Implementation of a Modular Magnetic Levitation Planar Motor

by

Curtis Stewart

A thesis
presented to the University of Waterloo
in fulfillment of the
thesis requirement for the degree of
Master of Applied Science
in
Mechanical and Mechatronics Engineering

Waterloo, Ontario, Canada, 2023

Author's Declaration

I hereby declare that I am the sole author of this thesis. This is a true copy of the thesis, including any required final revisions, as accepted by my examiners.

I understand that my thesis may be made electronically available to the public.

Abstract

A large-scale magnetically-levitated planar motor has the potential to revolutionize conveying and flexible manufacturing applications. The contactless nature nearly eliminates friction to produce less noise, vibration, and dust, which enables high-precision and energy-efficient operation. In this research, a maglev system is used which is newly designed and assembled by a team of graduate students at the Maglev Microrobotics Laboratory. The stator consists of square hollow-core coils and manipulates a levitated 2-D Halbach array mover. Three equipment setups are tested in this thesis: the 64-coil prototype with camera feedback, the 64-coil prototype with laser sensor feedback, and the MagFloor with camera feedback. The contributions of this thesis include the implementation of levitation through controller design and system integration, comparison of levitation precision, step responses, and trajectory tracking between the three setups, and improving the system performance through more advanced methods.

A PID control loop is designed in MATLAB/Simulink, with a PID for each of the six degrees of freedom of the mover and with a custom derivative calculation to overcome spikes from sensor sync issues, derivative kick, and measurement noise. The overall system integration is completed in TwinCAT and includes a visualization interface for user input and control of the system. The PIDs are first tuned by levitating the mover on a 64-coil prototype stator using a camera-based motion tracker for position feedback.

As expected, levitation precision is most precise with the eight laser sensors, with a precision of 0.005 mm in the xyz translation directions and 0.002° in the $\alpha\beta\gamma$ rotations. Conversely, the precision with the cameras is 0.008 mm in xy, 0.011 mm in z, 0.003° in $\alpha\beta$, and 0.002° in γ. Using the cameras further away on the MagFloor, the precision is reduced to 0.03 mm in xyz, 0.015° in $\alpha\beta$, and 0.01° in γ. The best step performance is found with the camera system on the 64 coils. For an 8 mm step in the x-axis with this setup, the rise time is as little as 0.045 s, the 2 % settling time is 0.088 s, and the overshoot is 0.275 %. Using ramp trajectories on the MagFloor, the maximum speed is found to be 500 mm/s in the xy plane and 75 °/s about the yaw rotation, which can achieve the full 360° range.

The levitation performance is further improved through the addition of a state estimator and an iterative learning controller (ILC). The state estimator compensates for the 7 ms system latency when using the camera feedback. This reduces the force and torque error, resulting in smaller fluctuations and raising the maximum speed. With this strategy, the maximum speed on the MagFloor is increased to 1000 mm/s in xy and 360 °/s in yaw. The

tracking error is reduced through the addition of ILC on top of the state estimator. On the 64 coils, the mean absolute error in x during the 500 mm/s region of an x-ramp decreased from 4.862 mm to 0.397 mm from the first to tenth iteration. The fluctuations in the levitation gap and the rotation axes are also reduced. The most significant improvement is seen in the 64-coil prototype, which has smaller measurement noise than the MagFloor.

Lastly, further improvements to the system are discussed as potential future work. These include improvements to methods discussed in this research as well as the next steps towards realizing a planar motor for conveying or flexible manufacturing applications.

Acknowledgements

I would like to take this opportunity to thank everyone who made this research possible. In particular, my deepest gratitude goes to my supervisor, Prof. Behrad Khamesee, whose constant support, invaluable guidance when reviewing my progress, and patience during my MASc program were instrumental in completing this work. I would also like to thank him for the opportunity to be a part of this project as it was amazing to work with such a one-of-a-kind large-scale magnetic levitation platform and the incredible team which designed and constructed it.

A special thanks goes to the team on the planar maglev project, which included Zhenchuan (Daniel) Xu, Chanuphon (Cha) Trakarnchaiyo, Dr. Moslem Goughari, Yang (Bob) Wang, and Dr. Xiaodong Zhang. It was also a pleasure working with the remaining lab members at the Maglev Microrobotics Laboratory: Pooriya Heris, Parichit Kumar, Saksham Malik, Dr. Heba Farag, Azeem Kahlon, Yashesh Dasari, Joseph Nofech, and Ridwan Bari.

Constructing and fabricating the Magnetic Levitation Floor would not have been possible without the tremendous support from the machining technicians: Mark Kuntz, Andrew Urschel, Brian Shuh, Jeff McCormick, and a special thanks to Jason Benninger for machining the frame of the mover and more. In addition, my gratitude goes to the RoboHub staff, Robert Wagner, Prof. Brandon DeHart, and Alexander Werner, and the RoboHub director, Prof. William Melek. The electronics technician Neil Griffett was also a huge help in bridging our knowledge gap.

Lastly, I would also like to thank Rui Zhang from Beckhoff Automation Canada and Eduard Prelipcean from Technosoft who were a great support in working with TwinCAT and the current amplifiers.

This project would not have been possible without the financial support from the Engineering Excellence MASc Fellowship and the Ontario Graduate Scholarship (OGS). Through the lab, this work was also supported by the Canada Foundation for Innovation (CFI) and the Natural Sciences and Engineering Research Council of Canada (NSERC).

Dedication

This thesis is dedicated to my family and, in particular, my parents, whose love, continual support, and patience helped me through this journey.

Table of Contents

List of Figures

List of Tables

List of Abbreviations

AMR autonomous mobile robot 5

DLPM double-layer planar motor 14

DOF degrees of freedom 1, 13, 15, 17, 46, 107, 108

FFT fast Fourier transform 102, 111

FMS flexible manufacturing system 4, 5

ILC iterative learning controller 3, 11, 28, 39, 109, 111

MLPM magnetically-levitated planar motor 1, 6, 7

MMLM moving magnet linear motor 13, 14

PID proportional-integral-derivative 11, 18, 28, 39, 46, 79, 93, 99, 107, 117

PLC programmable logic controller 27, 28, 30, 31, 41, 44, 54, 59, 76, 79, 115

SVD singular value decomposition 63, 64

UDP User Datagram Protocol 28, 54

Symbol Convention

To make the notation as clear as possible, letters with an arrow above ($\vec{F}$) refer to vectors, letters with a hat above ($\hat{n}$) refer to unit-length vectors, bold-face capital letters ($\mathbf{R}$) refer to matrices, and italic letters (x) refer to scalars.

There are multiple coordinate systems used throughout this document, and these may be denoted with subscripts or superscripts. For instance, the rotation matrix $\mathbf{R}_g^m$ denotes a matrix that can convert a vector in the **global** coordinate system, $\vec{F}^g$, to the **mover** coordinate system through the equation: $\vec{F}^m = \mathbf{R}_g^m \vec{F}^g$.

The coordinate systems will be denoted with

- m for the **mover** coordinate system at the bottom-center of the magnet array,
- c for the **coil** coordinate system at the top-center of the winding,
- f for the laser sensor **frame** coordinate system,
- and g for the **global** coordinate system at the center of the coil array.

Note that these letters may also be used to denote the location of one coordinate system within another. For instance, $\vec{m}^g = (m_x^g, m_y^g, m_z^g)$ is the position of the mover in **global** coordinates and $\vec{c}^m = (c_x^m, c_y^m, c_z^m)$ is the location of a coil in **mover** coordinates. For the sake of convenience, the position of the mover is often simply referred as an (x, y, z) location, rather than the full (m_x^g, m_y^g, m_z^g). When a coordinate system is not given, it is usually in the global coordinates. Similarly, the angles (α, β, γ) refer to the angles between the global coordinates to the mover coordinates, unless otherwise specified.

Chapter 1

Introduction

1.1 Introduction to Magnetic Levitation

Magnetic levitation (Maglev) systems are of increasing interest in many industries and have been a popular research topic in recent decades. Maglev systems aim to suspend an object without any mechanical connection through the use of magnetic fields. Typically, this involves utilizing electromagnetic coils to levitate a magnetized object, or conversely, suspending electromagnetic coils above permanent magnets. While maglev often utilizes permanent magnets, levitation can also be achieved using paramagnetic materials such as aluminum, when subjecting them to a time-varying magnetic field to produce eddy currents and a magnetic field in the opposing direction.

The primary advantage of maglev technology is that it eliminates contact between two surfaces. This means friction between the surfaces can be eliminated, resulting in more energy-efficient operation while producing less noise, vibration, and dust. The reduced friction enables high-speed processes, such as Maglev trains [1] and high-speed electrical machines using active magnetic bearings (AMBs) [2]. The dustless aspect of maglev transportation makes them particularly suitable for applications sensitive to contamination and requiring a clean environment, such as OLED display transportation [3, 4] and wafer transportation [5, 6]. The reduced vibrations of Maglev are of significant importance to high-precision applications like photolithography [7]. With the ability to provide force-at-a-distance, maglev is being investigated for remote-manipulation and wireless-actuation tasks in robotics [8]. For instance, magnetic micromanipulation could be used in the medical field to provide control over surgical devices and drug containers inside a human body [9, 10]. Other applications of maglev include levitated rotary tables [11, 12] and levitating a workpiece during metal additive manufacturing [13].

The focus of this thesis is on a magnetically-levitated planar motor (MLPM). This type of system consists of a flat stator capable of manipulating a levitated mover within a planar area. Since the mover is levitated, it must be controlled in six degrees of freedom (DOF), which includes three translational axes (x, y, z) and three rotational axes (roll, pitch, and yaw given by α, β, and γ). These systems typically support longer ranges in the horizontal

axes and some designs can even achieve unlimited yaw rotation, but the vertical axis and roll and pitch are limited. With smart design, stators can be made into modules which can be joined together to achieve any desired range or route of transportation of levitated objects, thus establishing a planar electromagnetic conveyor [14]. This has the potential to revolutionize manufacturing and conveying applications.

Figure 1.1 shows the large maglev planar motor constructed in the RoboHub at the University of Waterloo by the maglev team from the Maglev Microrobotics Laboratory. The 6×8 ft. platform consists of eight stator modules of square coils mounted on a lift, which is stored in a pit. The system can be lowered and covered to open the space for other purposes. When in use, it is raised so its surface is approximately floor level. As such, it is named the Maglev Floor, or "MagFloor" for short. The MagFloor can levitate a moving 2-D Halbach array of permanent magnets anywhere on its surface and utilizes a set of four motion-tracking cameras to provide the position feedback for the control loop.

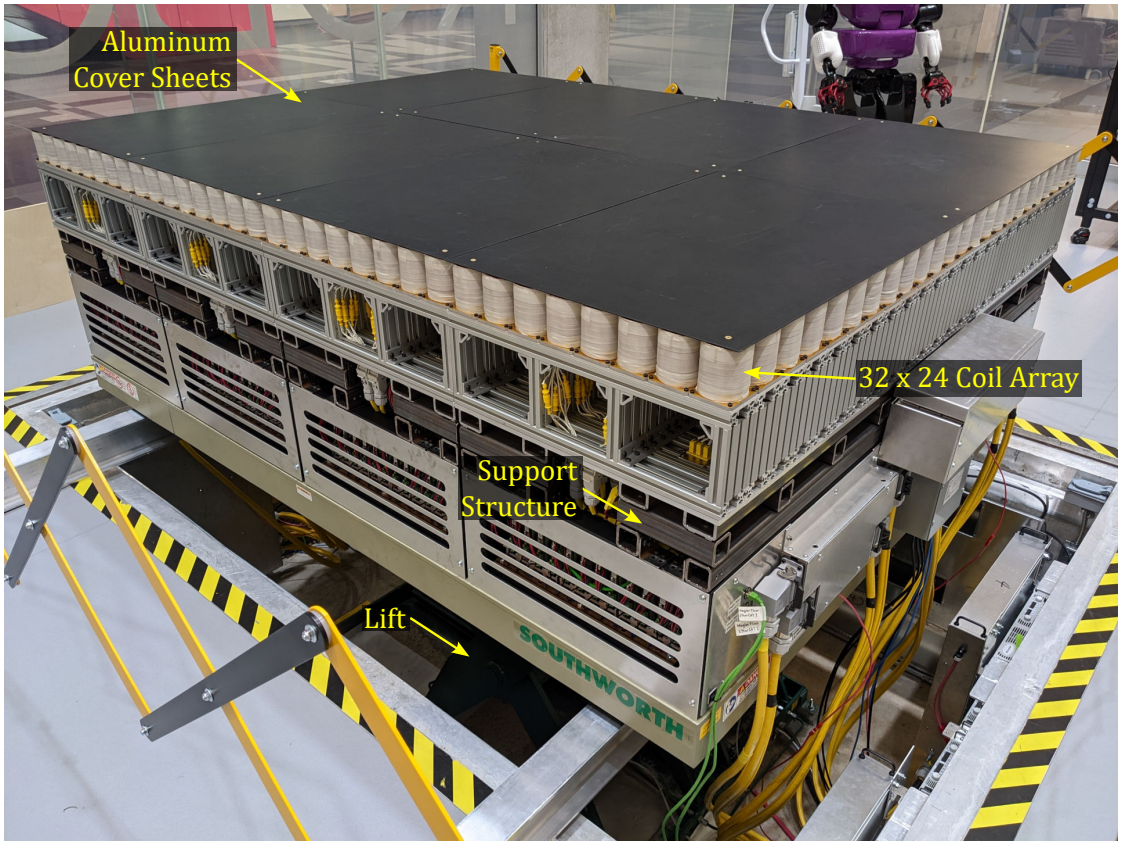

Figure 1.1: MagFloor raised to highest position.

Much of the research was completed on a smaller prototype of the MagFloor consisting of 64 coils for a 2×2 ft. area, as shown in figure 1.2. This prototype consists of the same design as the MagFloor with the same coils, frame structure, current amplifiers, and control unit, and is simply a smaller version of the MagFloor, except the cameras can be placed closer. In this research, successful levitation of a 2-D Halbach array of permanent magnets is achieved on both the 64-coil prototype and the MagFloor. Performance is compared between the two systems and between using laser sensors versus cameras on the 64-coil prototype. Improvements are also tested to the basic control strategy, such as adding a state estimator to compensate for the measurement delay and using an iterative learning controller (ILC), which are shown to improve performance. The objectives and contribution of the research are further discussed in section 1.3.

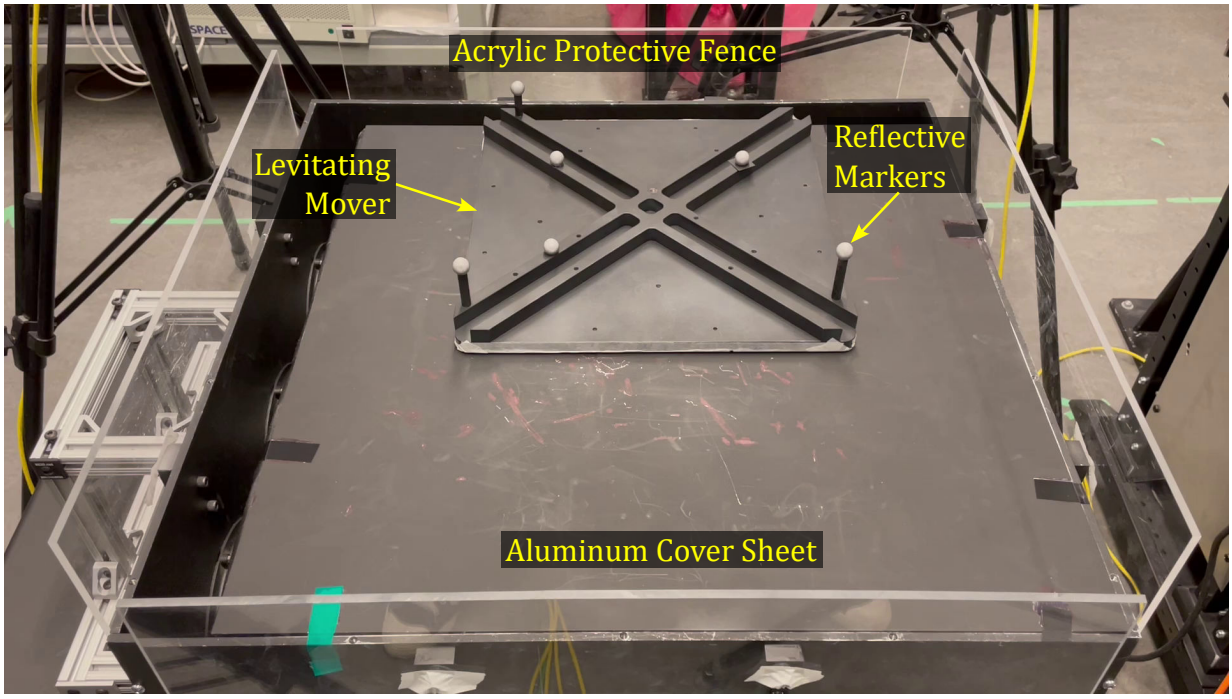

Figure 1.2: 64-coil prototype with mover levitating using camera feedback.

1.2 Application to Flexible Manufacturing

Modern manufacturing is continuously changing due to ever-evolving products, increased levels of customization, increased product variety, shorter product life cycles, variability in demand, and global competition. Because of these trends, manufacturing facilities need to be highly flexible and capable of producing multiple products with varying volumes to meet current demand. Traditional manufacturing approaches aimed toward high-volume production take significant time to modify layouts and routing for different products. As such, a flexible manufacturing system (FMS) seeks to solve these issues by becoming more adaptable to changing product needs and requirements. Manufacturing flexibility can be split into several dimensions as shown in table 1.1 [15, 16]. Note that other sources include other dimensions such as material handling flexibility, program flexibility, market flexibility, and labour flexibility [16, 17].

Table 1.1: Flexibility dimensions and their definitions. [15, 16]

Flexibility dimension	Definition
Machine flexibility	Various types of operations that the machine can perform without requiring prohibitive effort in switching from one operation to another
Operation flexibility	Ability of a part to be produced in different ways
Routing flexibility	Ability to produce a part by alternative routes through the system
Volume flexibility	Ability of the manufacturing system to be operated profitably at different levels of overall output
Expansion flexibility	Ease with which manufacturing system capacity and capability can be increased when needed
Process flexibility	Set of part types that the system can produce without major set-ups
Product flexibility	Ease with which new parts can be added or substituted for existing parts
Production flexibility	Universe of part types that the manufacturing system can produce without adding major capital equipment

Manufacturing flexibility is required to respond to both internal changes and external forces. Internal changes can include equipment breakdowns, variable task times, delays, rejects, and rework [16]. External forces can include a changing level of demand,

product prices, product mix, availability of resources, consumer preferences, technological innovations, regulations, and more [16]. To enable flexibility to these changing requirements, many components are involved in the FMS. These components can be classified into machine tools, materials handling systems, storage areas for in-process inventory, and computer control [18].

In the context of materials handling, some older solutions to sorting and distributing products to various production pathways include powered sweeps, pop-up rollers, pneumatic pushers and swivelling wheels. These must be installed at each pathway junction, and it is not possible to add, for instance, pop-up rollers into the middle of a conveyor belt track without significant redesign. To increase versatility, omnidirectional conveyors have been developed as shown in figure 1.3. These conveyors utilize omni-wheels to independently move objects in any planar direction and can also rotate objects about the yaw axis for proper alignment. These omnidirectional platforms enable highly flexible material flow and can easily be extended by adding more modules [19, 20]. They can also increase efficiency as only the wheels below products need to be powered on, and the wheels themselves are lightweight, so energy is predominantly spent moving the payload and not the components of the system.

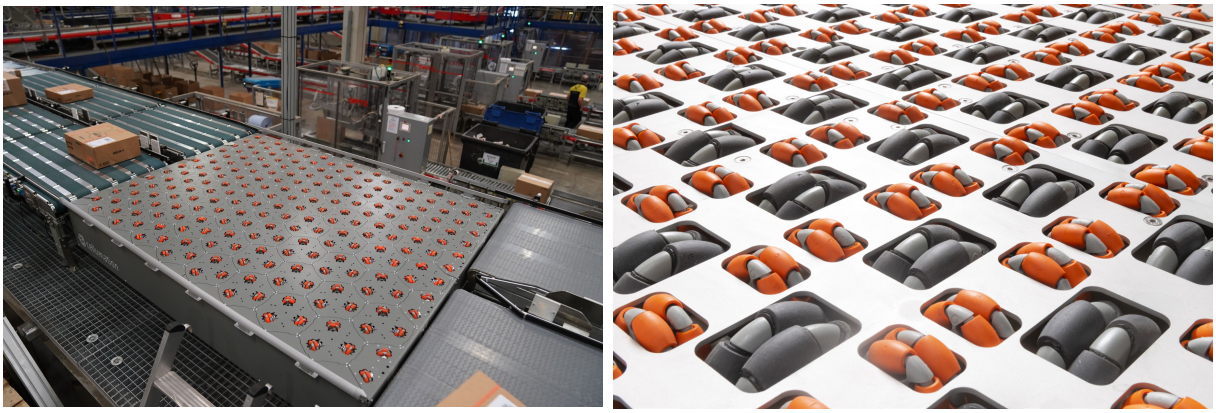

(a) Celluveyor by Cellumation [21] **(b)** Omnia Wheel Conveyor [22]

Figure 1.3: Omnidirectional conveyor systems.

Another approach to increase flexibility in manufacturing, warehouse, and distribution environments is to utilize autonomous mobile robots (AMRs), such as those offered by Fetch Robotics Inc. shown in figure 1.4. The Fetch robots consist of several standard bases capable of supporting payloads from 100 to 1500 kg, with a variety of products mounted on top, such as connections to move pallets, carts or shelves, or powered top

rollers to integrate with conveyor systems. The Freight100 base product can move at 1.5 m/s, turn in place, run for 9 hrs, and has a variety of sensors and software built-in. [23]

Figure 1.4: Autonomous Mobile Robots by Fetch Robotics Inc. [23]

Similar to the omnidirectional conveyors using omni-wheels, maglev planar motors enable flexible and independent trajectories of levitated objects. However, MLPMs have all the advantages of maglev technology, including the contactless operation eliminating friction and reducing noise, vibration, and dust. Due to the lack of moving parts, they require less maintenance and the stators can even be encased to become waterproof if required for the manufacturing process. Maglev planar motors can drive anywhere on the stator on any path, offer nearly instant directional change, and provide very high-precision control. Because of the high-precision control, maglev planar motors can be more than conveying mechanisms and can integrate directly into machining processes, reducing the complexity of other machining tools. To aid in manufacturing tasks, the movers could also be attracted to the stator, instead of repelled, to magnetically lock them at a workstation.

A few commercial MLPMs have become available in the recent few years. One example is the XBot by Planar Motor Inc. as shown in figure 1.5. The XBot specifies a repeatability less than 5 µm in all axes and supports full 360° rotation about the z-axis. The movers range from a size of $120 \times 120 \times 10$ mm^3 with a payload of 0.6 kg to the largest size of $450 \times 450 \times 16$ mm^3 with a payload of 14.4 kg. It can levitate with a gap between 0.5 to 4 mm, move up to a maximum speed of 2 m/s, and accelerate at 20 m/s^2. Each stator module has dimensions of $240 \times 240 \times 70$ mm^3, requires a supply voltage of 48 VDC, and can be arranged in any layout. [24]

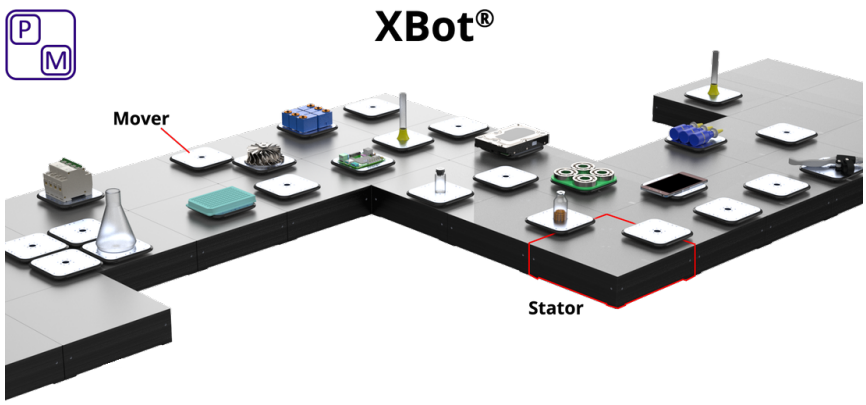

Figure 1.5: XBot by Planar Motor Inc. [24]

Another commercially available MLPM is the XPlanar by Beckhoff Automation Ltd. as shown in figure 1.6. The XPlanar has similar specifications to the XBot and can rotate a full 360° about the z-axis, tilt in other axes up to 5°, levitate up to 5 mm, and move up to a maximum speed of 2 m/s. The position resolution is 1 µm in (x, y, z) and 0.001° in the rotation axes, and the repeatability is 50 µm in (x, y), 60 µm in (z), and 0.1° in the rotation axes. The movers range from a size of $113 \times 113 \times 12$ mm^3 with a payload of 0.4 kg to the largest size of $235 \times 235 \times 12$ mm^3 with a payload of 4.2 kg. For larger payloads, the movers can be mechanically coupled or operated as a group. The stator modules have dimensions of $240 \times 240 \times 67$ mm^3 and can be arranged in any layout. [25]

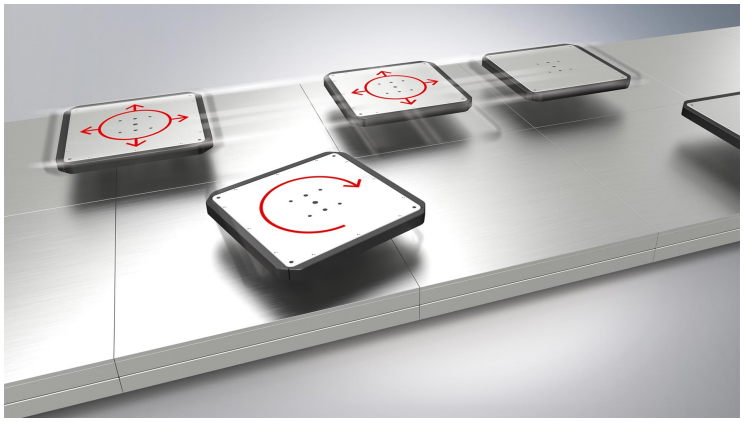

Figure 1.6: XPlanar by Beckhoff Automation Ltd. [25]

1.3 Objectives and Contributions

This research demonstrates the successful implementation of a modular maglev planar motor which was newly designed by a team of graduate students at the Maglev Microrobotics Laboratory. This planar motor operates without contact between the mover and the stator, removing friction to reduce noise, vibration, and dust, and reduce the need for maintenance. The system can achieve high-precision motion on any desired trajectory on the platform, and the stator modules could be arranged in any desired layout per the facilities' requirements. Overall, maglev planar motors have the potential to revolutionize the manufacturing industry and substantially increase system flexibility.

The design of the electromagnets and stator structure used in this research was completed as prior work by Dr. Xiaodong Zhang and Chanuphon Trakarnchaiyo, and the design of the 2-D Halbach array mover was completed in parallel by Zhenchuan Xu.

1.3.1 Main Objectives

To achieve the implementation of the maglev planar motor, the following main objectives were set:

1. Achieve levitation with the maglev system through completion of system integration, controller design, and controller tuning.
    - Tune the internal PI controllers in the current amplifiers.
    - Complete system integration in TwinCAT with a visualization interface for user control of the system.
    - Design and tune a controller for the maglev system.
2. Compare levitation performance for each of the three setups: the 64 coils with laser sensors, the 64 coils with cameras, and the MagFloor with cameras.
    - Determine the levitation precision from small step responses and the system latency, rise time, settling time, and overshoot from larger steps.
    - Determine the trajectory tracking performance, including maximum speed and cross-axis fluctuations.
3. Improve the levitation performance through more advanced techniques such as a state estimator and an iterative learning controller.

1.3.2 Contributions

The following contributions were achieved as a result of this research:

C1: Aided the maglev team in constructing, fabricating, and commissioning of the 64-coil prototype, the MagFloor, and the 2-D Halbach mover.

This involved assembling each stator module, installing the electromagnetic coils, power supplies, and power distribution boxes, completing all the wiring, installing the cover sheets to provide eddy-current damping, testing each component, and other tasks. The MagFloor construction was started in 2020 and completed in the first half of 2022. The major work for assembling the mover involved epoxying the 2-D Halbach array of 120 permanent magnets into the machined aluminum frame. It also included designing and fabricating flat plates against which the laser sensors can measure.

C2: Completed system integration in TwinCAT, developed a PID control loop to avoid derivative spikes, and tuned the controller.

As a first step to the system integration, the internal PI controllers in the current amplifiers were tuned and tested to determine response time and bandwidth. Next, a basic PID control loop was designed in MATLAB/Simulink and within the control loop, the force and torque model developed by Xu et al. [26] was integrated for use in the wrench method to determine coil current targets. Due to instability caused by derivative spikes during initial testing, a custom method was developed for calculating the derivative to improve stability. The overall system integration was completed in TwinCAT for running on the Beckhoff server PLC. A visualization interface was designed in TwinCAT for control and user input to the maglev system, with methods for generating and logging trajectories in real-time. The PIDs were first tuned on the 64-coil prototype using camera-based position feedback and successful levitation was achieved.

C3: Implemented levitation using the laser displacement sensors for position feedback.

This first involved designing and constructing a frame to hold the eight laser displacement sensors in position above the 64-coil prototype. The frame was designed such that the eight sensor heads can move together and the apparatus can be easily re-positioned above the 64 coils for testing in various locations. An algorithm was also developed to convert the eight linear displacement readings into the 6-D position and orientation of the mover, with a method for calibration.

C4: Compared levitation performance between each of the three setups: the 64 coils with laser sensors, the 64 coils with cameras, and the MagFloor with cameras.

First, the measurement noise of each system was found before the levitation. Then, the levitation precision with each setup was determined by taking very small steps. Using larger steps below saturation, the step responses were found to determine the rise time, settling time, overshoot, and latency. Using smooth ramp targets, the maximum speed and fluctuations in the levitation gap and rotations were found. The tracking performance to other trajectories such as a circle and figure-eight was also found.

C5: Improved the levitation performance through the implementation of a state estimator and an iterative learning controller (ILC).

A state estimator was implemented to compensate for the delay between the sensor measurements and the coil actuation by using the velocity of the mover and the control effort to update the delayed measurement to the current position. This increased the maximum speed and reduced the fluctuations in the levitation gap during movement. An iterative learning controller was then tested, which improves the performance on repeated iterations of a given trajectory by learning modifications to the control effort from the position error. Using ILC, both the xy tracking performance was improved and the fluctuations in other axes were reduced.

1.4 Thesis Outline

The remaining chapters in this thesis are organized as follows:

Chapter 2 starts with a literature review on planar maglev systems and then discusses relevant theory pertaining to the implementation of the planar maglev system in this thesis. For better context, the four coordinate systems and the transformations between them are introduced. Some background on the Lorentz force and magnetic nodes method is discussed. Finally, a summary is provided of the real-time approach used in this thesis to estimate the forces and torques by using a harmonic model and Fourier series.

Chapter 3 presents the system setup, starting with the design of the stationary electromagnetic coil array and the permanent magnet mover. An overview of the experimental setup is provided, showing the flow of data between devices. Preliminary testing of the current amplifiers is shown, with plots of responses to step and sinusoidal current targets. Lastly, some safety precautions are discussed.

Chapter 4 shows the design of the proportional-integral-derivative (PID) control loop and wrench method for determining current targets. Other features are also discussed, such as methods for dealing with derivative kick, rotating the yaw past the discontinuity of 180°, dealing with slight variations in the surface level of the MagFloor, and improving the performance when one or two coils are saturated.

Chapter 5 discusses the two measurement systems of the Vicon cameras and laser displacement sensors. The algorithm to convert from the linear displacement readings of the laser sensors to the 6-D position and orientation of the mover is described. Finally, the measurement noise during a static placement of the mover resting on the stator is shown for each system.

Chapter 6 presents the results of sets of tests performed while levitating on each system, such as small stepping near the measurement precision, larger step responses to determine system latency, rise time, settling time, and overshoot, and trajectory tracking of motions such as ramps and a circle.

Chapter 7 is a preliminary investigation into improvements to the control design, such as adding a state estimator to compensate for the system delay and implementing an ILC. The results of testing these improvements are shown.

Chapter 8 concludes the research and suggests future work to improve the system.

Chapter 2

Literature Review and Related Theory

2.1 Planar Maglev in Literature

Planar motors commonly utilize repulsive levitation above the stationary stage, since this makes it easier to handle large weights, which can start resting on the stationary stage. An early exception did not levitate and instead utilized a permanent magnet mover resting on ball bearings, with a stator above [27]. It is also common for the electromagnetic coils to be stationary and support a permanent magnet mover. However, some systems utilize moving coils above an array of permanent magnets instead [28, 29]. In this case, there are fewer coils and the electrical complexity is simpler. However, moving coils have increased weight and the added challenges of cooling the coils and routing the electrical wires to energize them. These challenges make moving coil systems not viable for a flexible maglev conveying system. Among planar levitation systems, there are a variety of stator and mover designs, modelling approaches, and control schemes.

2.1.1 Stator Designs

Planar magnetic levitation has been reported as early as 1993, where a small cylindrical permanent magnet was levitated above five iron-core electromagnets [30]. In 1998, a high-precision magnetic levitation stage for photolithography was achieved through the levitation of a mover consisting of four 1-D Halbach arrays [7]. In this system, the levitated mover operated within a motion range of 50 mm by 50 mm, and with as low as 5 nm RMS positioning noise in x and y. This type of system is composed of sets of moving magnet linear motors (MMLMs), where each 1-D Halbach array is above a coil that can provide 2-DOF forces. The combination of four sets of MMLMs allows for complete 6-DOF control of the mover. In 2017, a model of the eddy current damping and end-effects of the 1-D Halbach array was developed [31], and in 2019, a dual-stage maglev system was added to further improve the positioning precision [32]. While planar maglev systems composed of sets of MMLMs can achieve very high precision, they have a limited range of motion as the magnets cannot move off of their paired coil.

Several coil topologies, magnet arrangements, and electromechanical models were studied in Jansen's 2007 PhD thesis [33]. Within this study, a herringbone pattern of rectangular coils in the stator paired with a moving 2-D Halbach array was particularly effective as this aided in decoupling forces for easier computation and control [34]. In this setup, the mover can move between coil sets to achieve a much larger motion range than those composed of sets of MMLMs. However, the herringbone pattern cannot be easily split into modular sections for a customizable conveyor system and also has the disadvantage of directional inconsistency in performance since it is not symmetrical.

Other designs solve the directional inconsistency of the herringbone pattern, such as the double-layer planar motor (DLPM) presented by Rovers et al. [35, 36], and recently continued in a method for active deformation control of the mover [37]. The DLPM consists of two layers of rectangular coils where the top layer is oriented perpendicular to the bottom, and can remove the directional inconsistency. As an added difficulty, the thickness of each layer must be carefully designed in order for the layers to have similar contributions.

Another design utilizing multiple layers is a printed circuit board (PCB) approach [14, 38, 39]. In these systems, the PCB has layers of approximately straight conductors oriented perpendicularly to simplify electromechanical modelling. These systems also have the advantage of tighter manufacturing tolerances. However, due to PCB limitations, the number of layers and the thickness of the conductors is limited, thus limiting the electromechanical strength of the stator. The PCB approach is utilized in both the commercial products of XBot and XPlanar, discussed in section 1.2.

For a strong and symmetric design, an array of circular or square coils can be used [40, 41]. Between these choices, circular coils are easier to model electromechanically due to their axisymmetric nature, while square coils have a greater packing density of the magnetic field for the same spacing [42]. Both square and circular coils have x, y directional consistency due to their symmetry, and they are easy to divide into modular sections for a customizable layout. An array of square coils is used in the stator in this research.

2.1.2 Mover Designs

Three main permanent magnet mover designs are four 1-D Halbach arrays [39], a 2-D Halbach array [34], and disk magnets [43]. Halbach arrays utilize a specific arrangement of magnets oriented in horizontal and vertical directions, which concentrate the magnetic flux towards the bottom, with the added benefit of a less significant field above the mover towards any payload [44]. Halbach arrays have a greater magnetic field strength compared to NS arrays composed of only vertically magnetized segments of the same pole pitch [39].

See figure 2.1 for an illustration of a 1-D Halbach array. In mover designs, it is common to utilize four 1-D Halbach arrays along the four sides of the mover to achieve the 6-DOF.

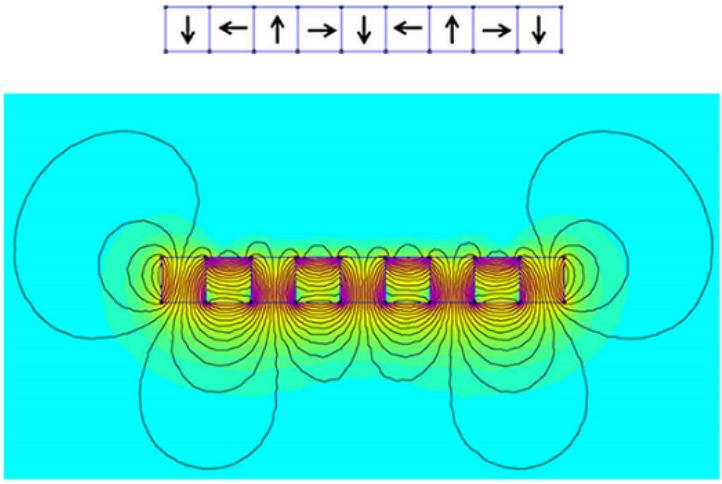

Figure 2.1: Example magnetic field of a 1-D Halbach array [45].

Another approach utilizes permanent disk magnets in the mover. Due to the axis of symmetry, using only one disk magnet allows 5-DOF motion control, but using two or more disk magnets can achieve full 6-DOF control [42]. In 2013, by utilizing two permanent disk magnets above a set of circular coils, large rotation ranges of $\pm 40^\circ$ in roll, $\pm 15^\circ$ in pitch, and unlimited yaw were achieved [43]. In addition, Miyasaka and Berkelman proposed a novel cube configuration of disk magnets to achieve an unlimited omnidirectional rotation range [46].

A 2-D Halbach array extends the same Halbach pattern of orienting the magnets to both horizontal directions to create a two-dimensional array. While 1-D Halbach arrays create 2-D magnetic sinusoidal magnetic fields, 2-D Halbach arrays create 3-D magnetic fields, which improves the power efficiency for large displacements [47]. However, since 2-D Halbach arrays increase the modelling complexity and have more significant force ripples, multiple 1-D Halbach arrays are simpler to implement [44]. Modifications to the traditional 2-D Halbach array have also been proposed to reduce the error of the harmonic model, such as adding 45° magnetized magnets [48] or using magnets of different heights and intensity [49]. In this research, a standard 2-D Halbach array was chosen for the mover due to its strong magnetic field on the bottom, sinusoidal nature of the magnetic fields to simplify modelling, and greater power efficiency compared to 1-D Halbach arrays.

2.1.3 Modelling Methods

Maglev planar motors must model the forces and torques on the mover provided by the electromagnetic coils to determine the current targets to send at each sampling interval. Three common methods for calculating forces in electromechanical systems include Maxwell stress, virtual work, and Lorentz force [50]. Finite-element packages often use the Maxwell stress or the virtual work method since this works between both current-carrying objects and non-current-carrying objects. However, the Lorentz force method is computationally much faster and is suitable for planar motors since the coils are current-carrying. To calculate the Lorentz force, a model of the magnetic flux density of the permanent magnets is required, which can be found using the magnetic surface charge model [50], the magnetic node model [51], and finite element methods [43]. Then, to find the Lorentz force, the integral must be solved over the current-carrying conductor.

Especially in the case of finite element methods, the computation is much too slow to perform in real-time for control of the system. One method to mitigate this issue is to utilize a lookup table to store how much force and torque per unit current can be generated for each coil at each location respective to the mover [40, 43, 52]. This means pre-calculating the force and torque values for a range and resolution of discrete positions. To achieve good accuracy, a fine resolution is needed, which causes the table to grow very large for the six degrees of freedom of the mover, resulting in significant offline computation and online memory usage. As such, methods have been proposed for analytical or real-time methods for various mover and coil shapes.

In the case of rectangular coils under a 2-D Halbach array, early work developed three approaches: the magnetic surface charge approach which treats each magnet separately; a harmonic model to solve the volume integral for the long straight segments of the coil analytically and reduce the corner segments to a numerical surface integral; and a fully analytical model using only the first harmonic and neglecting the corners [34, 53]. In subsequent research, it is common to simply use the real-time analytical model which treats the coil as four straight segments and neglects the corners [29, 54, 55]. In 2013, a real-time method considering the corners of a rectangular coil was developed using composite numerical integration and the Newton-Leibniz formula [56]. In addition, real-time numerical solutions using the magnetic nodes and Gaussian quadrature were successfully implemented on a field-programmable gate array (FPGA) [57]. As another approach, an offline method to optimize the design parameters of a 2-D Halbach array above a rectangular or square coil was developed using the magnetic charge method and Gaussian quadrature [58].

Real-time models have been proposed for analytically solving the volume integral for a 2-D Halbach array above circular coils [41] and square coils [59]. To enable these real-time

methods, the magnetic flux density under the center of a 2-D Halbach array is approximated using a harmonic expression of sinusoidal waves [49]. To estimate the magnetic flux density in the end effect of a 2-D Halbach array over an arbitrary coil shape, it has been proposed to utilize Fourier series [60]. A real-time method was recently developed by Xu et al. [26] which estimates the forces and torques using the first harmonic in the center of the 2-D Halbach, a third-order Fourier series in the edge regions, and uses superposition for the corners. This method is used in this research and is discussed further in section 2.4.

2.1.4 Sensor Systems

There are several main types of sensor systems used to provide position feedback in planar maglev systems: laser interferometers [7], laser triangulators [40], Hall effect sensors [61], capacitive sensors [31], eddy-current sensors [29], and camera-based motion trackers [42]. Capacitive sensors and eddy-current sensors are both short-range proximity sensors that can be used below the mover to accurately measure the levitation gap and the pitch and roll rotations. Laser displacement sensors are often utilized to measure against the sides of the mover to determine the x, y translations and yaw rotation. Of the laser displacement sensors, laser interferometers have much finer measurement precision than laser triangulators, but are more complex to set up. However, a configuration with laser sensors on the side and proximity sensors below the mover is not suitable for unlimited planar range since the mover can easily move out of range of the laser sensors.

To achieve an unlimited planar motor, two common approaches are to utilize Hall sensors in the stator or to use camera-based motion trackers. Hall sensors can detect the magnetic field of the mover, so many Hall sensors spread throughout the stator can be used to determine the 6-DOF position and orientation. However, maintaining accuracy with Hall sensors is difficult due to errors caused by higher harmonic components of the magnet array and manufacturing tolerances, so model parameters may vary with position and between magnet arrays [61, 62].

In this research, a Vicon camera motion tracking system is utilized, similar to the work by Zhang et al. [42]. The camera-based system readily accommodates long-stroke applications and with just four cameras, the entire 6 x 8 ft. area of the MagFloor can be covered with sub-millimetre resolution. Since the cameras detect markers on the mover, it is easy to switch mover designs and no new sensing model is required as would be for Hall sensors. With automatic camera switching, individual cameras can be placed closer to see only part of the area, such that multiple sets of cameras can be utilized to achieve the full range. With this ability, a theoretically infinite motion range can be measured. In general,

adding more cameras would increase accuracy and reduce measurement noise. Additionally, a set of eight laser triangulators is also separately tested to provide measurement feedback to demonstrate higher precision control. In a more advanced setup, a large motion range could be accommodated by a camera-based tracker, while higher precision, shorter-range sensing could be installed in specific locations where needed.

2.1.5 Controller Designs

Most research in maglev planar motors utilizes classical controllers such as the PID or lead-lag controllers. Recently, interesting research has been conducted into iterative learning-based controllers. In 2016, Hu et al. [63] proposed learning adaptive robust control (LARC) which contains an adaptive robust control (ARC) term and an iterative learning control (ILC) term in series. The ARC term can provide parameter adaption and robustness to uncertain disturbances, while the ILC term is set to modify the reference under repetitive tasks to achieve excellent tracking performance. For some tasks, the overall contour error is more important than the time-based position error. For this, a Newton-ILC method has been proposed which estimates the contouring error and uses iterative learning to adjust the reference commands to improve accuracy [64]. Iterative learning has also been proposed to aid in the identification of the repeatable errors caused by the trajectory and force ripple and separate them from errors caused by mechanical vibration and measurement noise [65].

A disadvantage of ILC is that it requires repeated iterations of each trajectory and does not perform well with slight changes in the trajectory. In [66], feedforward control is switched between ILC and a data-based fixed-structure feedforward control depending on whether the references are repeated, so that performance is still improved on new trajectories. Alternatively, a projection-based ILC (P-ILC) was proposed which uses frequency-domain-based design and basis functions to fit the reference trajectory to be applicable to varying tasks [67]. In 2021, a feedforward reference modification prediction strategy using gated recurrent units (GRU) was proposed to improve tracking performance [68]. This strategy trains a GRU neural network to learn the relationship between trajectories and reference modification and can provide reasonable trajectory modification for new trajectories. In 2022, an online iterative learning compensation method was proposed which is based on model prediction [69].

The standard ILC is tested in this research as a preliminary step to improving the levitation performance as it is simple to implement and effective for repeating tasks. The ILC implementation in this research also takes into account the system latency to modify the feedforward control based on the delayed measurements.

2.2 Coordinate Systems

There are three main coordinate systems used to describe the setup, as shown in figure 2.2. The **global** coordinate system $[X_g, Y_g, Z_g]$ is located at the center of the coil array, at the top of the winding of the coils. Each **coil** has its own coordinate system $[X_c, Y_c, Z_c]$, and the location of a coil in the global coordinates is $\vec{c^g} = [c_x^g, c_y^g, c_z^g]$. The **mover** has a coordinate system $[X_m, Y_m, Z_m]$ located at the bottom center of the magnet array which translates and rotates with the mover. The position of the mover in the global coordinates is given by $\vec{m^g} = [m_x^g, m_y^g, m_z^g]$. To simplify the calculation, the forces and torques on the mover are first calculated in the mover coordinate system, and each coil is described in mover coordinates as $\vec{c^m} = [c_x^m, c_y^m, c_z^m]$. Figure 2.2 shows these coordinate systems for the 64-coil prototype and they are similarly set up for the MagFloor.

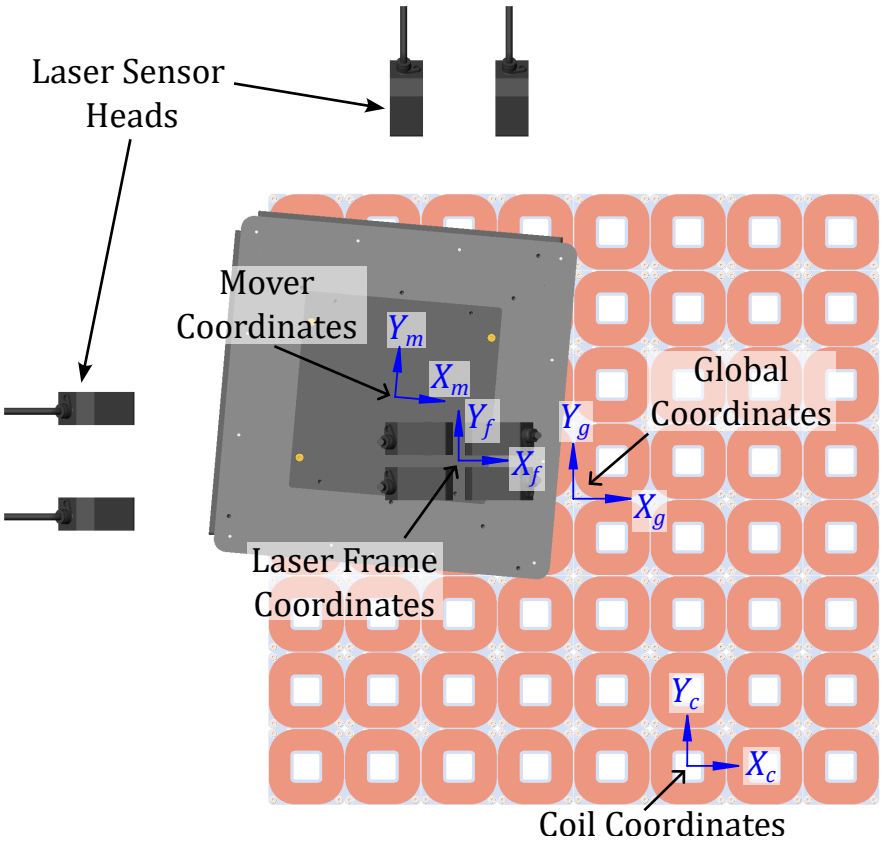

Figure 2.2: System coordinates, shown from the top.

The Vicon camera motion tracking system is set up such that its global coordinate system is aligned with the global coordinates at the center of the coil array, and as such, the measured 6-D position of the mover is given in the global coordinates. However, an extra coordinate system is needed for the laser displacement sensors. Since the laser sensors have a much shorter measurement range, the eight laser triangulators are mounted on a custom aluminum frame such that all eight sensor heads can move together and be positioned where desired above the 64 coils. The position of this sensor **frame** creates another coordinate system $[X_f, Y_f, Z_f]$, such that if the mover were aligned with it, all laser sensor heads would return approximately zero. Using the laser sensors, the mover's 6-D position is first measured in the **frame** coordinates and then transformed into the **global** coordinates to be used in the controller. This process is detailed in section 5.3.

Euler angles in the XYZ form are used to describe the roll (x-axis rotation), pitch (y-axis rotation), and yaw (z-axis rotation) of the mover with respect to the global coordinate system, denoted by α, β, and γ, respectively. Coordinates can be transformed from one coordinate system to another using a rotation matrix. For example, a coil location in mover coordinates can be found from

$$\vec{c^m} = \mathbf{R}_g^m(\vec{c^g} - \vec{m^g}), \tag{2.1}$$

where $\mathbf{R}_g^m$ describes a rotation from global to mover coordinates.

The rotation matrix in the XYZ form corresponds to three **intrinsic** rotations about the x, y, then, z axes, where each rotation is about the *new* coordinate axes from the previous rotation. This is equivalent to three **extrinsic** elementary rotations in the reverse order about the z, y, then x axes of the same angles, where the rotations are about fixed external axes. Note that rotation matrices left multiply the vector, so the matrices are applied right to left. Therefore, an XYZ rotation matrix is given by

$$\mathbf{R}_{xyz} = \mathbf{R}_x\mathbf{R}_y\mathbf{R}_z, \tag{2.2a}$$

$$\text{where} \quad \mathbf{R}_x = \begin{bmatrix} 1 & 0 & 0 \\ 0 & \cos(\alpha) & -\sin(\alpha) \\ 0 & \sin(\alpha) & \cos(\alpha) \end{bmatrix}, \tag{2.2b}$$

$$\mathbf{R}_y = \begin{bmatrix} \cos(\beta) & 0 & \sin(\beta) \\ 0 & 1 & 0 \\ -\sin(\beta) & 0 & \cos(\beta) \end{bmatrix}, \tag{2.2c}$$

$$\text{and} \quad \mathbf{R}_z = \begin{bmatrix} \cos(\gamma) & -\sin(\gamma) & 0 \\ \sin(\gamma) & \cos(\gamma) & 0 \\ 0 & 0 & 1 \end{bmatrix}. \tag{2.2d}$$

2.3 The Lorentz Force and Magnetic Nodes

In order to properly levitate and manipulate the mover with the electromagnetic coils, it is necessary to have a relationship between the current in each coil and the forces and torques applied to the mover. In this type of system, the mover levitates via Lorentz levitation, as the forces are generated in current-carrying conductors (the electromagnetic coils) immersed in external magnetic fields (from the permanent magnets of the mover) [70]. The Lorentz force $\vec{F}_L$ is the force experienced by a current-carrying conductor with current $\vec{i}$ in an external magnetic field with magnetic flux density $\vec{B}$. The Lorentz force per unit length of a conductor is given by

$$\vec{F}_L = \vec{i} \times \vec{B}. \tag{2.3}$$

To calculate the Lorentz force, it is necessary to estimate the magnetic flux density provided by the external magnet. One approach is to use the magnetic nodes method, proposed by F. Bancel in 1999 [51]. The magnetic nodes approach models a parallelepiped magnet with uniform magnetization, such as a cuboidal magnet, by setting nodes at its eight corners, as shown in figure 2.3. The approach comes from Maxwell's equations and models the magnets as a distribution of equivalent magnetic charges to compute the force. This assumes that the magnet is an ideal magnet with fixed and uniform magnetization. It also assumes that there are no other materials which disturb or contribute to the magnetic field, such as a ferrous core of a coil. Since the coils in the planar motor used in this research have cores of hollow aluminum square channels, this is a reasonable assumption.

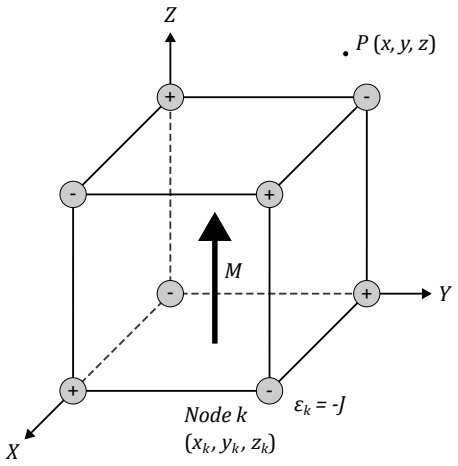

Figure 2.3: Representation of a cuboidal magnet using magnetic nodes [51].

Using the magnetic nodes method, the magnetic flux density at point P produced by the magnetic node k at each corner can be expressed by

$$B_{xk} = \frac{\epsilon_k}{4\pi} \ln\left(-y_r + \sqrt{x_r^2 + y_r^2 + z_r^2}\right), \tag{2.4a}$$

$$B_{yk} = \frac{\epsilon_k}{4\pi} \ln\left(-x_r + \sqrt{x_r^2 + y_r^2 + z_r^2}\right), \tag{2.4b}$$

$$B_{zk} = \frac{\epsilon_k}{4\pi} \arctan\left(\frac{x_r y_r}{z_r \sqrt{x_r^2 + y_r^2 + z_r^2}}\right), \tag{2.4c}$$

where $x_r = x - x_k$, $y_r = y - y_k$, $z_r = z - z_k$, and ϵ_k is the magnetic charge J, which is given by the remanence of the permanent magnet B_r, with sign as indicated in figure 2.3. Note that these flux densities are given in the coordinate system of the magnet, which is oriented the same as the **mover** coordinates $[X_m, Y_m, Z_m]$. The total magnetic flux density at point P is the summation of the flux density from each of the n nodes, from each of the h magnets

$$\vec{B}_P = \begin{bmatrix} B_x & B_y & B_z \end{bmatrix}^T = \sum_{l=1}^{h} \sum_{k=1}^{n} \vec{B}_{lk}. \tag{2.5}$$

The total force on an electromagnetic coil under the magnetic field of the mover can then be found by the volume integral of the Lorentz force in equation (2.3). The force on the mover produced by a coil will be equal and in the opposite direction and is given by

$$\vec{F} = -\iiint \vec{i} \times \vec{B}\, dV, \tag{2.6}$$

where $\vec{B}$ is the magnetic flux density at the center of each element of integration, found through equation (2.5). The torque $\vec{T}$ on the mover is then the integral of the cross product of the torque arm and the Lorentz force

$$\vec{T} = -\iiint \vec{r} \times (\vec{i} \times \vec{B})\, dV, \tag{2.7}$$

where $\vec{r}$ is the distance vector between the center of mass of the mover to the center of the current element.

The volume integral for the force and torque contribution of a coil can be computed using a numerical method which splits the coil into a mesh of many small elements. However, this method of integration to find the forces and torques is computationally expensive and not suitable for real-time control. As the controller runs at 1000 Hz in this system, the force and torque contributions for all coils must be estimated well within 1 ms for real-time control. To achieve this speed, a data-driven method is utilized to develop functions to quickly estimate the total forces and torques of each coil.

2.4 Force and Torque Modelling

A 3-D data-driven force and torque modelling method developed by Xu et al is utilized in this system for real-time force and torque estimation [26]. This method uses a set of sinusoidal functions and Fourier series to directly estimate the forces and torques based on the relative location of a coil under the mover. The functions result from curve fitting to data generated using the Lorentz force numerical integration technique with magnetic nodes described earlier.

The area under the Halbach array is divided into nine regions: a central region, four edge regions and four corner regions. By splitting the area into these separate regions, the edge effect of the 2-D Halbach array is considered, while maintaining good accuracy in the center. Under the central region of the Halbach array, the forces produced on the mover can be modelled with harmonic functions using

$$\vec{F}_{\text{center}}(c_x^m, c_y^m, c_z^m) = I \begin{bmatrix} K_x \cos(\eta_x)\sin(\eta_y) \\ K_y \sin(\eta_x)\cos(\eta_y) \\ K_z \sin(\eta_x)\sin(\eta_y) \end{bmatrix}, \tag{2.8}$$

where $\eta_x = \pi c_x^m/\tau$, $\eta_y = \pi c_y^m/\tau$ and I is the current input to the coil. K_x, K_y and K_z are exponential decay functions related to c_z^m. In [26], it is shown that the edge effect can be modelled using a modified third-order Fourier series by considering the amplitude and frequency to change with the levitation height. For example, F_x in the top edge region can be given by $F_x = IK_x \cos(\eta_x) f_1(c_y^m, c_z^m)$ where f_1 is the modified Fourier series. Due to the symmetry of the Halbach array, only three data-fit functions, f_1, f_2 and f_3, are needed to model the forces in all regions.

The torque from a coil in the central region can be modelled using the force found through the sinusoidal functions and an "effective torque arm". The torque on the mover in the central region is

$$\vec{T}_{\text{center}}(c_x^m, c_y^m, c_z^m) = \begin{bmatrix} r_{y1}^{\text{eff}} F_z - r_{z1}^{\text{eff}} F_y \\ -r_{x1}^{\text{eff}} F_z + r_{z2}^{\text{eff}} F_x \\ r_{x2}^{\text{eff}} F_y - r_{y2}^{\text{eff}} F_x \end{bmatrix}, \tag{2.9}$$

where F_x, F_y and F_z are the forces on the mover. Equations for the effective torque arms are all found through data fitting. In the edge and corner regions, modified third-order Fourier series also aid in modelling the torque. Due to the symmetry of the Halbach array, only four torque components found through data-fitting, t_1, t_2, t_3 and t_4, are needed to model the torque in all regions. For the maximum 36 coil activation of the mover in this research, the force and torques for all activated coils can be estimated within 90 µs, well under the desired 1 ms cycle time for the controller feedback loop.

Chapter 3

System Setup

3.1 Maglev System Setup

The stator and mover were designed, fabricated, and assembled by the team at the Maglev Microrobotics Laboratory. There are two separate systems used in this thesis, the first is a 64-coil prototype and the second is a much larger Magnetic Levitation Floor (MagFloor). The 64-coil prototype shown in figure 3.2 consists of an 8 by 8 array of square air-core coils spaced 76.2 mm (3 in.) apart for a total levitation area of 610 mm × 610 mm (24 in. x 24 in.). The coils are 75 mm wide, 86.5 mm tall, and have approximately 972 turns of 16 AWG wire. These coils are supported by an aluminum frame on top of a steel support structure which holds the current amplifiers. The current amplifiers can provide a maximum of 80 VDC and 10 A to each coil. The prototype also has mounting locations for the aluminum frame which holds the laser sensors, which is discussed in more detail in section 5.2.

The MagFloor is made of eight sections of a very similar design to the 64-coil prototype. Each section has an 8 by 12 array of square coils, for a total array 32 by 24 coils across the MagFloor, producing a levitation area of 2438 mm × 1829 mm (96 in. x 72 in.). There are four 5 kW power supplies which power the MagFloor, each connected to two of the stator sections. The MagFloor can provide a maximum of 80 VDC and 10 A to each coil, the same as the prototype. The stator structure is mounted on a lift in a pit which allows it to be lowered and covered when not in use so the room can be used for other purposes. When in use, it is raised so that its surface is approximately floor level, as shown in figure 3.3.

The mover contains a 2-D Halbach array with a six-by-six pole layout, for a total of 120 magnets. The permanent magnets are installed in an aluminum frame which provides structural rigidity. The total dimensions of the mover are 337 mm × 337 mm × 26 mm and it weighs approximately 6.6 kg. The frame also has mounting locations for the reflective markers for the cameras or for the flat plates for the laser sensors as shown in figure 3.1. When the flat plates are added to the mover, the total weight is approximately 7.0 kg.

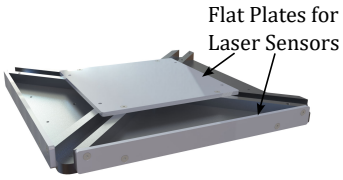

Figure 3.1: Mover image.

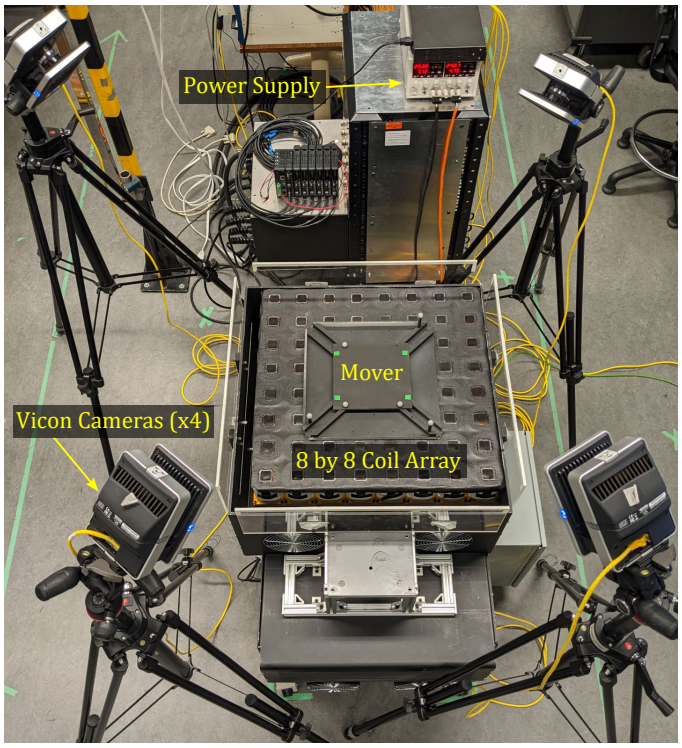

Figure 3.2: Overview of the 64 coil maglev prototype setup.

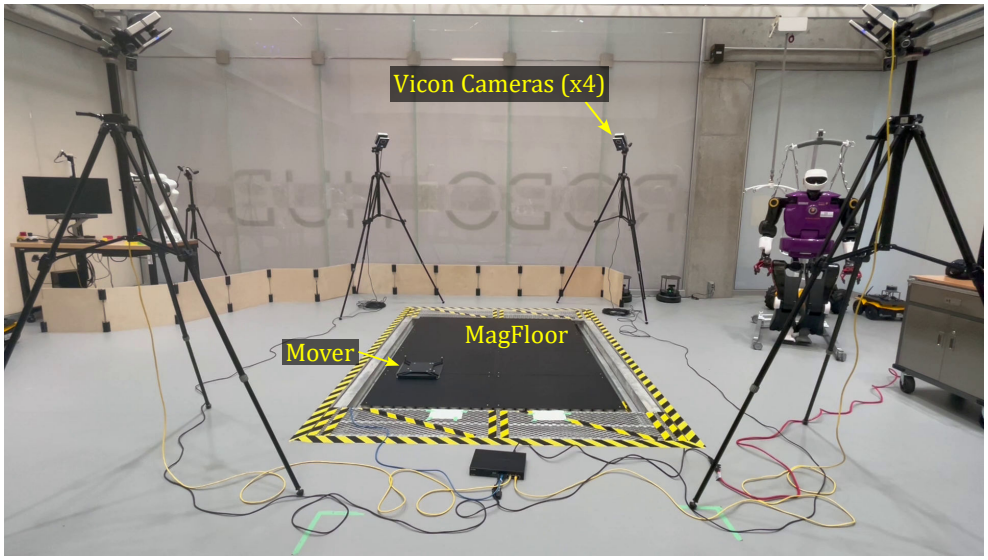

Figure 3.3: Overview of the MagFloor setup during operation.

3.2 Experimental Setup

A Beckhoff C6670-0010 industrial server is utilized to control the maglev system, for both the 64-coil prototype and the MagFloor. This acts as the programmable logic controller (PLC) to run the control code through TwinCAT 3. The controller scheme is designed in MATLAB/Simulink, exported to a TcCOM object, and imported into the TwinCAT project. Another TwinCAT program is dedicated to sending the control words to the current amplifiers to enable/disable them through their state machine and to send the current targets once enabled. The PLC communicates to the Technosoft iPOS8010 BX-CAT current amplifiers through the EtherCAT protocol at 2000 Hz, which is the maximum the amplifiers support. Although the Vicon system and control loop only operate at 1000 Hz, operating EtherCAT at 2000 Hz helps to reduce the system delay as the amplifiers receive the commands faster. See figure 3.4 for a diagram of the hardware connections for the maglev system.

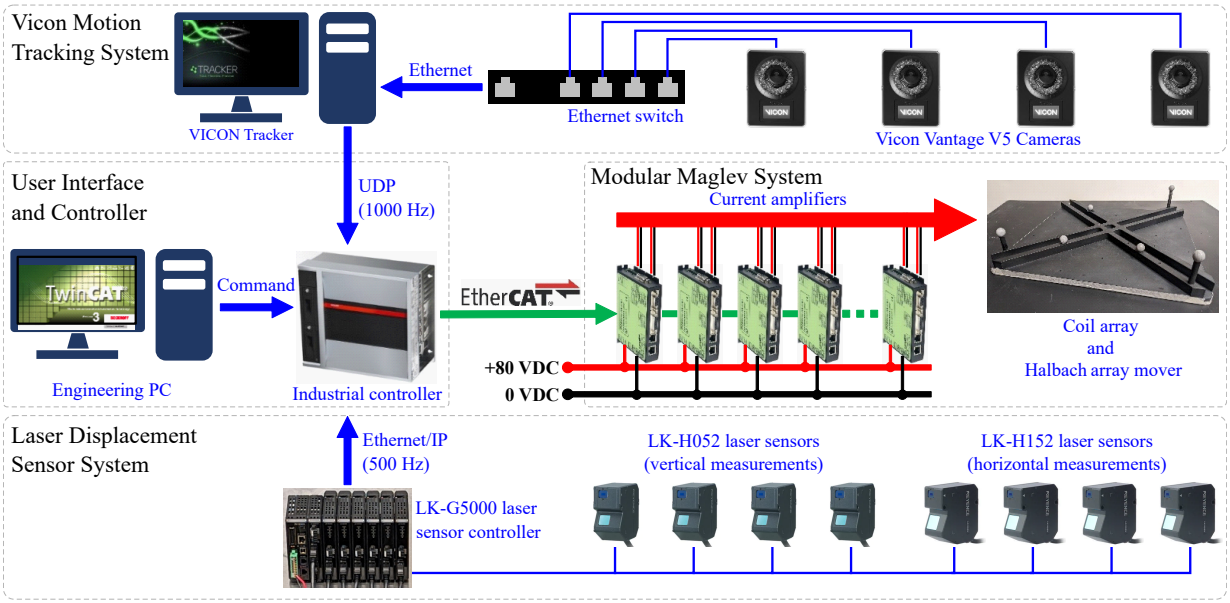

Figure 3.4: Hardware connection diagram.

On the 64-coil prototype, both the Vicon motion tracking system and laser displacement sensors were tested independently. The Vicon cameras are connected to an Ethernet switch which powers the cameras through Power over Ethernet (PoE). The cameras detect reflective markers mounted on the top of the mover and send the data to a PC running the Vicon Tracker software for processing. With at least three detected markers on the

mover, the system is able to determine the full 6-D position and orientation of the mover and sends this data via a User Datagram Protocol (UDP) data stream to the PLC at 1000 Hz. A TwinCAT task is dedicated to checking and parsing the UDP messages to send the position feedback to the controller task.

The eight laser displacement sensors are connected to a laser sensor controller which communicates with the PLC through Ethernet/IP at 500 Hz. The laser sensors only detect linear displacements, so further computation is needed to convert the readings into the 6-D position and orientation of the mover. This process is done in the Simulink task and is described in section 5.3. When using the laser displacement sensors on the 64-coil prototype, the Vicon cameras cannot be used simultaneously due to the large obstruction caused by the laser sensors and their mounting frame. As such, the two sensor systems were only tested independently and never simultaneously. The laser sensors were only tested on the 64-coil prototype, not the MagFloor.

A custom visualization interface was designed in TwinCAT for the control of the system during operation, as shown in figure 3.5. Before levitation, there are text boxes for modifying all the PID gains of the controller for each of the six axes. A feed-forward bias to the F_z force to offset the mass of the mover is also adjustable and was typically set at 62 N, just below the actual weight, so the integrator can quickly reach the actual value. The controller is discussed in more detail in chapter 4. For the later ILC tests discussed in section 7.3, commands were added for modifying the learning gains and loading and saving trajectory files.

To start operation, the current amplifiers can be enabled through their state machine by flipping the "Driver Enable" toggle. In preparation for a levitation, there is a button to toggle the integrator gains k_i of all axes to 0, except z. This ensures that integrators in other axes do not grow too large while the mover is resting on the stator with friction. To start a levitation, the "Simulink Enable" toggle is flipped to enable the current targets coming from the controller to be sent to the amplifiers. Once levitation is achieved, the k_i gains are toggled back on the fully enable the controller in all axes.

During levitation, there is a modifiable threshold called "Max Step" which controls when a new target is directly sent to the controller as a step input. If the new position target is further than the threshold from the previous target, then intermediate targets are generated as a smooth ramp with acceleration and deceleration periods until the final target is reached. The maximum step size, speed of the ramp, and acceleration at the start/end of the ramp are all modifiable with the visualization interface. There are also built-in trajectories such as a ramp, rectangle, ellipse, figure-eight, and others than can be started with the interface. There are options to modify the trajectory parameters such as

its dimensions and the number of loops. More details on trajectory generation are discussed in appendix A. When the "Log Path" checkbox is enabled under the "Path Toggle", data logging will automatically start and stop as the trajectory is sent so that it is in sync. Data logging can also be manually started via the "Log Data" toggle. This will log important variables to a .csv file on the PLC at a specified write period up to a maximum of 1000 Hz.

The visualization also displays useful data such as the measured 6-D position, control efforts, maximum current, estimated power consumption, and more. If the system automatically detects a problem, such as those discussed in section 3.4.2, the "Simulink Enable" toggle will flip off and targets of 0 A will be sent to all coils. The "Auto Disable Reset" will toggle on, preventing the system from being re-enabled unless this is manually toggled off.

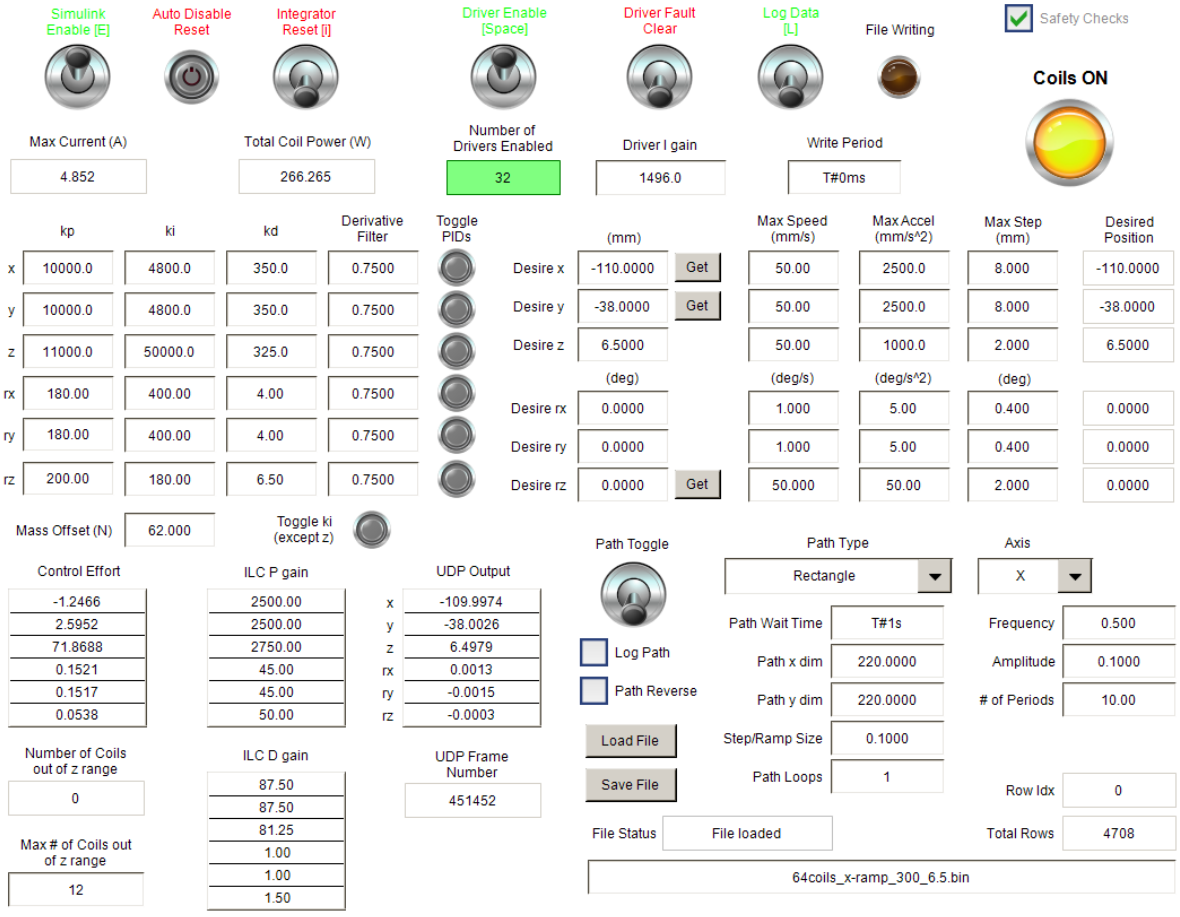

Figure 3.5: Custom TwinCAT visualization control interface during operation.

3.3 Current Amplifier Tuning and Testing

The current amplifiers each have their own internal PI controller which controls the output voltage of the amplifier to achieve the desired target current through the coil. The internal PI controller was configured to run at a frequency of 10 kHz, and the EtherCAT communication frequency to the PLC was set at the maximum 2000 Hz. This communication frequency is the maximum frequency at which the current targets can update using EtherCAT. An amplifier was tuned and tested using Technosoft's EasyMotion Studio software and an RS-232 connection, and then the same settings were saved and sent to all other current amplifiers using the File over EtherCAT (FoE) protocol in TwinCAT. After tuning the internal PI controller of the current amplifiers, the final gains were set to a k_p of 16.49 and a k_i of 1.7146, where the values of the gains are measured in internal units for the software. Converting to SI units using conversion factors in the documentation, the k_p is 65.96 V/A and the k_i is 68 584 V/(A·s). The following sections show step and frequency responses of an amplifier after tuning.

3.3.1 Amplifier Step Response

After tuning the PI controller in the current amplifier, step responses were tested using Technosoft's EasyMotion Studio software. This software allows step data to be recorded at the full 10 kHz of the internal PI controller. See figure 3.6 for step responses of a current amplifier connected to one of the square coils for test steps of 0.5 A, 1 A, 3 A and 5 A. The output voltage of the current amplifier is also shown with the right axis.

The rise time is defined as the time for the response to go from 10 % to 90 % of the steady-state value. For the four step responses tested, the rise time is about 0.2 ms for both the 0.5 A and 1 A steps, 0.6 ms for the 3 A step, and 1.2 ms for the 5 A step. The maximum voltage of the 0.5 A step is 36.1 V and well below saturation. For the 1 A step, the voltage reaches 72.2 V, which is just below saturation. The voltage saturates at 73.0 V for both the 3 A and 5 A step responses. Since the voltage does not saturate for small steps below 1 A, it makes sense that the rise time for those step responses was the same 0.2 ms. During levitation, the controller operates at 1000 Hz and produces a new set of current targets for each coil every 1 ms. Since the current targets have only small changes between time steps for smooth motions such as ramps, this means the current amplifiers can usually reach the new target before the next target is received.

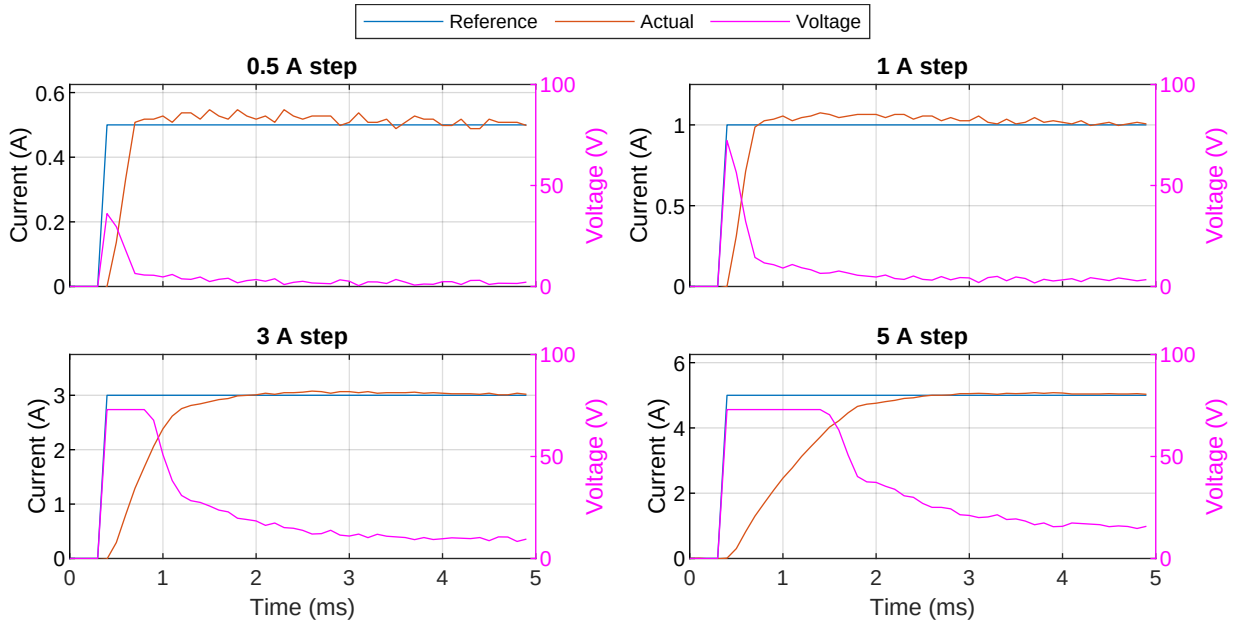

Figure 3.6: Step responses with control voltage for a current amplifier.

3.3.2 Amplifier Frequency Response

To test the current amplifier under sinusoidal responses, it was connected to the PLC with EtherCAT to send target sine waves of various frequencies. The current feedback from the amplifier was logged and the waveforms were compared. Using the current feedback, a sine wave at the same frequency was fit to the data in MATLAB to determine the relative amplitude and phase change compared to the input signal. This data was then used to generate a Bode plot.

An ideal Bode plot can also be generated from the closed loop transfer function $G_{cl}(s)$ setting $s = j\omega$ where ω is the frequency in radians, and the magnitude and phase are found from the resulting complex number. To find the closed-loop transfer function, a model of the plant (the coil) and the controller are needed. The electromagnetic coil connected to the current amplifier can be modelled as an inductor and resistor in series. The voltage can then be given by

$$V = L\frac{di}{dt} + Ri, \tag{3.1}$$

where L is the inductance of the coil, R is the resistance of the coil, V is the voltage and i

is the current. Taking the Laplace transform of this, the transfer function for the plant is

$$P(s) = \frac{I(s)}{V(s)} = \frac{1}{Ls + R}. \tag{3.2}$$

The transfer function of the PI controller is given by

$$C(s) = \frac{k_p s + k_i}{s}. \tag{3.3}$$

The closed-loop transfer function can then be found using the equation

$$G_{cl}(s) = \frac{P(s)C(s)}{1 + P(s)C(s)} = \frac{k_p s + k_i}{Ls^2 + (R + k_p)s + k_i}. \tag{3.4}$$

However, because of the EtherCAT communication, there is a time delay both in sending the current target from the PLC to the current amplifier and in receiving the current feedback back to the PLC. For example, the current target is generated and sent from the PLC in cycle 1, the current target is received by the amplifier and it starts to react in cycle 2, the updated current feedback will be sent in cycle 3, and the PLC will receive the updated current feedback in cycle 4. If the EtherCAT is running at 2000 Hz and considering cycle 1 to be time 0 ms, the PLC will receive the current feedback in cycle 4 at time 1.5 ms. As such, there is a minimum 1.5 ms delay between the waveform sent and received by the PLC. This time delay can be represented in the Laplace domain as $e^{-0.0015s}$, giving the theoretical transfer function as

$$G_{cl}(s) = e^{-0.0015s} \frac{k_p s + k_i}{Ls^2 + (R + k_p)s + k_i}. \tag{3.5}$$

To find the frequency response of the current amplifiers, reference sinusoidal waves were sent to the amplifier through EtherCAT at a communication frequency of 2000 Hz. These sinusoidal inputs ranged from frequencies of 0.9 Hz to 950 Hz for amplitudes of 1 A, 2 A, 3 A and 5 A. See figure 3.7 for example responses for a 2 A test at frequencies of 155.5 Hz, 311.9 Hz, 625.6 Hz and 950.0 Hz. For low frequencies, the response closely follows the reference, but with a delay of about 1.5 ms resulting from the EtherCAT communication. For high frequencies, such as the 950 Hz test shown in figure 3.7, the reference shown in blue starts to appear with a "beat" of varying amplitude due to the sampling of the reference at 2000 Hz. Since the full amplitude is reached in some cycles for the reference, if the response were to also reach it, the resulting curve fit could still approximately reproduce the full amplitude. For the 2 A amplitude test, the full amplitude cannot be reached at high frequencies.

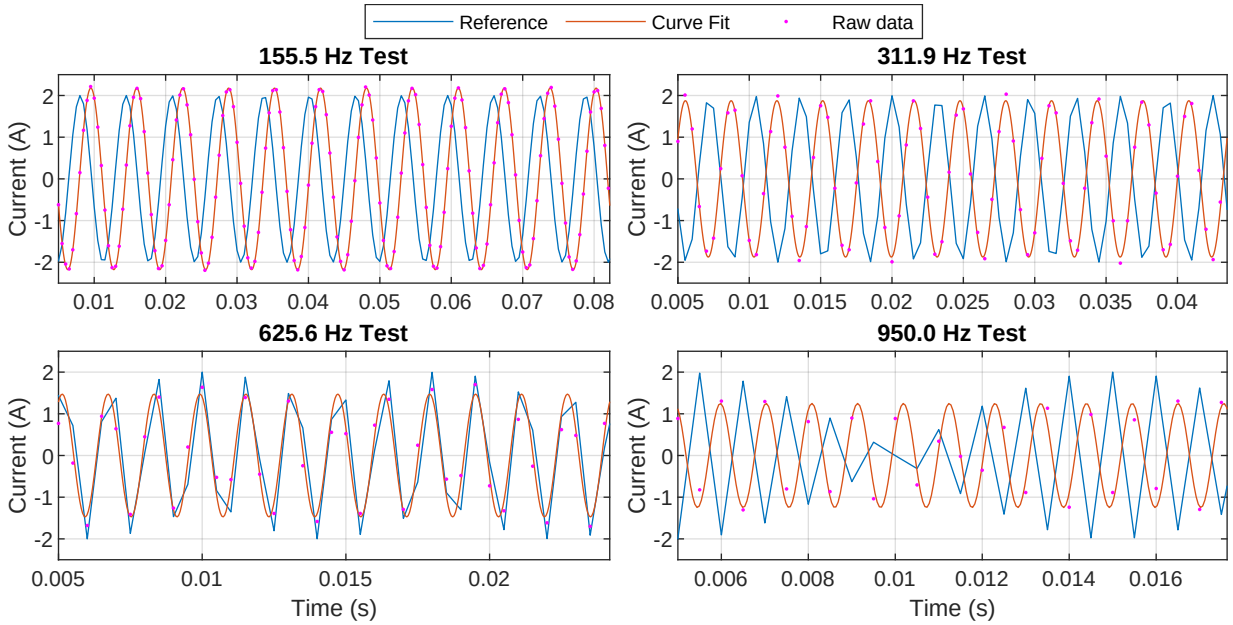

Figure 3.7: Response for 2A amplitude sinusoidal inputs at various frequencies.

For all frequencies, a sine wave is fit to approximately 500 data points from the test. For low frequencies, these data points were spaced out to be approximately 100 points per period of the sine wave, and for frequencies above 20 Hz, these points were spaced 0.5 ms apart at the maximum 2000 Hz cycle frequency of the EtherCAT. To avoid error from the delay at the start, the first 5 ms of data was ignored when doing the curve fit. The curve fit equation was

$$f(x) = a\sin(2\pi f x + \theta), \tag{3.6}$$

where the frequency f was set to be a constant using the known reference frequency, and the amplitude a and phase θ where the two unknowns from the curve fit. The magnitude for a Bode plot is the ratio of the measured amplitude over the reference a/a_{ref}, and the phase θ was adjusted by adding or subtracting multiples of 2π as needed to make the phase plot of the Bode plot continuous.

The resulting Bode plot from the frequency response tests is shown in figure 3.8. The "ideal" response as given by the continuous domain transfer function in equation (3.5) is also plotted, assuming $R = 2.6\,\Omega$, $L = 17\,\text{mH}$, and k_p and k_i are as given previously. In this plot, the magnitude is plotted in decibels (dB) using $|G(j\omega)|_{\text{dB}} = 20\log_{10}|G(j\omega)|$, the phase is given in degrees, and the frequency in hertz. The phase plot is dominated by the 1.5 ms time delay in the communication and as such drops off at high frequencies.

The bandwidth is defined as when the magnitude of the closed-loop response plot drops below −3 dB, which corresponds to a magnitude of 0.708. The bandwidth is approximately 756 Hz, 659 Hz, 432 Hz, and 236 Hz for the ideal case, 2 A, 3 A and 5 A amplitude tests, respectively. However, the magnitude plot of the 1 A never pass below −3 dB. This is because while the internal PI controller updates at 10 kHz, the current targets are only updating at 2 kHz through EtherCAT. As such, when a current target near the peak of the waveform is received, the amplifier has 0.5 ms to respond before the next target is received. As seen from the step responses in figure 3.6, the driver can respond to small steps in as little as 0.2 ms and thus the current feedback sent back to the PLC on the next EtherCAT cycle will have reached the target. If the targets were updated more frequently, the reference would decrease before the amplifier reaches it at high frequencies. This results in errors in both the magnitude and phase plots at high frequencies. The bandwidth decreases for higher amplitude sine waves because these amplitudes pass above the voltage saturation, so the amplifier is slower to respond and cannot reach the full amplitude at high frequencies.

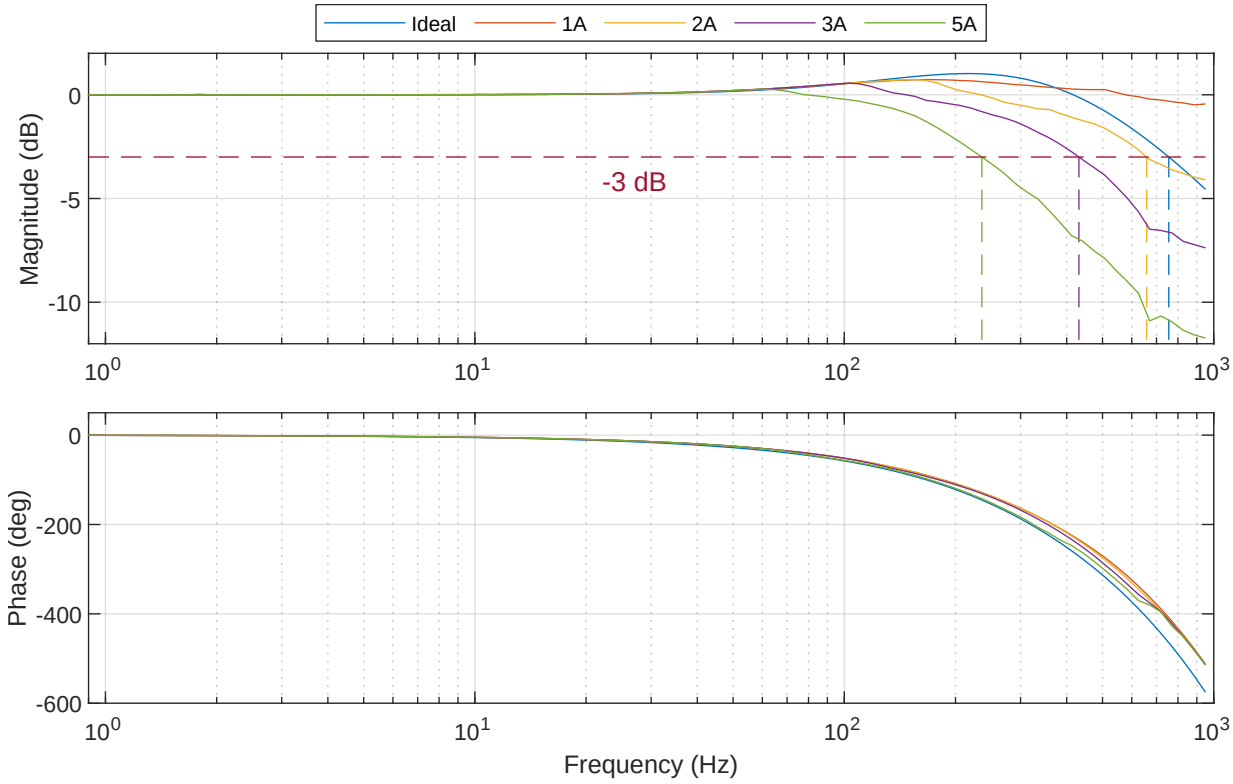

Figure 3.8: Bode plot of frequency response tests for a current amplifier.

3.4 Safety Precautions

3.4.1 Automated Amplifier Testing

An automated test of the current amplifiers is run each time before running the maglev system. This can identify communication issues to each amplifier and wiring problems on either the input or output side of the amplifier, such as if a coil becomes disconnected. This is especially important for the MagFloor where the system is on a lift with the connections coming off the side to the walls of the pit. This test was custom designed and coded in separate TwinCAT projects from the levitation code. See figure 3.9 for the TwinCAT visualization during a test of the 32 amplifiers in the 64-coil prototype.

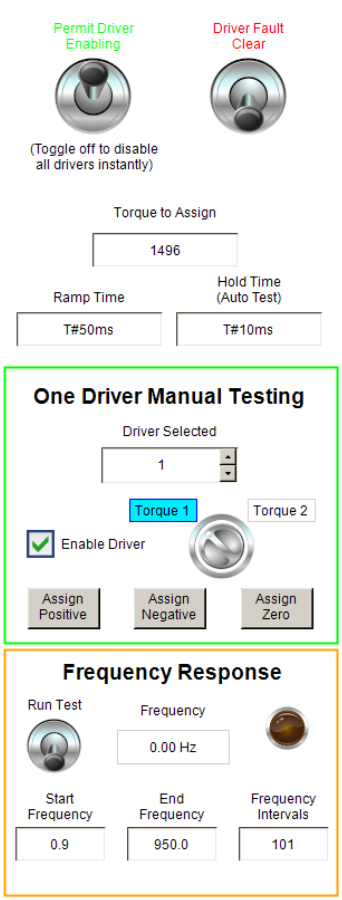

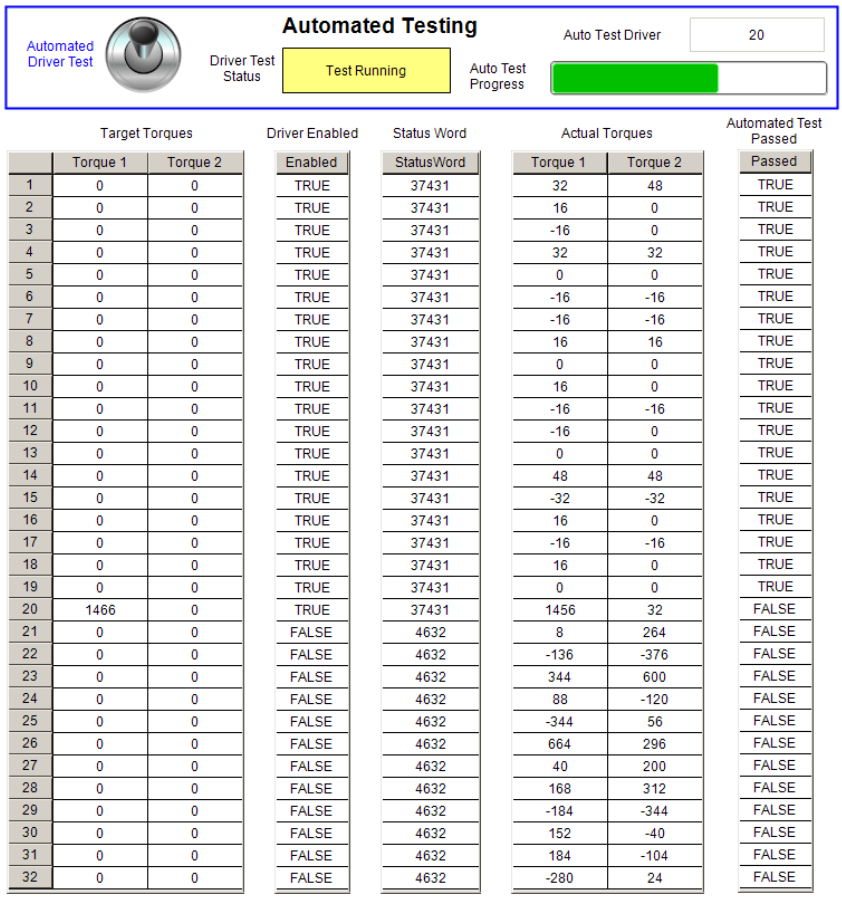

	Target Torques		Driver Enabled	Status Word	Actual Torques		Automated Test Passed
	Torque 1	Torque 2	Enabled	StatusWord	Torque 1	Torque 2	Passed
1	0	0	TRUE	37431	32	48	TRUE
2	0	0	TRUE	37431	16	0	TRUE
3	0	0	TRUE	37431	-16	0	TRUE
4	0	0	TRUE	37431	32	32	TRUE
5	0	0	TRUE	37431	0	0	TRUE
6	0	0	TRUE	37431	-16	-16	TRUE
7	0	0	TRUE	37431	-16	-16	TRUE
8	0	0	TRUE	37431	16	16	TRUE
9	0	0	TRUE	37431	0	0	TRUE
10	0	0	TRUE	37431	16	0	TRUE
11	0	0	TRUE	37431	-16	-16	TRUE
12	0	0	TRUE	37431	-16	0	TRUE
13	0	0	TRUE	37431	0	0	TRUE
14	0	0	TRUE	37431	48	48	TRUE
15	0	0	TRUE	37431	-32	-32	TRUE
16	0	0	TRUE	37431	16	0	TRUE
17	0	0	TRUE	37431	-16	-16	TRUE
18	0	0	TRUE	37431	16	0	TRUE
19	0	0	TRUE	37431	0	0	TRUE
20	1466	0	TRUE	37431	1456	32	FALSE
21	0	0	FALSE	4632	8	264	FALSE
22	0	0	FALSE	4632	-136	-376	FALSE
23	0	0	FALSE	4632	344	600	FALSE
24	0	0	FALSE	4632	88	-120	FALSE
25	0	0	FALSE	4632	-344	56	FALSE
26	0	0	FALSE	4632	664	296	FALSE
27	0	0	FALSE	4632	40	200	FALSE
28	0	0	FALSE	4632	168	312	FALSE
29	0	0	FALSE	4632	-184	-344	FALSE
30	0	0	FALSE	4632	152	-40	FALSE
31	0	0	FALSE	4632	184	-104	FALSE
32	0	0	FALSE	4632	-280	24	FALSE

Figure 3.9: TwinCAT visualization for amplifier testing.

The automated test iterates through each amplifier to perform the following steps:

1. Attempt to enable the amplifier through its state machine,
2. Send a $+1$ A current target to output 1 and check the current feedback,
3. Send a -1 A current target to output 1 and check the current feedback,
4. Send a $+1$ A current target to output 2 and check the current feedback, and
5. Send a -1 A current target to output 2 and check the current feedback.

The target currents are smoothly increased using a ramp over 50 ms, then held for 10 ms, and using a 10-element moving average, the actual current is compared to the target. If within about 0.03 A, the check will pass. It then smoothly decreases the target current back to 0 before doing the next test. If there are wiring issues on the input side of the amplifier, these will usually be detected when trying to enable the amplifier. Wiring issues on the output side may not be detected until attempting to send a target current. Because the current amplifiers normally act as motor controllers, instead of directly sending a target current, a target "torque" is sent instead. The torque tick-to-current ratio was checked for all 32 amplifiers on the prototype system and was found to be $1496 \pm 2\%$ ticks/A. This TwinCAT project also allows for sending sinusoidal targets to an amplifier as was done during the frequency response tests in section 3.3.2.

3.4.2 Automatic Shut-Offs

Once operation is started to do a levitation, there are automatic shutoffs built-in to the TwinCAT code. If any of the safety checks fail, the system will automatically send 0 A current targets to all coils to prevent the mover from flying uncontrollably. It will only re-enable from manual user input. The system will automatically disable itself if

1. The measured position has not been updated for the past 5 frames,
2. The x or y position of the mover is more than 25 mm from the target (10 mm with the laser sensors),
3. The yaw rotation γ of the mover is more than 5° from the target, or
4. More than 12 active coils are outside of the valid c_z^m range of 0 mm to -8 mm for the force and torque model.

Instead of checking the roll, pitch, and z position of the mover directly, the system checks if the z position of each active coil transformed into the mover's coordinate system is within the valid range. If the mover goes too high or rotates too far on either the roll or pitch, this check will fail. The check is done in this manner as it is a more relevant condition for the force and torque model described in section 2.4, which was trained on data collected between levitation heights of 0.5 mm to 7.5 mm. Note that the z position of a coil in mover coordinates can be greater than 0 (above the bottom of the mover) if the mover is very tilted since the coil activation area is larger than the mover. See figure 3.10 for an example of an automatic shut-off during an unstable ramp motion before the PIDs were fully tuned. The mover comes to rest on the stator after the shut-off.

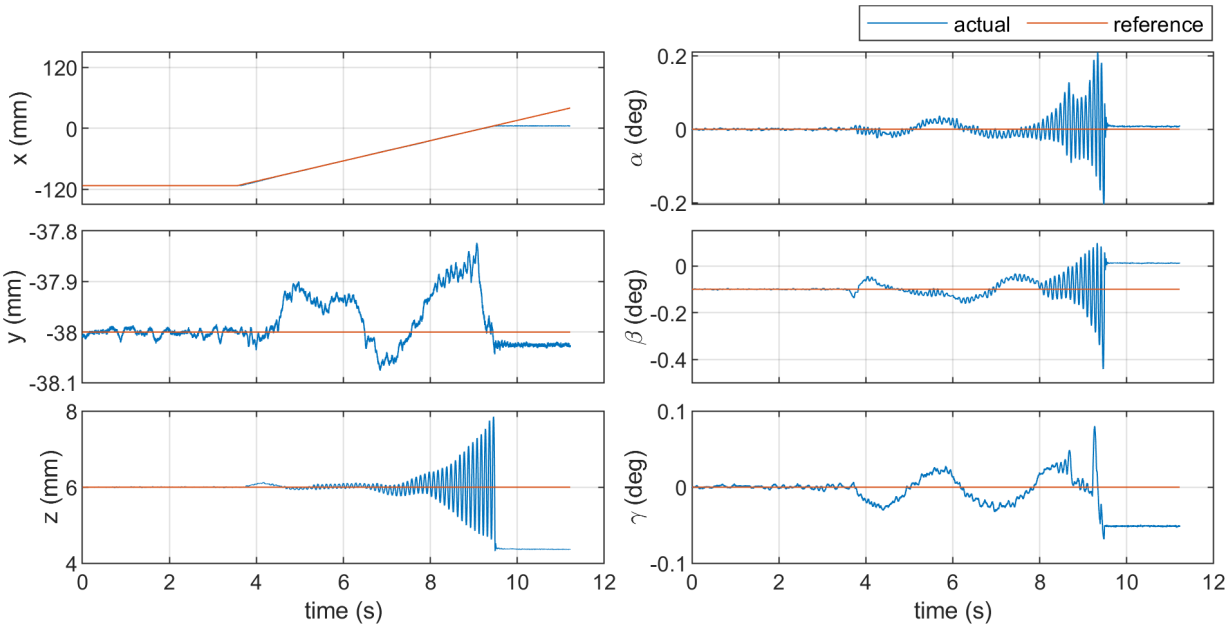

Figure 3.10: Example of automatic shut-off during unstable motion.

There are limits to what the user is allowed to enter for the position targets. For example, it is not allowed to enter an x or y target that would cause the edge of the mover to go past the edge of the stator. In the case of a long ramp motion, the system compares the current position to the next intermediate target along the ramp, which is generated at the full 1000 Hz of the controller. Therefore, if the mover falls more than a threshold behind the ramp motion, the system will disable itself. This can happen if the speed of the ramp is too fast and the system cannot keep up. In actuality, too many coils may saturate before this happens, causing the power supply to trip.

Each power supply has a current limit and if the overall system is drawing too much power, the power supply will automatically cut its output. The current amplifiers will then detect the low input voltage and automatically go to a disabled state. The current amplifiers can also detect shorts on their outputs directly and automatically disable them. The TwinCAT code will detect the amplifier has disabled itself and will not attempt to re-enable the amplifier until the user manually clears the fault. On the 64-coil prototype, the output current limit of the power supply was set to 30 A, and on the MagFloor, the output current limit was set to 40 A on each of the 5 kW power supplies.

3.4.3 Other Safety Features

On the 64-coil prototype, there is also an acrylic fence surrounding the levitation area to prevent the mover from flying off the system, as shown in figure 1.2. On the MagFloor, there is an aluminum mesh on the sides of the stator to prevent the mover from falling into the pit. Since the mover only levitates a few millimetres, if it were to leave the stator, it would quickly touch the mesh or the edge of the pit, and would not travel far. As shown in figure 3.11, there is also a mechanical fence to prevent people from getting too close to the MagFloor, with a nylon net attached as an extra precaution to stop the mover. As future work of the maglev team, it is planned to replace the net with a smaller and more secured fence around the edge of the MagFloor pit. On the Power Control Panel placed on the wall of RoboHub, there is an emergency stop button to kill all power to the system as well as a switch for controlling the DC output of the power supplies, shown in figure 3.12. There is another emergency stop by the podium control station, and limit switches at the edges of the pit to detect if the floor panel is covering the pit.

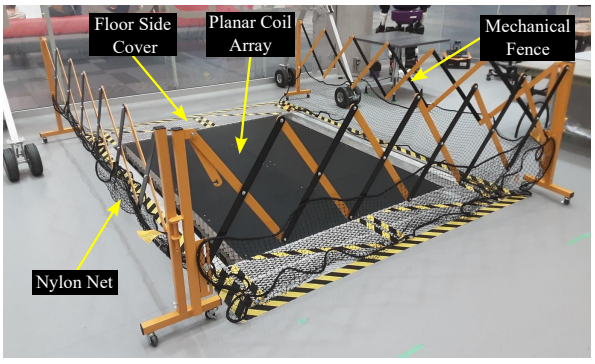

Figure 3.11: Protective fence around the MagFloor.

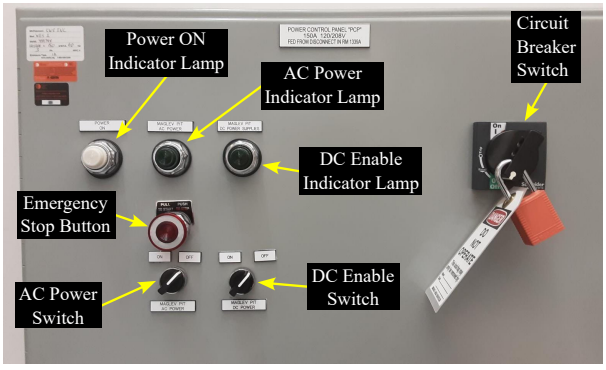

Figure 3.12: Power control panel for the MagFloor.

Chapter 4

Controller Design

4.1 Overview of the Control Loop

An overview of the closed-loop controller is presented in figure 4.1. Within TwinCAT, a 6-D position and orientation target $\vec{m}^g_{\text{ref}} = \begin{bmatrix} x & y & z & \alpha & \beta & \gamma \end{bmatrix}^T$ is generated at each 1 ms cycle of controller. Taking the difference with the measured position $\vec{m}^g_{\text{act}}$, the 6-D position error, $\vec{e^g} = \vec{m}^g_{\text{ref}} - \vec{m}^g_{\text{act}}$ is input to six independent discrete PIDs, one for each axis. The output of these PIDs is the control effort $\vec{w}$, which is the desired forces and torques to be applied to the mover in each axis. For the z axis, a feed-forward bias is added to the control effort equal to the weight of the mover $F_{z,\text{bias}} = mg$, which is approximately 65 N. Adding this bias reduces the delay for the integrator in the z axis to build up, and enables the mover to levitate almost immediately once the coils are activated. For the ILC tests discussed in section 7.3, a feed-forward control effort is also added after learning from previous iterations. The resulting net control effort $\vec{w}_{\text{net}}$ is in global coordinates and used to determine the coil currents through the direct wrench method. The current targets are then sent to the current amplifiers, which actuate the maglev system.

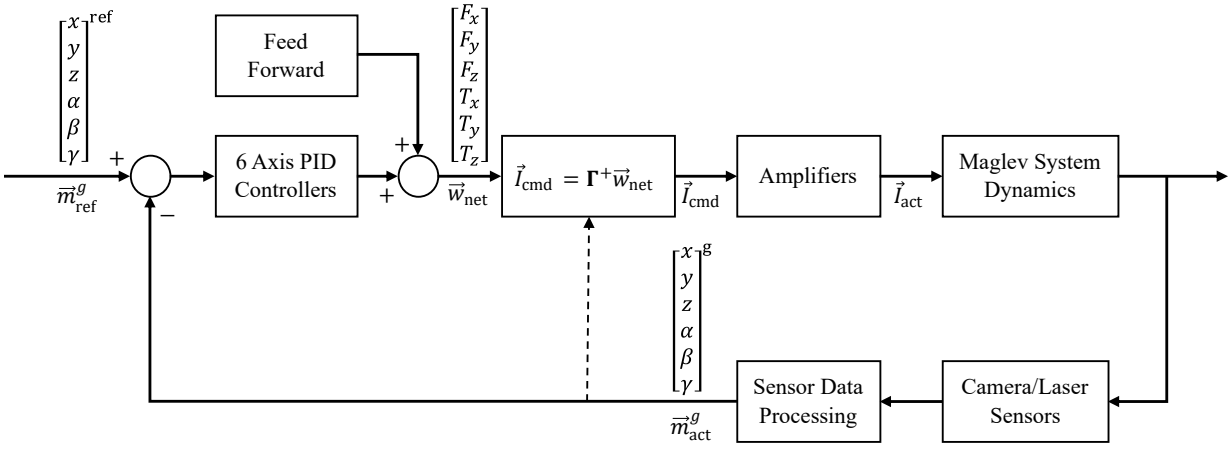

Figure 4.1: Overall control diagram for the maglev system.

The basic PID includes three terms: a proportional term, an integral term, and a derivative term. Each of these terms is with respect to the error $\vec{e^g}$ and is multiplied by a gain k_p, k_i, and k_d, respectively. The proportional term scales the control effort with respect to the size of the position error. The derivative term helps ensure stability by resisting the motion. For example, if the error is decreasing too quickly, the control effort is reduced. During a smooth ramp motion, the derivative can also add to the control effort to help initiate or stop the motion. The integral term serves to eliminate steady-state error and also aids in catching a target ramp.

The PID gains used in each of the experimental setups are shown in table 4.1. Note that the 6-D position is converted into SI units (m and rad) before being sent to the controller. The gains are very similar between the different setups, however, some changes were made from the initial tuning done on the 64-coil prototype using the camera motion tracking system. Since the cameras in the MagFloor are placed farther away, this results in less accurate measurements and more steady-state error. To compensate, the integral gains were increased. This also helps to quickly catch the ramp motions during large trajectories across the MagFloor. Some of the gains on the α and β rotation axes were also raised when using the laser sensors, since the laser sensors have less noise in those axes, allowing greater derivative gain. Note that the controller was still run at 1000 Hz with the laser sensors even though they update at 500 Hz to help avoid missed measurements caused by sync issues.

Table 4.1: PID gains for each of the six axes of the three experimental setups.

		x	y	z	α	β	γ
			N/m			N·m/rad	
P gain k_p	64 Coils Cameras	10000	10000	11000	180	180	200
	64 Coils Lasers	10000	10000	11000	180	180	200
	MagFloor Cameras	9000	9000	11000	180	180	220
			N/(m·s)			N·m/(rad·s)	
I gain k_i	64 Coils Cameras	4800	4800	50000	400	400	180
	64 Coils Lasers	4800	4800	50000	600	600	180
	MagFloor Cameras	35000	35000	50000	600	600	600
			N·s/m			N·m·s/rad	
D gain k_d	64 Coils Cameras	350	350	325	4	4	6.5
	64 Coils Lasers	350	350	325	6	6	6.5
	MagFloor Cameras	350	350	325	6	6	6.5

4.2 Improving the Derivative

The default discrete derivative used in a PID is given by

$$u_d(t_n) = k_d \frac{e(t_n) - e(t_{n-1})}{T_s} \tag{4.1}$$

where $e(t_n)$ and $e(t_{n-1})$ are the errors at the current and previous time step, k_d is the derivative gain, $u_d(t_n)$ is the derivative control effort and T_s is the sample time, which is 0.001 s at 1000 Hz. There are a few problems with using this derivative function without any modification or filtering. The first problem is that this function assumes smooth changes in the reference, so any step change will result in derivative kick. Secondly, any noise in the input signal is amplified by taking the derivative, which for the noisy measurements from the camera-based motion tracker, results in noisy control efforts. The final issue is that this is taking the derivative of the error directly, which assumes that the reference position and the measured position are from the same time step and change continuously. Due to sync issues between the sensor systems and the PLC, it is possible that the controller will sometimes see a duplicate measurement or miss a sensor cycle, which would cause spikes in the derivative. In this section, modifications to the derivative computation are discussed to resolve these issues.

4.2.1 Resolving Derivative Kick

When a step input is given to the controller, for example, if the x position is increased by 8 mm in a time step, then the derivative in the reference at that instant is 8 m/s for a sample time of 1 ms. This is a very fast instantaneous motion, which will result in a large spike in the derivative at that time step. This spike can cause a control effort beyond the system's ability to produce and saturate all active coils, potentially causing instability or even tripping the power supply.

One common method to remove derivative kick is to take the derivative of the negative of the measurement only, ignoring the change in reference. This works well for step inputs but causes an additional problem during a ramp motion. Since the change in reference is ignored, the derivative is constantly trying to hold back the motion during a ramp, resulting in the integrator needing to grow larger to compensate and produce a large overshoot at the end of the ramp.

The solution to derivative kick used in this research is to set the change in reference to 0 only when a step change is detected, by using a threshold. The derivative is first

calculated by taking the derivative of the reference and the measurement separately and then taking the difference between them. If the absolute value of the derivative of the error is greater than both a threshold and the derivative of the measurement alone, then the change in reference is ignored. This threshold is approximately set to avoid saturating the coils. Algorithm 4.1 shows this process of killing derivative kick in lines 8–11.

4.2.2 Filtering the Derivative

To reduce the effect of measurement noise on the derivative, a low-pass filter is added after taking the derivative. In the z-domain, the filter is of the form

$$G(z) = \frac{\frac{T_s}{T} z}{z - (1 - \frac{T_s}{T})}, \tag{4.2}$$

where T_s is the sample time of 1 ms and T is an approximate time constant for the filter. The time constant was chosen to be 2 ms for the 64-coil prototype and 4 ms for the MagFloor. Using the MagFloor as an example, the filter is then

$$G(z) = \frac{0.25z}{z - 0.75}. \tag{4.3}$$

Converting this into the time domain, the filter equation is then

$$y(t_n) = 0.75y(t_{n-1}) + 0.25x(t_n), \tag{4.4}$$

where x is the input to the filter and y is the output of the filter. The low-pass filter is shown on line 12 of algorithm 4.1.

Figure 4.2 demonstrates the effect of the derivative filter during x-ramps of 400 mm/s on the 64-coil prototype. The lower plot shows the derivative of the error in x, which is highest at the start and ends of the ramp motion. For this test, the discrete low-pass filter was set to a time constant of 2 ms, which is shown to approximately reduce the noise of the derivative in half. Further increasing the filter would result in less noise entering the derivative, but has the disadvantage of increasing the delay. Since this system already has a significant delay, adding more delay is very undesirable. Using the bigger filter with a time constant of 4 ms on the MagFloor is necessary because of the greater measurement noise, and the system is shown to still be stable.

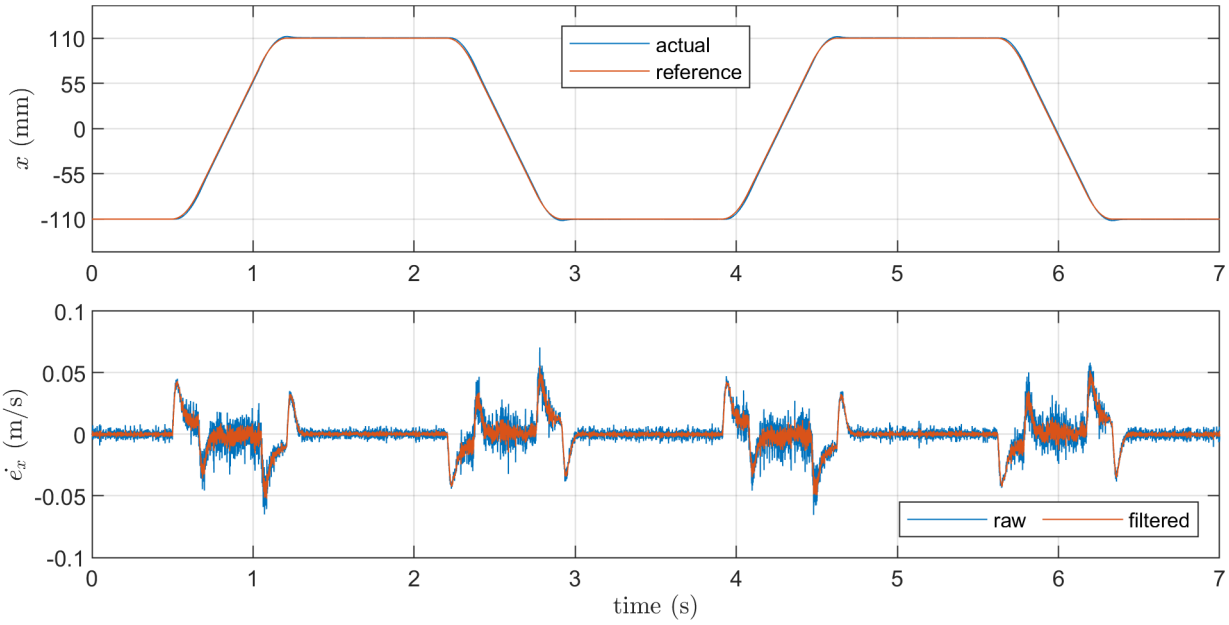

Figure 4.2: X-ramp on 64 coils with the derivative before and after the filter.

4.2.3 Resolving Derivative Sync Issues

Although the sensor systems operate at around 1000 Hz for the camera system and 500 Hz for the laser sensors, this is an approximate value and the time between each frame can vary slightly. This is shown in figure 4.3, where for a slightly longer frame, the next cycle of the controller may start before the measurement data has updated, resulting in the controller using the same measurement data as the last cycle. It is also possible that the controller misses a sensor frame if the sensor updates twice in the previous cycle. These two issues commonly come in pairs, with a duplicate frame and then a skipped frame.

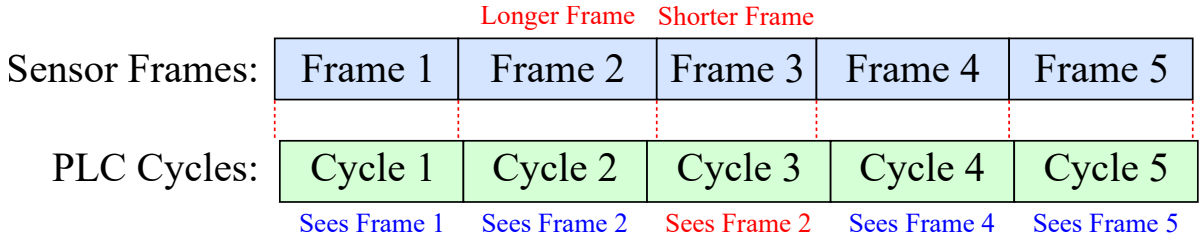

Figure 4.3: Syncing between sensor cycles and PLC cycles.

This syncing issue between the sensor's and the PLC's cycle time can cause problems when computing the derivative. This is shown in figure 4.4, where the top plot shows a ramp motion in the x axis at 0.4 m/s and the lower plot shows the computed derivative of the error. When the controller uses a duplicate measurement from the last frame, this means that the derivative of the measurement jumps to 0, so the derivative of the error will jump to the change in reference, which is about 0.4 m/s in this case. This is shown by the upward spikes in the plot. When a sensor frame is skipped, the change in the measurement is double what it should be, resulting in the downward spikes shown in the plot.

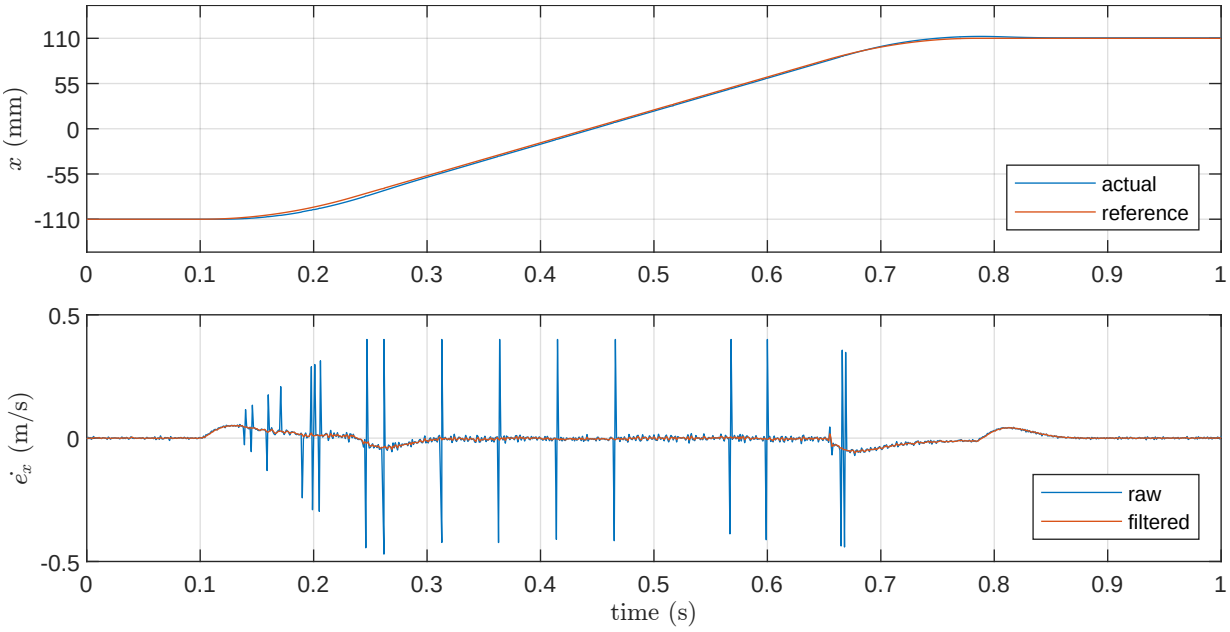

Figure 4.4: Example of sync issues causing derivative spikes during ramp.

To resolve this sync issue, the derivatives of the reference and the measurement are computed separately. Since the reference targets are generated within TwinCAT, there is never any sync issue with them, and the reference derivative can be computed normally. The derivative of the measurement is then computed using the difference between the current measurement and the last different measurement, and the time step is multiplied by the number of frames between them. The last different measurement may not be from the previous PLC cycle. Both the Vicon camera system and the laser sensor system send a count that increments with each cycle along with the data. This count is used to determine how many frames have passed between measurements. If the measurement hasn't been updated, then the measurement derivative from the last cycle is kept to avoid

it jumping to 0. Algorithm 4.1 shows the overall method for computing the derivative on the MagFloor. Note that for the laser sensors, a sample time of $T_s = 2\,\text{ms}$ is used to compute the derivative of the measurement as the laser sensors update at 500 Hz. The low pass filter is shown with a time constant of 4 ms in the algorithm, but a time constant of 2 ms is used for the 64-coil prototype.

Algorithm 4.1 Algorithm for calculating the derivative.

$\dot{r}_n \leftarrow \frac{r_n - r_{n-1}}{T_s}$
$r_{n-1} \leftarrow r_n$
if $f_n > f_{n-1}$ **then** ▷ The sensor frame number has updated
    $\dot{x}_n \leftarrow \frac{x_n - x_{n-1}}{(f_n - f_{n-1})T_s}$
    $x_{n-1} \leftarrow x_n$ ▷ Update previous variables
    $f_{n-1} \leftarrow f_n$
end if
$\dot{e}_n = \dot{r}_n - \dot{x}_n$
if $|\dot{e}_n| > |\dot{x}_n|$ and $|\dot{e}_n| \geq e_{\text{thresh}}$ **then** ▷ Detect step input
    $\dot{e}_n = -\dot{x}_n$
end if
$\dot{e}_{n,\text{f}} \leftarrow 0.75\dot{e}_{n-1,\text{f}} + 0.25\dot{e}_n$ ▷ Low-pass filter
$\dot{e}_{n-1,\text{f}} \leftarrow \dot{e}_{n,\text{f}}$
$u_d \leftarrow k_d \dot{e}_{n,\text{f}}$

4.3 Coil Selection and Current Decoupling

The direct wrench method allows the decoupling of the forces and torques to determine the target current in each coil. A wrench transformation matrix $\mathbf{\Gamma}$ contains, in each column, the force and torque contribution for each coil per 1 A of current. The matrix $\mathbf{\Gamma}$ is generated using the force and torque model described in section 2.4 and considering the relative position of each coil in the mover's coordinate system. Performing a matrix multiplication of the wrench transformation matrix $\mathbf{\Gamma}$ with a vector of coil currents will then give the net force and torque on the mover,

$$\vec{w}_{\text{net}} = \begin{bmatrix} F_{x,1} & F_{x,2} & \dots & F_{x,n} \\ F_{y,1} & F_{y,2} & \dots & F_{y,n} \\ \vdots & & \ddots & \vdots \\ T_{z,1} & T_{z,2} & \dots & T_{z,n} \end{bmatrix} \begin{bmatrix} I_1 \\ I_2 \\ \vdots \\ I_n \end{bmatrix} = \mathbf{\Gamma}(\vec{c^m})\vec{I} \tag{4.5}$$

where n is the number of active coils. Since there are always more than six coils being activated, the six DOF motion is always over-actuated. To determine the target currents from the known wrench transformation matrix $\mathbf{\Gamma}$ and desired forces and torques $\vec{w}_{\text{net}}$, the Moore-Penrose inverse can be utilized. Using this pseudoinverse, the solution minimizes energy consumption. The control current can therefore be found using

$$\vec{I} = \mathbf{\Gamma}^{+}\vec{w}_{\text{net}} = \mathbf{\Gamma}^{T}(\mathbf{\Gamma}\mathbf{\Gamma}^{T})^{-1}\vec{w}_{\text{net}}. \tag{4.6}$$

However, both the wrench transformation matrix $\mathbf{\Gamma}$ and the force and torque vector $\vec{w}_{\text{net}}$ must be in the same coordinate system. Since the wrench transformation matrix is computed in the mover coordinates, it is more computationally efficient to transform the global force and torques from the PID controllers into the mover coordinate system using

$$\vec{w}^{\,m}_{\text{net}} = \mathbf{R}^{m}_{g}\vec{w}^{\,g}_{\text{net}}. \tag{4.7}$$

To speed up the computation, active coils are first selected based on the position of the mover and whether the coil offers any significant force or torque. For simplicity, a coil will be activated if the coil center is within a 16 in. by 16 in. square of the mover center, where the activation square rotates with the mover. This means that if the edge of a coil passes under the edge of the mover, the coil will be activated, as shown in figure 4.5.

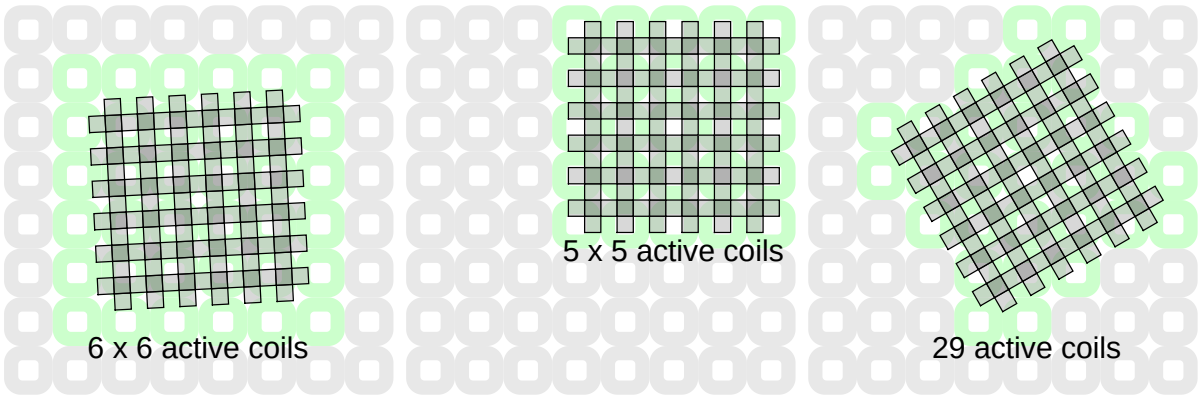

Figure 4.5: Coil activation with various mover locations. Active coils are shown in green.

Coils that are not active will either have their force and torque contribution set to 0 in the wrench transformation matrix, or those coils will not be included in the matrix at all. For the MagFloor, the wrench transformation matrix is a fixed size of 6 rows by 36

columns for a maximum of 36 active coils. The resulting 36-element current vector is then mapped to a larger current vector which includes all 768 coils. This process allows easy extension of the stator by adding more coils with virtually no change in computation time.

4.3.1 Current Recalculation When Saturated

Due to the nature of the pseudoinverse, the target current map tries to minimize the total energy to produce the desired forces and torques on the mover. This minimal energy solution may involve large currents in a few coils that are well positioned below the magnet array at that time step. If the magnitude of these few target currents is above the allowable current limit, then they will be saturated to the limit to avoid damaging the system or blowing any fuses on the coils. Although the fuses between the current amplifiers and coils are rated for 10 A, the current is limited between -9 A to 9 A in the code to provide a buffer to account for uncertainties. When coils are saturated to the limit, then the resulting net force and torque on the mover will not match that which was desired. However, it could be possible to still achieve the desired force and torque on the mover by increasing the current in other coils which are below saturation, since the system is over-actuated. This resulting solution would consume more energy than the original current targets even if they were not saturated.

The current map is recalculated when one or a few coils are saturated. First, the original coil map is calculated using equation (4.6) and the Moore-Penrose inverse as described earlier. Then, the coil numbers are stored for any current targets which are above their saturated value

$$\vec{N}_{\text{idx}} = \arg(|\vec{I}| > |\vec{I}_{\text{sat}}|). \tag{4.8}$$

Using the wrench transformation matrix and the saturated current vector for only the saturated coils, the total force and torque contribution of the saturated coils is found

$$\vec{w}_{\text{sat}} = \mathbf{\Gamma}(:, \vec{N}_{\text{idx}})\vec{I}_{\text{sat}}(\vec{N}_{\text{idx}}). \tag{4.9}$$

This force and torque contribution is subtracted from the net desired force and torque to obtain the remaining force and torque from the other coils, $\vec{w}_{\text{rem}} = \vec{w}_{\text{net}} - \vec{w}_{\text{sat}}$. The pseudoinverse is then taken of the new wrench transformation matrix which only includes the unsaturated coils and new target currents are found using the remaining force and torque vector

$$\vec{I}_{\text{rem}} = \mathbf{\Gamma}^{+}_{\text{rem}}\vec{w}_{\text{rem}}. \tag{4.10}$$

A final current vector is then compiled using the new targets for the unsaturated coils and the saturated currents for the saturated coils. This process is repeated until the net

force and torque after saturation matches the desired force and torque from the controller. However, if 8 or more coils are saturated, then this process is stopped as raising any more currents may trip the power supply so there is no need to continue calculating in this case.

4.4 Additional Controller Functions

4.4.1 Extending to Infinite Yaw Rotation

The yaw rotation angle measured by the Vicon camera system is limited to the range of $-180°$ to $180°$. When the mover rotates past this limit, for example rotating from $179°$ to $181°$, the measurement will jump to $-179°$. This discontinuity would cause instability in the controller and makes targeting yaw rotation angles close to the bounds difficult. In order to resolve this issue, the yaw rotation angle is extended to be of unlimited range before passing into the controller. This is done by taking the difference between the previous measurement and the current to compute the number of rotations different between them. For example, the difference between a previous measurement of $179°$ and a current measurement of $-179°$ is close to $360°$, or one revolution. As such, one revolution is added to the current measurement, $-179° + 360° = 181°$, to remove the discontinuity. This process is shown in algorithm 4.2. Using this method, any number of rotations can be achieved, and a reference target of, for example, $\gamma_{\text{ref}} = 720°$ can be sent to the controller to perform two revolutions.

Algorithm 4.2 Algorithm for extending the yaw rotation angle in degrees.

1: $N_{\text{revs}} \leftarrow \text{round}((\gamma_{n-1} - \gamma_n)/360)$ ▷ Store number of rotations
2: $\gamma_n \leftarrow \gamma_n + 360N_{\text{revs}}$ ▷ Add rotations to current yaw
3: $\gamma_{n-1} \leftarrow \gamma_n$ ▷ Update previous yaw

4.4.2 Using Measurements of Coil Locations

When finding the force and torque contribution of each coil on the mover, the location of each coil in the mover's coordinates is used. Thus, it is necessary to have a map of the locations of all coils. The simplest approach would be to assume an ideal 76.2 mm (3 in.) spacing for the coils based on their dimensions. However, due to fabrication difficulties and tolerance errors, the spacing of the coils is slightly greater since there is some additional space between the coil modules. To resolve this, on the 64-coil prototype, the location of

every coil was measured with reference to the global coordinates using the Vicon motion tracking system and a custom block which fit into the core of the coil and held a reflective marker. Thus, a map of the x and y locations of every coil was created and is utilized in the code. The height of each coil was assumed to be the same on the 64-coil prototype.

On the MagFloor, the coil locations were more complicated since the MagFloor is composed of eight sections, each with twelve modules of eight coils. The top surfaces of each of these eight sections were not perfectly level or aligned with each other and there is about $\pm 2\,\text{mm}$ variation between the heights of the top surface of the coils. For the MagFloor, the locations of each of the four corners of the eight sections were measured for a total of 32 (x, y, z) coil locations. Then, the location of each of the coils within a section was interpolated between its four corners to obtain a map of (x, y, z) locations for all coils.

Because the height of the coils on the MagFloor is not exactly the same, there is an additional difficulty in maintaining a constant levitation gap. To resolve this, the coil height is interpolated at the location of the mover and added to the reference z_{ref} position. This interpolation is done using the x, y reference location of the mover and the (c_x^g, c_y^g, c_z^g) coil locations of the four coils surrounding the center point of the mover. The 2-D interpolation is done on a non-uniform grid since the coil spacing is assumed non-uniform. This interpolation strategy is illustrated in figure 4.6.

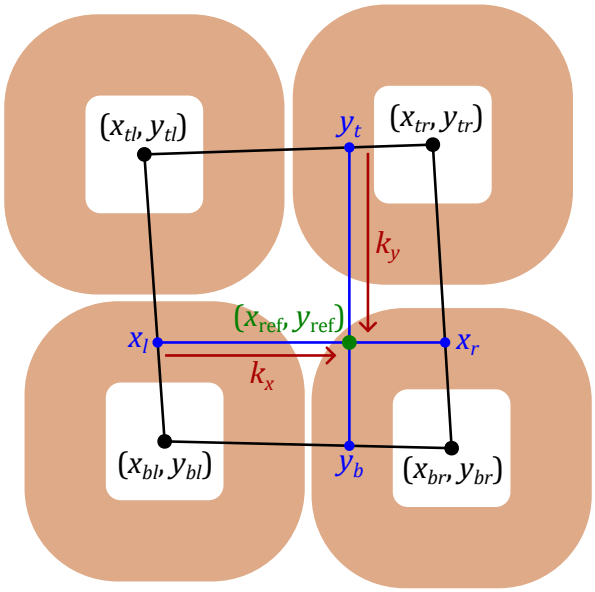

Figure 4.6: Interpolation between four coils around the center of the mover. The coil misalignment is exaggerated for illustrative purposes.

First, intermediate y values are found between the top two coils and bottom two coils by interpolating in x

$$y_t = y_{tl} + \frac{x_{\text{ref}} - x_{tl}}{x_{tr} - x_{tl}}(y_{tr} - y_{tl}), \tag{4.11a}$$

$$y_b = y_{bl} + \frac{x_{\text{ref}} - x_{bl}}{x_{br} - x_{bl}}(y_{br} - y_{bl}), \tag{4.11b}$$

where x_{tl}, x_{tr}, x_{bl}, and x_{br} are the x locations of the top-left, top-right, bottom-left, and bottom-right coils around the center of the mover when viewed from the top. An interpolation coefficient is then found along y between these two intermediate values

$$k_y = \frac{y_t - y_{\text{ref}}}{y_t - t_b}. \tag{4.12}$$

Using a similar process in x, intermediate x values are found between the left two coils and right two coils by interpolating in y

$$x_l = x_{bl} + \frac{y_{\text{ref}} - y_{bl}}{y_{tl} - y_{bl}}(x_{tl} - x_{bl}), \tag{4.13a}$$

$$x_r = x_{br} + \frac{y_{\text{ref}} - y_{br}}{y_{tr} - y_{br}}(x_{tr} - x_{br}), \tag{4.13b}$$

where x_l and x_r are the left and right interpolated x values. An interpolation coefficient in x is then found between these two values,

$$k_x = \frac{x_{\text{ref}} - x_l}{x_r - x_l}. \tag{4.14}$$

Using these two interpolation coefficients, a z position is interpolated between the four coils. The contribution of each coil is given by

$$k_{tl} = (1 - k_x)(1 - k_y)z_{tl}, \tag{4.15a}$$

$$k_{tr} = k_x(1 - k_y)z_{tr}, \tag{4.15b}$$

$$k_{bl} = (1 - k_x)k_y z_{bl}, \tag{4.15c}$$

$$\text{and} \quad k_{br} = k_x k_y z_{br}. \tag{4.15d}$$

The interpolated z position is then the sum of these four contributions

$$z_{\text{coil}} = k_{tl} + k_{tr} + k_{bl} + k_{br}. \tag{4.16}$$

With this method, the final target $z_{\text{ref,f}} = z_{\text{ref}} + z_{\text{coil}}$ varies with the location of the mover and is not constant within a given trajectory. In this thesis, plots of experimental results on the MagFloor show the original unmodified z_{ref} and a corrected measured z position using $z_{\text{act,c}} = z_{\text{act}} - z_{\text{coil}}$. This is the estimated levitation gap.

Figure 4.7 shows a x-ramp motion of 500 mm/s on the MagFloor. The middle plot shows the modified reference $z_{\text{ref,f}}$ sent to the controller using the interpolation strategy and the measured z_{act} from the Vicon camera system. Since the controller uses the measured coil heights at each location to compute the force and torque, the target levitation gap is approximately constant. The lower plot shows the original reference height z_{ref} and a corrected measurement $z_{\text{act,c}}$ found by subtracting the estimated coil height from the Vicon reading. This is approximately the levitation gap and this is what is plotted for the z axis in later sections of this thesis.

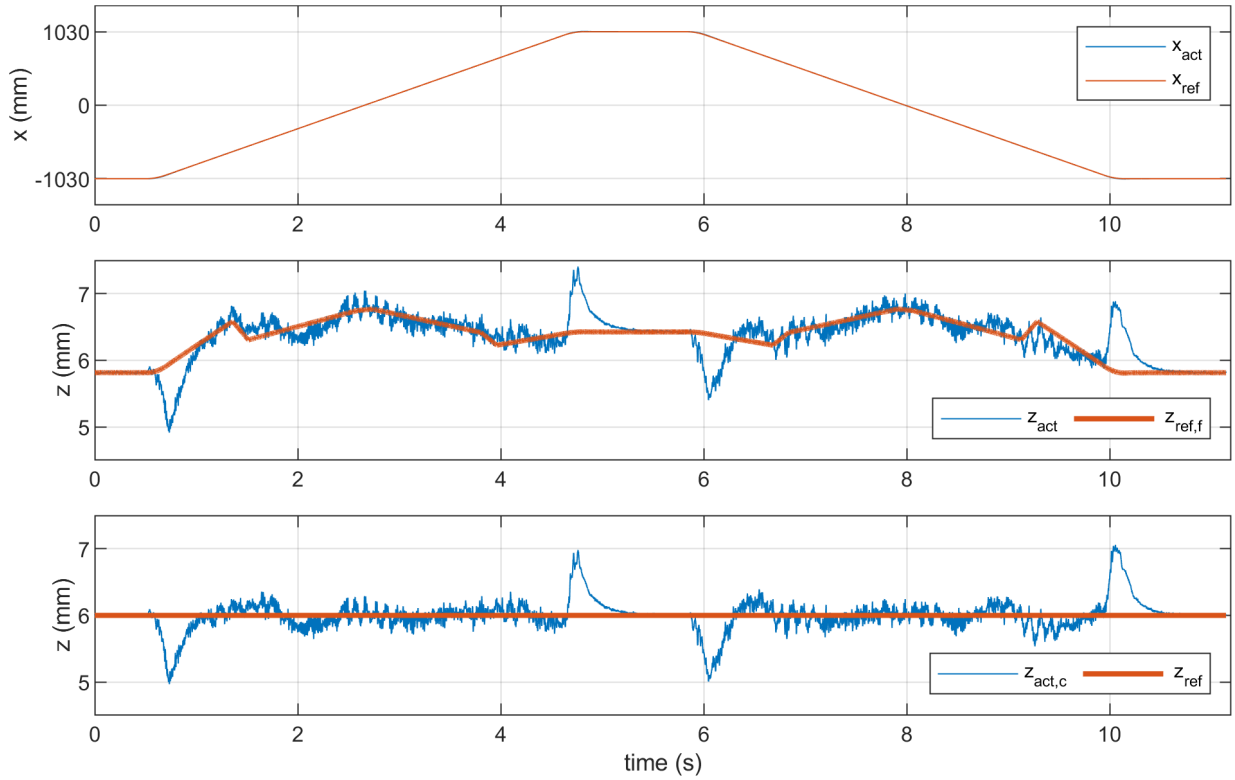

Figure 4.7: X-ramp on the MagFloor showing the z reference adjustment.

Chapter 5

Measurement Systems

Two separate measurement systems are utilized in this thesis to provide position feedback for the closed-loop control of the system. The first measurement system is a camera-based motion tracking system, which was tested on both the smaller prototype magnetic levitation system and the larger MagFloor in the RoboHub. The second measurement system utilizes eight laser displacement sensors positioned to measure against three flat surfaces on the mover. The laser displacement sensors were only tested on the prototype maglev system since they have a small measurement range. Both measurement systems can provide the 6-D position of the mover required for control.

5.1 Camera Motion Tracking System

The camera motion tracking system projects infrared light onto the work area, which is reflected by spherical markers placed on the mover and then received to produce a gray-scale IR image. This approach enables much simpler image processing as with proper calibration and settings, only the circles from the reflective markers will appear in the image, for which centroids can be efficiently fit to locate the markers in the 2-D image. By using multiple stationary cameras, these 2-D locations of each marker can be extended into locations in 3-D space. If there are at least three markers on an object, where the relative distances between the markers are known and rigid, then this set of 3-D points of each marker can be used to determine the 6-D position and orientation of the object. This corresponds to three translations (x, y, z) and three elementary rotations about the coordinate axes, roll, pitch, and yaw, denoted with α, β, and γ, respectively. A motion tracking system from Vicon was utilized in this system, which provides software to perform image processing and object tracking.

The reflective marker layout on the mover is shown in figure 5.1a, and the object detected by the Vicon Tracker software is shown in figure 5.1b. The mover has six markers mounted on its top surface: three markers in the center which form a 90° angle, and three markers on standoff towards the corners of the mover. The three markers at the center

aid in aligning the mover's coordinate system in the Vicon Tracker software, which is then translated to the center bottom of the magnet array. The three markers at the corners help to produce a more precise measurement of the rotations of the mover since they are farther apart, and the standoffs of varying heights also help to improve the measurement. Although only three markers are required to determine the position of the object, additional markers help to reduce measurement noise and enable measurements in the case a few markers are obstructed. The resulting 6-D position of the object can be obtained via a UDP data stream for low-latency communication. This data stream is connected to the PLC and read via a TwinCAT project.

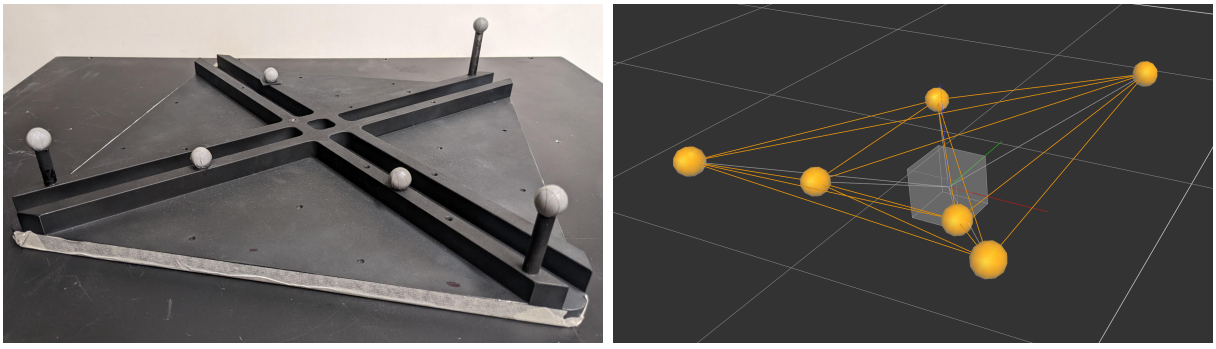

(a) Marker layout for cameras **(b)** Mover object in Vicon software

Figure 5.1: Mover setup for the camera system.

The camera system can accommodate long-stroke applications, such as on the MagFloor, due to the wide field of view and sufficient resolution. Many cameras can also be added with overlapping fields of view, such that with automatic camera switching, a nearly unlimited motion range can be achieved. Since the cameras utilize the IR spectrum to reduce noise and distractions, very little image processing is required. This enables the motion tracking to operate at high frequency, and in this experiment setup, they are set to operate at 1000 fps. To achieve this high speed, the cameras are set to "High Speed Mode" in the Vicon tracker software, which uses subsampling on the image frame to reduce the processing and data rate required, while still maintaining the full field of view. Refer to table 5.1 for more specifications of the cameras used in this system.

Before the camera system can be used to track the mover, the cameras must be calibrated so that they know their relative locations with respect to each other, and a coordinate system must be established. The camera calibration is done using the Vicon Tracker software while capturing a wand with LED lights of known spacing which is waved around the workspace of the cameras.

Table 5.1: Vicon V5 Camera Specifications.

Component	Specification
Resolution (pixels)	2432 H x 2048 V
Lens focal length	8.5 mm
Field of view (H x V)°	63.5 x 55.1
Strobe	850 nm (IR)
Set frame rate	1000 fps

To establish the **global** coordinate system of the cameras, four points are used with reflective markers mounted on blocks which slide into the core of the coils on the stator. Three of the points are used to establish the orientation of the coordinate system, where a line drawn between the first two is the direction of the x-axis, and the third point is used to establish the xy plane (the three markers don't need to form a 90° angle). After the orientation of the coordinate system is established, a fourth marker is used to locate the origin of the coordinate system, which is then translated to be in the center of the coil array and at the top of the coil winding. Refer to figure 5.2 for an illustration of establishing the camera coordinate system.

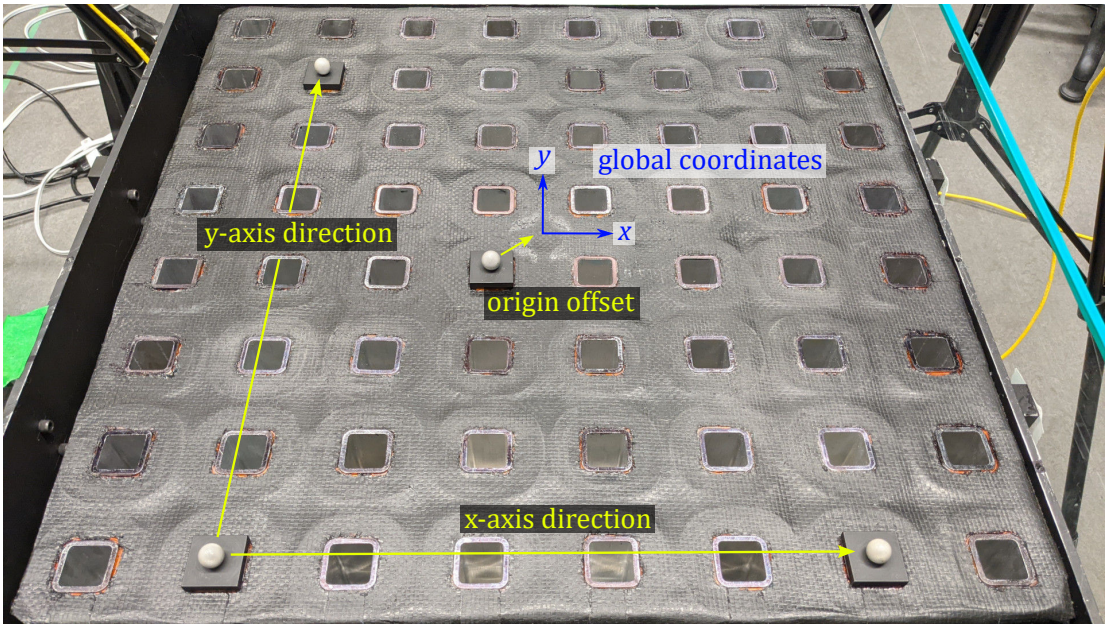

Figure 5.2: Configuring camera coordinate system with four markers.

5.2 Laser Displacement Sensors

For higher precision measurement feedback, a set of eight laser displacement sensors were mounted to the stator. Since each of these sensors only return a single linear displacement of the laser spot, at least six displacement sensors are required to determine the six degrees of freedom movement. Using eight displacement sensors increases robustness in case one or two sensors are obstructed and reduces measurement noise when all eight are utilized. The sensor heads were placed with four above the mover and two on two sides, thus detecting three surfaces to determine the 6-D position. A custom frame of T-slotted aluminum was designed and fabricated to support the sensor heads, as shown in the CAD render in figure 5.3. Since the measurement range of the laser sensors is small, this frame was designed such that it could be moved around the stator between experiments, while maintaining the same relative distances between the eight sensor heads. The majority of the weight of the sensor frame is supported by an adjustable arm, and additional stability is provided by three aluminum supports mounted on the side covers of the stator.

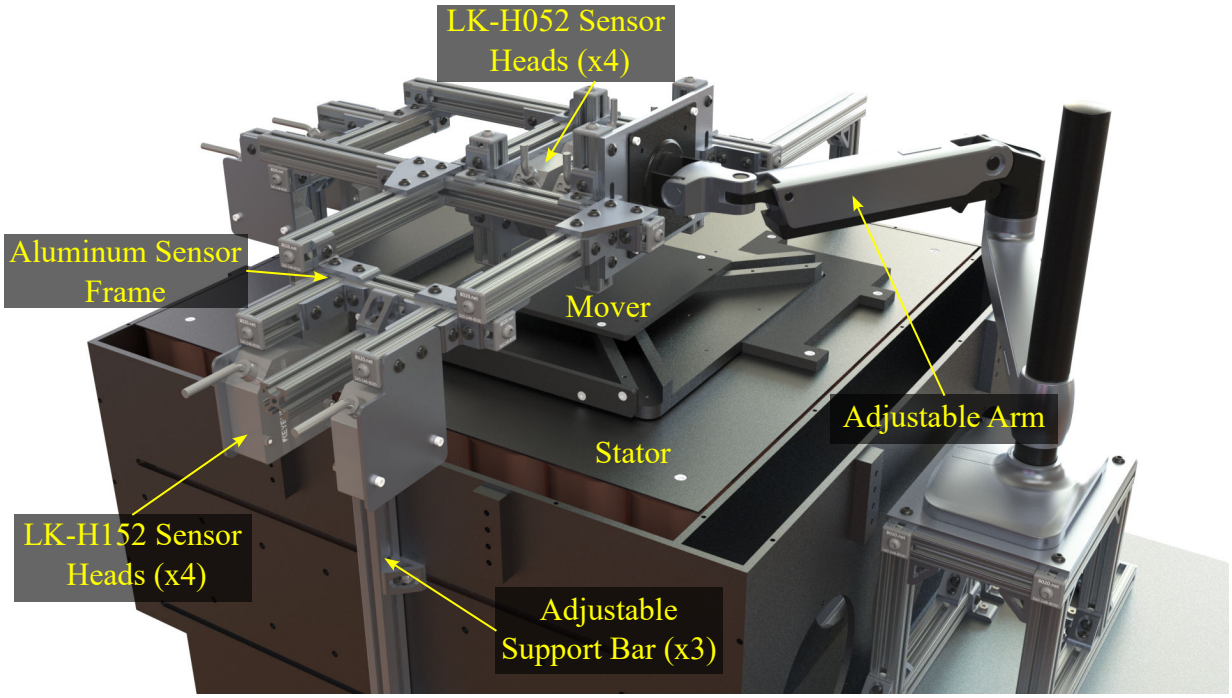

Figure 5.3: Render of laser displacement sensor setup with aluminum frame.

The LK-H052 sensors mounted on top have a reference distance of 50 mm with a range of ±10 mm, and the LK-H152 heads on the sides have a reference distance of 150 mm with a range of ±40 mm. As shown in figure 5.4a, the sensors on top are placed close together with about 12 mm between them to allow room for the mounting fasteners. They are about 50 mm above the mover when at a levitation height of 6 mm to be close to the reference distance. Keeping the top sensor heads close together maximizes the horizontal xy movement range as the lasers do not go off the top plate.

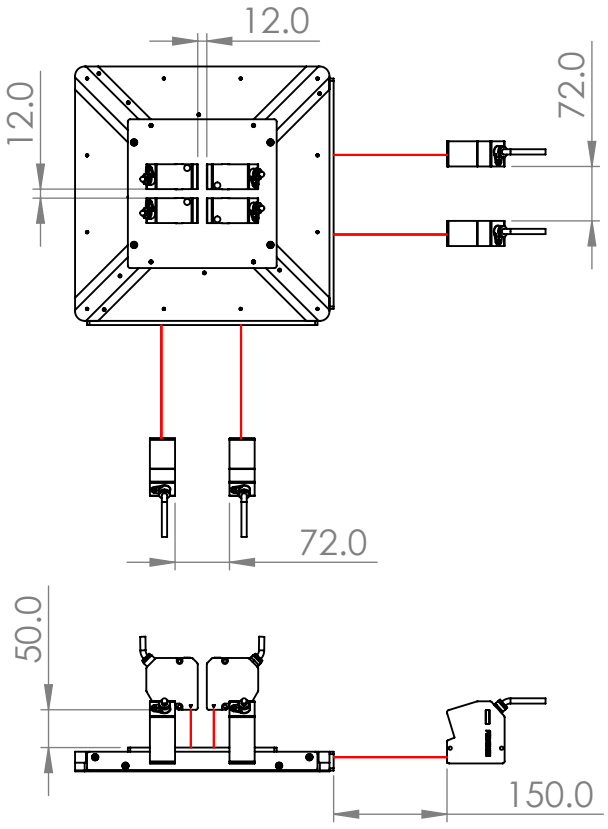

(a) Sensor placement dimensions

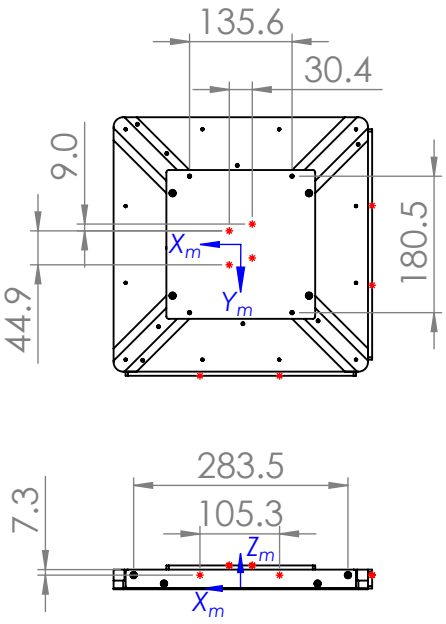

(b) Laser dot dimensions

Figure 5.4: Laser sensor placement with respect to the mover.

The side sensors are placed about 150 mm away from the mover at the reference location and about 72 mm apart. This means that the laser dots from the side sensors are about 105 mm apart, as shown in figure 5.4b, and the greater separation distance helps to improve the γ rotation measurement as these sensors are less precise than the top sensors. The

side sensors are positioned so that the laser dots will pass above the lower mounting screws of the side plates, thus ensuring good readings while the mover moves in its full $\pm 40\,\text{mm}$ range in x, y. A yaw γ rotation of about $\pm 20^\circ$ can be detected. Note that the mover is $336.6\,\text{mm} \times 336.6\,\text{mm} \times 26.0\,\text{mm}$ and the flat plates are $5.5\,\text{mm}$ thick.

Since the laser emitters are not in the center of the sensor heads, the laser dots from the top sensors do not form a rectangle, as shown in figure 5.4b. The top dots are about $30\,\text{mm}$ apart in the x direction, but about $45\,\text{mm}$ apart in the y direction. This makes the rotation about the x axis, α, easier to detect than the rotation about y, β. For the full $\pm 40\,\text{mm}$ range in x, y, the top laser dots will remain on the top flat plate and stay between the screw holes. The mover's coordinate system is also shown in figure 5.4b at the bottom center of the magnet array.

The measurement principle of the laser displacement sensors is based on triangulation. The laser first goes through a set of lenses which tightly focus the laser spot and keep the spot width consistent throughout the measurement range. The laser then shines on the measurement surface and diffusely reflects back in all directions. Another set of lenses and a CMOS sensor receive the reflected light at an angle. This angle depends on the measurement distance and determines where the laser will be received on the CMOS sensor. As such, this angle can be used to determine the distance to the measurement surface. See figure 5.5 for an illustration of this triangulation principle adapted from the catalogue of the sensor series [71].

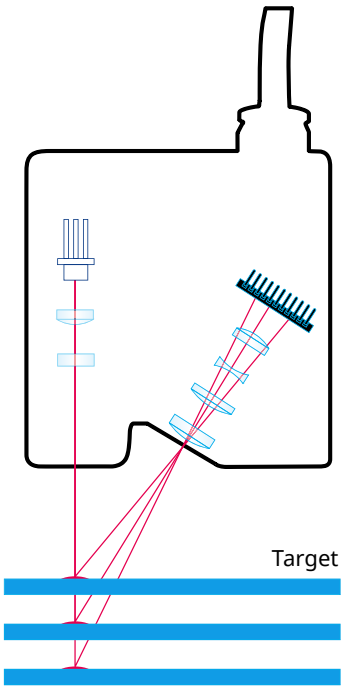

Figure 5.5: Principle of laser triangulation [71].

In order for the laser to reflect back into the receiver during mover motion and while the angle of the measurement surface changes, the measurement surface must be a diffusely reflective and opaque surface. To satisfy this requirement, flat plates of Delrin plastic were added to three sides of the mover and painted a matte black, as shown in figure 5.6. The surfaces of the plates were sanded with a fine 180-grit sandpaper before painting to achieve the matte finish. Delrin plastic was chosen as it is lightweight and easy to machine. The black paint was not too dark for the sensors to detect.

Two models of the laser sensor heads were used: four higher precision heads above the mover to detect the top surface and two longer range sensor heads on two sides, for

a total of eight sensor heads. The higher precision sensors are better on the top as the range of movement in the z-axis is small, and the system is more sensitive to measurement error in the z-axis. All laser displacement sensors were from Keyence, and their major specifications are listed in table 5.2. Measurements are sampled at a high 50 kHz and are averaged internally in the laser sensor controller before being sent to the PLC. However, measurements can only be sent from the laser sensor controller to the PLC at a maximum rate of 500 Hz using Ethernet/IP communication. Sampling at a higher frequency and using an averaging filter helps to reduce the measurement noise.

The LK-H052 sensor heads have a resolution of 10 nm and the LK-H152 have a resolution of 100 nm, however, their repeatabilities are listed as 25 nm and 250 nm, respectively. During experiments, it was found that the amplitude of the measurement noise is much higher (5–20x) than the repeatability listed in the datasheet of the sensors. This could be because the averaging filter was set to 16384 samples for the data sheet repeatability, which is 256 times greater than the 64 samples set in this experiment to reduce the measurement delay. Other factors such as vibrations in the building may also be contributing to the measurement noise.

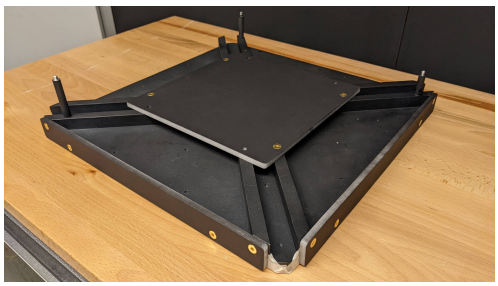

Figure 5.6: Mover with flat plates for the laser sensors.

Table 5.2: Laser Displacement Sensor Specifications.

Component	Heads 1-4	Heads 5-8
Keyence Model	LK-H052	LK-H152
Reference distance (mm)	50	150
Measuring range (mm)	±10	±40
Laser class (JIS C6802)	Class 2	
Laser wavelength (nm)	655	
Laser output power (mW)	0.95	
Spot diameter (µm)	50	120
Linearity	±0.02% of F.S.	
Repeatability (µm)	0.025	0.25
Set sampling cycle (µs)	20	
Set averaging measurements	64	
Communication cycle (µs)	2000	

Figure 5.7 shows an overview of the equipment setup using the laser displacement sensors for measurement feedback. During the initial setup, a removable L-bar is aligned with three calibration blocks and the mover is then aligned to the L-bar. This places the mover in a known location, from which the location of the aluminum laser sensor frame can be found using the measurement readings of the sensors, which are assumed to have fixed relative spacing. The L-bar is removed before starting a levitation. This process is described in more detail in section 5.4.

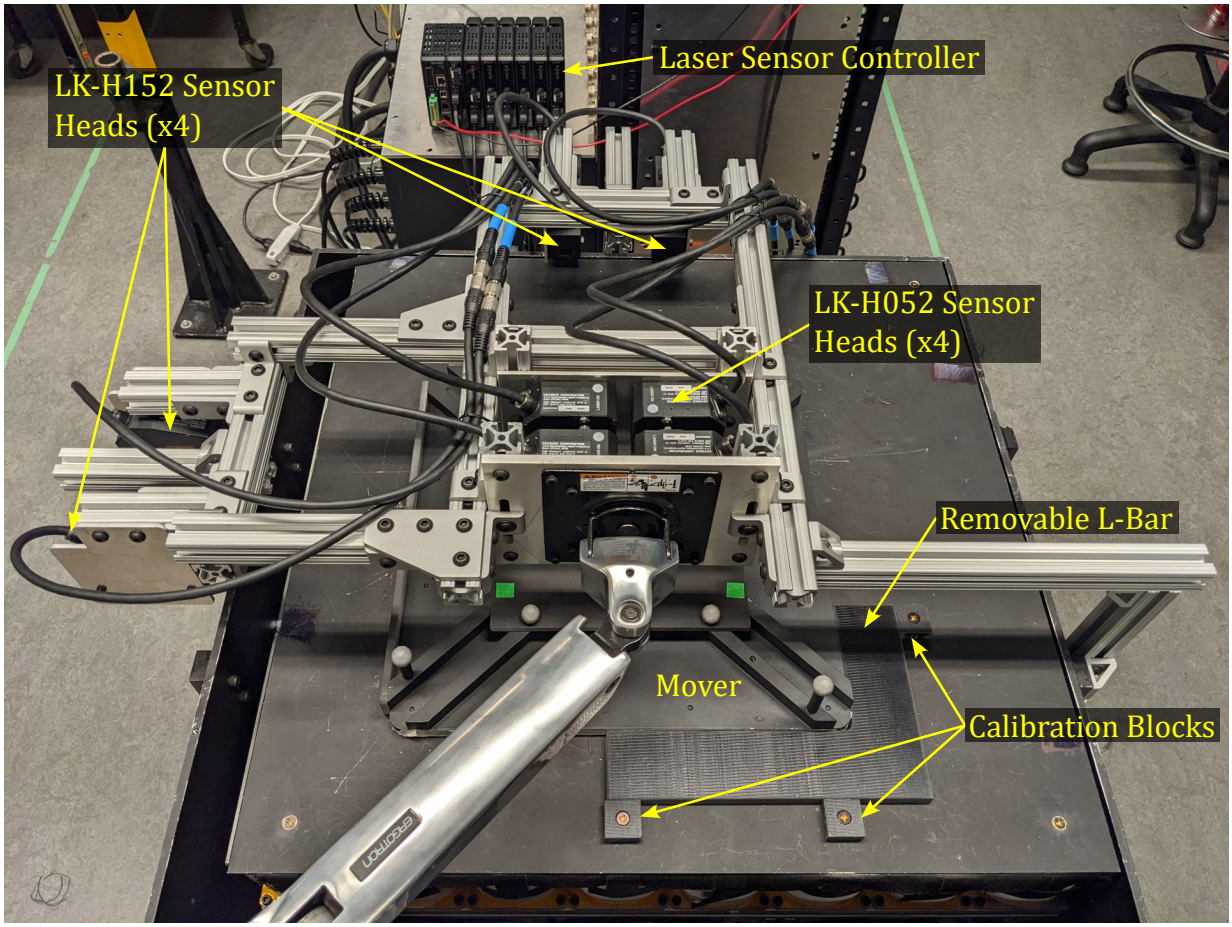

Figure 5.7: Setup of the laser displacement sensors.

5.3 Laser Displacements to 6-D Position

Since the eight laser displacement sensors only return the raw displacements between the sensor heads and the sides of the mover, some extra calculations are required to determine the 6-D position and orientation of the mover. To find the 6-D position of the mover,

1. the displacement measurements are converted to 3-D (x, y, z) points on the surface of the mover,
2. these points are used to determine the normal vectors for each of the three side planes of the mover,
3. the normal vectors and points are used to define the equations of the planes,
4. the intersection of the three planes is taken to find the point at the corner of the mover,
5. the three normal vectors are used to find the XYZ Euler rotation angles, α, β, and γ,
6. the point at the corner of the mover is translated along the determined axes to the bottom center of the magnet array,
7. and finally, the obtained position and orientation of the mover is converted from **frame** to **global** coordinates.

5.3.1 Converting Displacements to 3-D Points

The first step in utilizing the laser displacement sensor output is to convert the readings into 3-D points in the **frame** coordinate system. The laser heads 1–4 are oriented in the $-z$ direction, heads 5 and 6 are oriented in the $+x$ direction, and heads 7 and 8 are oriented in the $-y$ direction, as shown in figure 5.8. Heads 1–4 have a reference distance of 50 mm with a range of ± 10 mm and heads 5-8 have a reference distance of 150 mm with a range of ± 40 mm. Note that a positive laser displacement corresponds to a movement closer to the sensor head, and a negative laser displacement to a movement away. Let $\vec{P}_h^f = (x_h, y_h, z_h)$ denote the point on the laser head from which the laser emits in **frame** coordinates and h

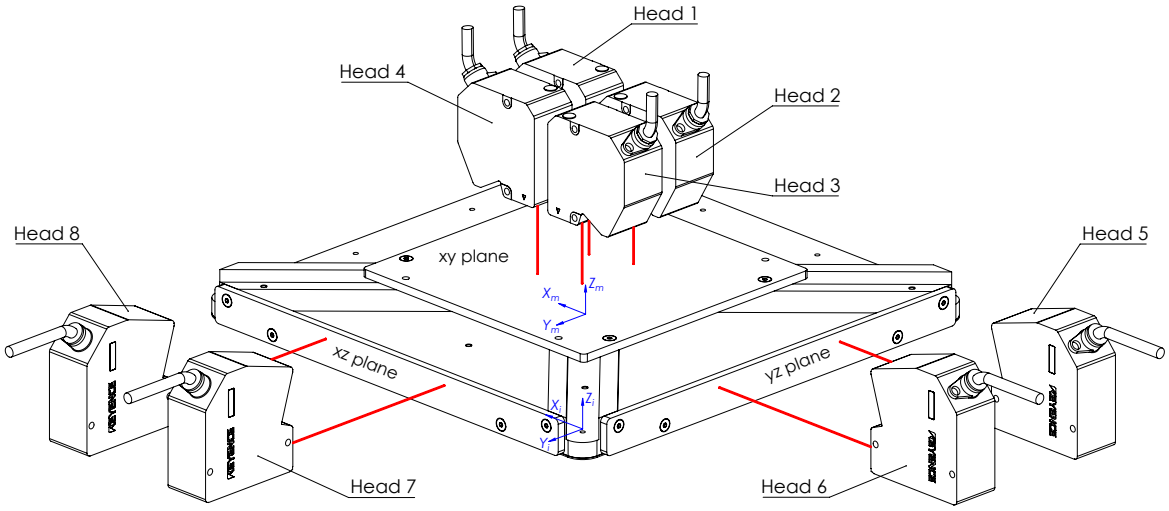

Figure 5.8: Arrangement of the eight laser displacement sensor heads.

denote the laser displacement reading. Then, for heads 1–4, the point of intersection with the mover $\vec{P}^f = (x_p, y_p, z_p)$ in mm is given by

$$\vec{P}^f = \begin{bmatrix} x_p \\ y_p \\ z_p \end{bmatrix} = \begin{bmatrix} x_h \\ y_h \\ z_h - 50 + h \end{bmatrix}, \tag{5.1}$$

for heads 5 and 6,

$$\vec{P}^f = \begin{bmatrix} x_p \\ y_p \\ z_p \end{bmatrix} = \begin{bmatrix} x_h + 150 - h \\ y_h \\ z_h \end{bmatrix}, \tag{5.2}$$

and finally, for heads 7 and 8,

$$\vec{P}^f = \begin{bmatrix} x_p \\ y_p \\ z_p \end{bmatrix} = \begin{bmatrix} x_h \\ y_h - 150 + h \\ z_h \end{bmatrix}. \tag{5.3}$$

5.3.2 Finding Equations of the Three Planes

A plane in 3-D space is defined by the equation

$$ax + by + cz = d, \tag{5.4}$$

where at least one of the coefficients a, b, or c must be non-zero. The equation of a plane can be determined by a point on the plane and the normal vector to the plane. Let $\vec{P} = (x, y, z)$ be any point on the plane, $\vec{P}_0 = (x_0, y_0, z_0)$ be a known point on the plane, and $\vec{n} = (a, b, c)$ be the normal vector to the plane, then $\overrightarrow{P_0P}$ is a vector on the plane, which by definition, must be perpendicular to the normal of the plane. Thus, by taking the dot product of $\overrightarrow{P_0P}$ with $\vec{n}$, the equation of a plane is obtained [72]

$$\begin{aligned}
\overrightarrow{P_0P} \cdot \vec{n} &= (x - x_0, y - y_0, z - z_0) \cdot (a, b, c) \\
&= a(x - x_0) + b(y - y_0) + c(z - z_0) \\
&= ax + by + cz - (ax_0 + by_0 + cz_0) \\
&= 0.
\end{aligned}$$

Therefore, the equation of a plane can also be written as

$$ax + by + cz = (ax_0 + by_0 + cz_0) = d, \tag{5.5}$$

where $\vec{n} = (a, b, c)$ is the normal vector to the plane and $\vec{P}_0 = (x_0, y_0, z_0)$ is a point on the plane.

For the top xy plane of the mover, there are four laser displacement readings, and thus four points on the plane can be obtained. Note that three points that do not lie on the same line are sufficient to fully define a plane, as vectors can be drawn between them, and their cross product can find the normal to the plane. With four points, a *best fit* plane can be obtained using the singular value decomposition (SVD).

The SVD of an $m \times n$ real matrix $\mathbf{A}$ returns a factorization of the form $\mathbf{A} = \mathbf{U}\mathbf{\Sigma}\mathbf{V}^T$, where $\mathbf{U}$ is an $m \times m$ orthogonal matrix, $\mathbf{\Sigma}$ is an $m \times n$ rectangular diagonal matrix, and $\mathbf{V}$ is an $n \times n$ orthogonal matrix. The diagonal entries $\sigma_i = \Sigma_{ii}$ of $\mathbf{\Sigma}$ are the singular values of $\mathbf{A}$. The non-zero singular values correspond to the square roots of the non-zero eigenvalues of $\mathbf{A}^T\mathbf{A}$ and $\mathbf{A}\mathbf{A}^T$. The columns of $\mathbf{U}$ are the left-singular vectors of $\mathbf{A}$, are the eigenvectors of $\mathbf{A}\mathbf{A}^T$, and form an orthonormal basis for $\mathbb{R}^m$. The columns of $\mathbf{V}$ are the right-singular vectors of $\mathbf{A}$, are the eigenvectors of $\mathbf{A}^T\mathbf{A}$, and form an orthonormal basis for $\mathbb{R}^n$. [72]

When taking the SVD of a $3 \times n$ matrix $\mathbf{A} = \mathbf{U}\mathbf{\Sigma}\mathbf{V}^T$, whose columns represent n 3-D points of zero-mean lying on a plane, the columns of $\mathbf{U}$ are the left-singular vectors and are the direction vectors of the semiaxis of a 3-dimensional ellipsoid fit to the data. When the singular values are arranged in descending order, the first two columns of $\mathbf{U}$ will form direction vectors that lie on the plane, while the third column of $\mathbf{U}$ will be a unit vector normal to the plane. It is important that the set of points have zero-mean (centred about the origin) for this to work, so the mean of the set of points should be found and then subtracted from all the points. By using this method with the four points on the top xy plane of the mover, the right-most column of the left-singular vectors will be a unit normal vector to the plane, $\hat{n}_{xy}$. The sign of this vector is checked to ensure it aligns with the z-axis as shown in figure 5.8, otherwise, the sign of the vector is flipped.

After the normal vector to the xy plane is found, finding the normals to the other two planes can be done using the cross product. A vector on the yz plane can be created using the points on the mover from sensor heads 5 and 6, $\overrightarrow{P_{56}}^f = \overrightarrow{P_{m6}}^f - \overrightarrow{P_{m5}}^f$. By taking the cross product with the xy normal found earlier and normalizing, the unit normal to the yz plane is found

$$\hat{n}_{yz} = \frac{\overrightarrow{P_{56}}^f \times \hat{n}_{xy}}{\left|\overrightarrow{P_{56}}^f \times \hat{n}_{xy}\right|}. \tag{5.6}$$

Finally, the normal to the third plane can be found by simply taking the cross product of the two unit vectors already found

$$\hat{n}_{xz} = \hat{n}_{xy} \times \hat{n}_{yz}. \tag{5.7}$$

To make full use of the eight sensor heads,

1. the yz normal $\hat{n}_{yz1}$ is first found using the cross product of a vector between points 5 and 6, $\overrightarrow{P_{56}}^f$, and the xy normal $\hat{n}_{xy}$ as shown in equation (5.6),
2. the xz normal $\hat{n}_{xz1}$ is then found using the cross product of the xy normal $\hat{n}_{xy}$ and a vector between points 7 and 8, $\overrightarrow{P_{78}}^f$,
3. the yz normal $\hat{n}_{yz2}$ is then found again using the cross product of $\hat{n}_{xz1}$ and $\hat{n}_{xy}$,
4. the average of the two yz unit normals $\hat{n}_{yz1}$ and $\hat{n}_{yz2}$ is taken and normalized to a unit vector $\hat{n}_{yz}$,
5. and finally the xz normal $\hat{n}_{xz}$ is found again using the cross product of $\hat{n}_{xy}$ and $\hat{n}_{yz}$ as in equation (5.7).

By following this procedure, the best-fit normals to the three planes are found utilizing all 8 sensor heads, and the three normal vectors are guaranteed to be an orthonormal set. They will also follow the right-hand rule and be oriented as shown in figure 5.8.

To create the equations of the three planes, a point on each plane is also needed. The mean of the four points from heads 1–4 is used as the point on the xy plane, $\overrightarrow{P_{xy}}^f$, the mean of the points from heads 5 and 6 is used as the point on the yz plane, $\overrightarrow{P_{yz}}^f$, and the mean from the points from heads 7 and 8 is used as the point on the xz plane, $\overrightarrow{P_{xz}}^f$.

A system of equations for the three planes is then formed using the normals and points and the dot product to create equations of the form of equation (5.5),

$$\begin{bmatrix} \hat{n}_{yz}^T \\ \hat{n}_{xz}^T \\ \hat{n}_{xy}^T \end{bmatrix} \begin{bmatrix} x \\ y \\ z \end{bmatrix} = \begin{bmatrix} \hat{n}_{yz} \cdot \overrightarrow{P_{yz}}^f \\ \hat{n}_{xz} \cdot \overrightarrow{P_{xz}}^f \\ \hat{n}_{xy} \cdot \overrightarrow{P_{xy}}^f \end{bmatrix}. \tag{5.8}$$

Solving this system of equations will produce a point $\vec{P}_i^f = (x, y, z)$ in **frame** coordinates at the intersection of the three planes, which is the corner of the mover.

Note that only 6 laser sensor heads are actually needed with this approach to find the equations of the three planes. More specifically, three measurements on the top xy plane of the mover are needed to find the normal of this plane, two measurements on one of the side planes can find its normal using the cross product, and then one last measurement on the other side plane is needed for a point on that plane. Sensor obstructions are accounted for in the code such that the system is robust to obstructions of one or two of the laser sensor heads, provided the requirements described are met. Using all 8 sensor readings helps to reduce measurement noise and improve performance.

5.3.3 Finding the 6-D Position in Frame Coordinates

Once the normal vectors to the three planes are found, these can be assembled to form a rotation matrix $\mathbf{R}_m^f$ which can be used to convert a vector in **mover** coordinates to **frame** coordinates. Assuming the normal vectors are unit vectors forming an orthonormal set, and that they follow the right-hand rule, this rotation matrix is given by:

$$\mathbf{R}_m^f = \begin{bmatrix} \hat{n}_{yz} & \hat{n}_{xz} & \hat{n}_{xy} \end{bmatrix}. \tag{5.9}$$

The XYZ Euler angles describing the rotations can be found from the elements of the

total rotation matrix, $\mathbf{R} = \mathbf{R}_x\mathbf{R}_y\mathbf{R}_z$,

$$\begin{aligned}\alpha &= \arctan\left(\frac{-R_{23}}{R_{33}}\right),\\ \beta &= \arctan\left(\frac{R_{13}}{\sqrt{1-{R_{13}}^2}}\right),\\ \gamma &= \arctan\left(\frac{-R_{12}}{R_{11}}\right).\end{aligned} \tag{5.10}$$

At this point, the rotation of the mover, $\mathbf{R}_m^f$, and the position of the corner of the mover at the intersection of the three planes, $\vec{P}_i^f$, have been found. However, the point of the bottom-center of the magnet array is desired. This can be found using the transformation,

$$\vec{m}^f = \vec{P}_i^f + \mathbf{R}_m^f\vec{T}_i, \tag{5.11}$$

where $\vec{T}_i$ is a vector from the corner of the mover to its bottom-center, in the mover coordinate system, and $\vec{m}^f = \begin{bmatrix}x & y & z\end{bmatrix}^T$ is the position of the mover in the **frame** coordinate system. The translation vector is given by $\vec{T}_i = \begin{bmatrix}w_m & -w_m & -h_m\end{bmatrix}^T$, where w_m is the distance from the side surface to the center of the mover, and h_m is the distance from the top xy surface to the bottom of the magnet array.

5.3.4 Converting to Global Coordinates

At this point, the 6-D position of the mover has been found in the sensor **frame** coordinate system. However, the laser sensor frame may not be aligned to the **global** coordinate system at the center of the coil array. As such, this 6-D position must be converted to the **global** coordinates before it can be used in the control system. Let the matrix $\mathbf{R}_m^f$ describe the total rotation of the **mover** with respect to the **frame** coordinate system and the matrix $\mathbf{R}_f^g$ describe the rotation of the **frame** coordinate system with respect to the **global** coordinate system. Then, the rotation matrix describing the rotation of the mover with respect to the **global** coordinates is

$$\mathbf{R}_m^g = \mathbf{R}_f^g\mathbf{R}_m^f. \tag{5.12}$$

The Euler angles describing the rotation of the mover with respect to the **global** coordinates, α_m^g, β_m^g, and γ_m^g, can then be found using arctan of the elements of $\mathbf{R}_m^g$ as shown in equation (5.10).

The position of the mover in **global** coordinates, $\vec{m}^g$, can be found using

$$\vec{m}^g = \mathbf{R}_f^g \vec{m}^f + \vec{f}^g \tag{5.13}$$

where $\vec{m}^f$ is the position of the mover in **frame** coordinates and $\vec{f}^g$ is the location of the frame coordinate system in **global** coordinates. It is the position in **global** coordinates, $\vec{m}^g$, that is sent to the closed-loop controller.

5.4 Calibrating the Laser Measurement System

The laser measurement system must be calibrated with a reference to ensure it is giving an accurate position reading. In the calibration procedure, it is assumed that the relative distances between the eight laser sensor heads are constant and known with less than 1 mm error. However, due to the design of the laser sensor apparatus, the sensor frame can be positioned at various locations with respect to the coil array, with the eight sensors moving together. As such, the 6-D position of the sensor frame with respect to the **global** coordinates, is an unknown that must be solved for in a calibration procedure. This position of the frame is needed in equations (5.12) and (5.13) to solve for the position of the mover in **global** coordinates.

To calibrate for the position of the frame, the mover is placed in a known reference location. In this location, the rotation of the mover in **global** coordinates, $\mathbf{R}_m^g$, is known, and the rotation of the mover in **frame** coordinates, $\mathbf{R}_m^f$, can be found using the sensor readings and the procedure described in section 5.3. Then, the rotation of the frame with respect to the global coordinate system is given by

$$\mathbf{R}_f^g = \mathbf{R}_m^g \mathbf{R}_m^{f\,T}. \tag{5.14}$$

The position of the frame in **global** coordinates can then be found using the equation

$$\vec{f}^g = \vec{m}^g - \mathbf{R}_f^g \vec{m}^f. \tag{5.15}$$

Figure 5.9 shows how the mover is positioned in a known location using reference blocks on the coil array during the laser calibration. The L-shaped block is removed after the calibration is completed, and since it is slightly wider than 40 mm, the remaining three square blocks are outside of the movement range the sensors can measure and can stay mounted during levitation. The position of the mover when aligned with the reference blocks was measured using the Vicon camera system to ensure consistency between the measurements of the two systems.

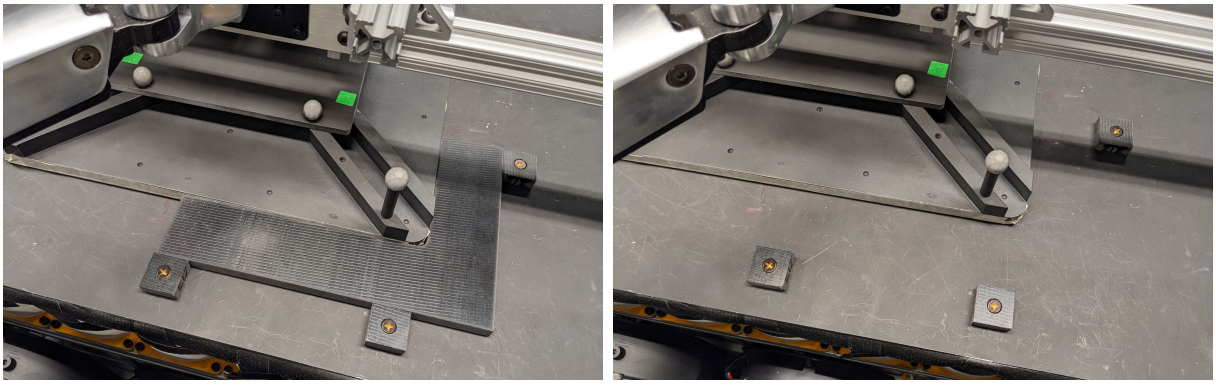

(a) With L-bar, before levitation **(b)** Without L-bar, after calibration

Figure 5.9: Laser sensor calibration with small blocks and an L-bar.

5.4.1 Calibrating for Partial Obstructions

Since eight laser displacement sensors are utilized to find the 6-D position, but only six sensors are required, the resulting measurement is a "best fit" to the raw data. However, if one or two sensors are obstructed, the measurement reading will slightly jump due to errors, such as imperfect sensor positioning, which cause the new "best fit" to slightly change. To significantly reduce this jump in the reading, offsets can be added to all eight linear displacement measurements which simply move their reading to this "best fit" during the sensor calibration. This should not change the estimated 6-D measurement when all eight sensors are utilized but will reduce any jump in the measurement if a sensor is obstructed.

To find the offsets to add to the displacement readings, the 6-D position of the mover in **frame** coordinates is first estimated using the displacement readings and the procedure described in section 5.3. Then, the reverse process is done by using this 6-D position to estimate what should be the eight linear displacement readings. The displacement offsets are then found by simply taking the difference between the estimated displacement readings for this position and the actual displacement readings returned from the sensors. This process is only done once during the calibration procedure to find the frame position described earlier, and this one set of offsets is then stored and added to all displacement readings during levitation. Imperatively, none of the laser sensors can be obstructed during the calibration procedure for this to work properly.

The process to find the eight displacement readings from the 6-D position is simply the reverse of the process described in section 5.3. The estimated displacements are found by

1. using the known rotation angles of the mover with respect to the sensor frame to rotate the normal vectors of the side planes of the mover,
2. using the 6-D position of the mover to transform known points on the side planes of the mover,
3. defining equations of the side planes using the points and normal vectors,
4. finding the intersection of the lines from the sensors heads to the planes on the mover,
5. and using the points of intersection to find the laser displacement readings.

5.5 Measurement Noise

For each measurement system, the mover was placed resting on the stator without levitation, and the stationary measurement noise was recorded over a 3 min time period. The resulting measurement noise in each of the six axes is shown in figures 5.10 to 5.12 for the laser sensors on the 64 coils and the cameras on both the 64 coils and the MagFloor. The standard deviation of the measurement noise in each axis is shown in table 5.3, along with 3σ, for which $\pm 3\sigma$ corresponds to a 99.7 % confidence interval around the mean.

As can be expected, the laser sensors on the 64 coils had the least measurement noise. In particular, the standard deviation in the z axis using the four higher precision laser heads was only 0.15 µm, whereas it was 2.81 µm for the cameras on the 64 coils and 12.1 µm for the cameras on the MagFloor. The noise of the laser sensors in the x and y axes is greater than the z axis since the four sensors on the sides are less precise, but with longer range. The noise in the rotation axes for the laser sensors depends on both the precision of the sensor heads and how far apart the sensor heads are placed, as the rotation is measured from the difference in displacement readings between the heads. The noise in the α rotation axis is the smallest because the vertical heads are both high precision and spaced slighter farther apart in the y direction than they are in the x direction.

Since the cameras were placed about 1 m away from the center of the 64-coil prototype, but close to 4 m away from the center of the MagFloor, the sensor noise on the MagFloor is expected to be about 4 times greater than with the 64 coils. However, the noise is about 4–6 times greater between the MagFloor and the 64 coils. This could be because there is less light reflecting off the marker as they get farther away and they are harder for the cameras to see. Interestingly, the noise in the γ rotation axis is similar for the 64 coils between the cameras and the laser sensors.

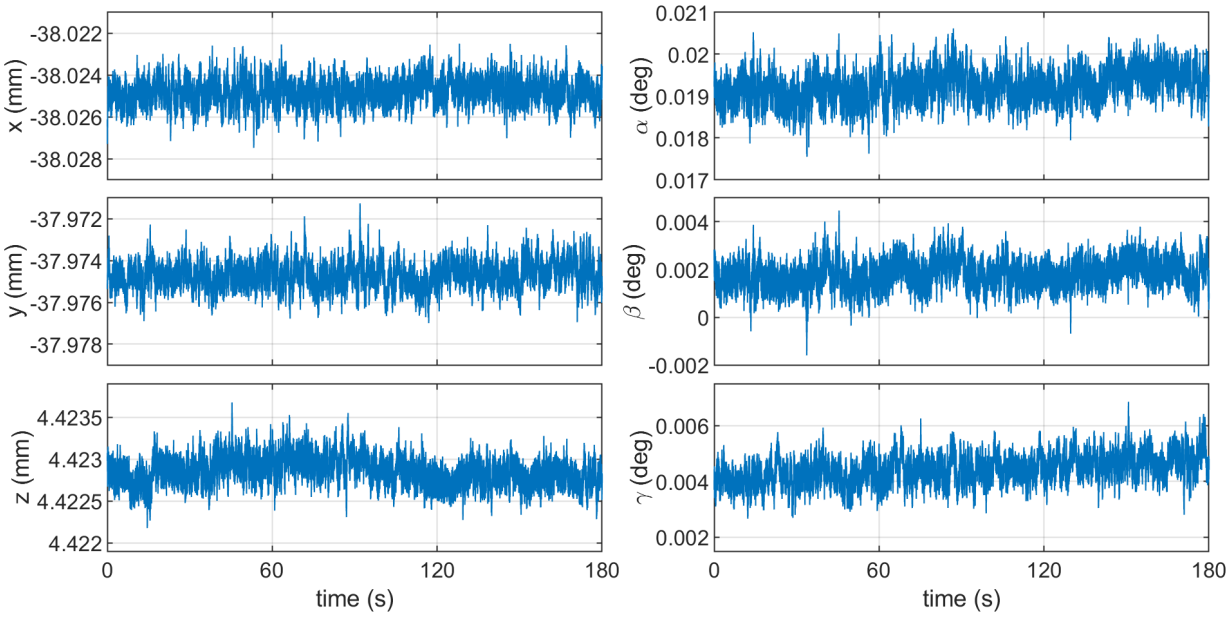

Figure 5.10: Measurement noise using laser sensors above 64 coils.

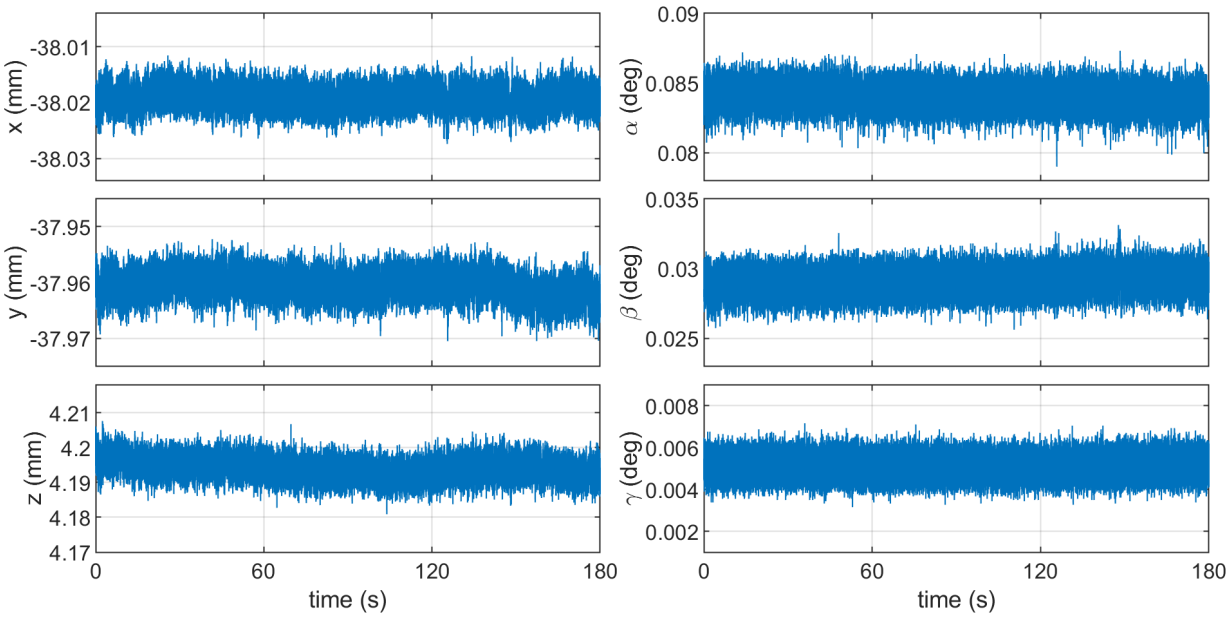

Figure 5.11: Measurement noise using Vicon cameras above 64 coils.

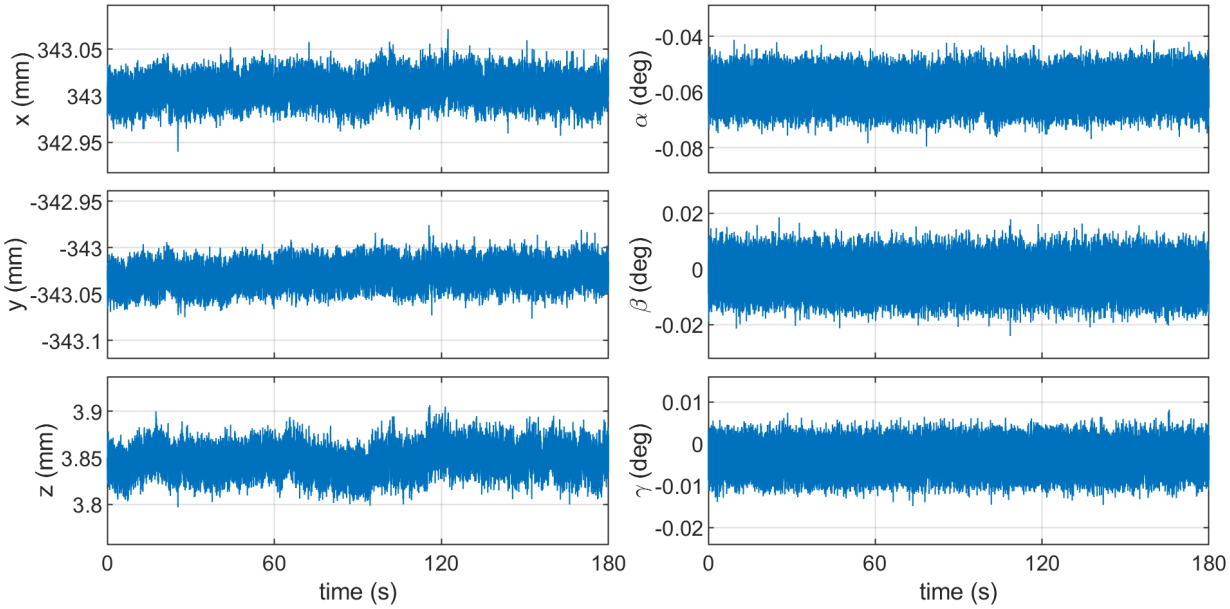

Figure 5.12: Measurement noise using Vicon cameras above the MagFloor.

Table 5.3: Standard deviation, σ, of the measurement noise in six axes for each system.

System	x (mm)	y (mm)	z (mm)	α (deg)	β (deg)	γ (deg)
			Standard Deviation, σ			
64 Coils Laser Sensors	0.00056	0.00060	0.00015	0.00036	0.00053	0.00048
64 Coils Cameras	0.00176	0.00209	0.00281	0.00074	0.00076	0.00045
MagFloor Cameras	0.0114	0.0101	0.0121	0.00415	0.00454	0.00255
			3 Standard Deviations, 3σ			
64 Coils Laser Sensors	0.00168	0.00179	0.00046	0.00107	0.00160	0.00144
64 Coils Cameras	0.00529	0.00626	0.00843	0.00222	0.00228	0.00135
MagFloor Cameras	0.0342	0.0302	0.0363	0.0124	0.0136	0.00765

Chapter 6

Experimental Results

In this section, the results of levitation experiments are presented from testing on the 64-coil prototype using camera feedback and laser feedback, and from using camera feedback on the MagFloor. With each system, very small precision steps are tested to determine the position resolution, the system delay is measured, and larger step responses and trajectory tracking are presented.

6.1 Levitation Precision

After tuning the controller, the mover was levitated and very small steps were taken in each axis to determine the position resolution of each system. Figures 6.1 and 6.2 show the precision on the 64-coil prototype using the laser displacement sensors and the camera system, and figure 6.3 shows the precision on the MagFloor using camera feedback. The steps in each axis were taken separately, so each subplot shows a separate trial.

From these tests, the standard deviation of the position error in each axis was recorded and is presented in table 6.1, along with 3σ, for which $\pm 3\sigma$ corresponds to a 99.7 % confidence interval. Using the 3σ rule, the motion precision is about 0.005 mm in the xyz translation directions and 0.002° in the $\alpha\beta\gamma$ rotations and for the laser sensors. For the camera system on the 64 coils, the precision is about 0.008 mm in xy, 0.011 mm in z, 0.003° in $\alpha\beta$, and 0.002° in γ. The MagFloor is less precise from placing the cameras further away and is about 0.03 mm in xyz, 0.015° in $\alpha\beta$, and 0.01° in γ. For the camera system, the motion precision is a similar magnitude to the measurement noise reported in section 5.5. However, for the laser sensors, the precision in xy is about 3 times larger than the noise, and the precision in z is about 12 times larger than the noise. This may indicate that the precision of the laser sensors in z is no longer limiting the levitation. The limiting factor may be the 500 Hz frequency of the measurement, hardware limitations, cross-coupling from other axes, or the surface roughness of the plates on the mover. However, these tests only measure the precision of the measurement and not the absolute accuracy, which can be worse when moving away from the reference position.

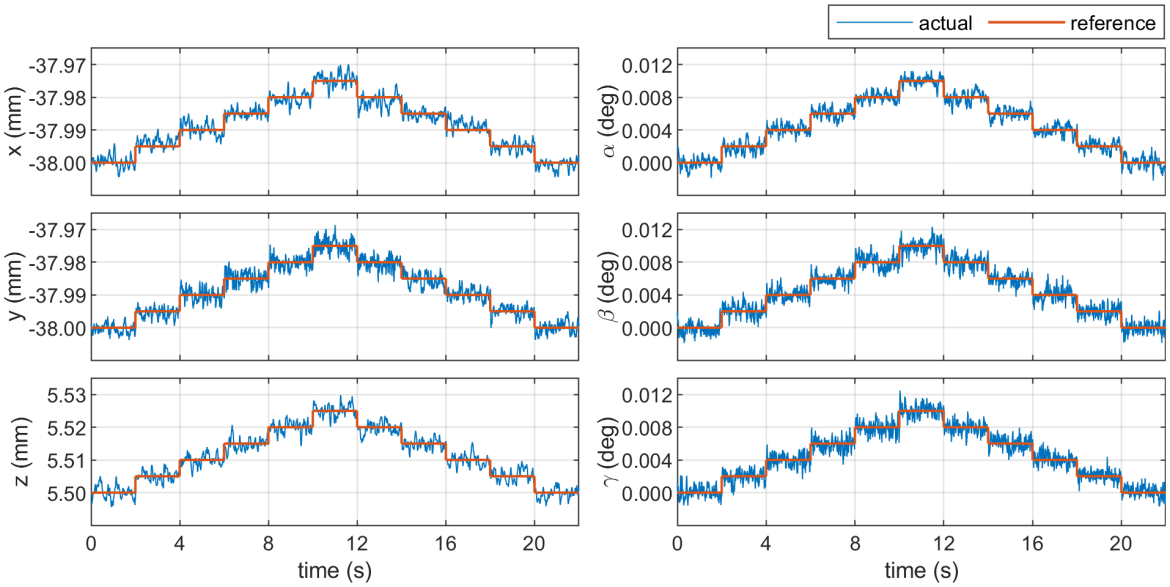

Figure 6.1: Precision in each axis using laser feedback on 64 coils. Steps of 0.005 mm are taken in the x, y, and z axes and 0.002° in the α, β, and γ axes.

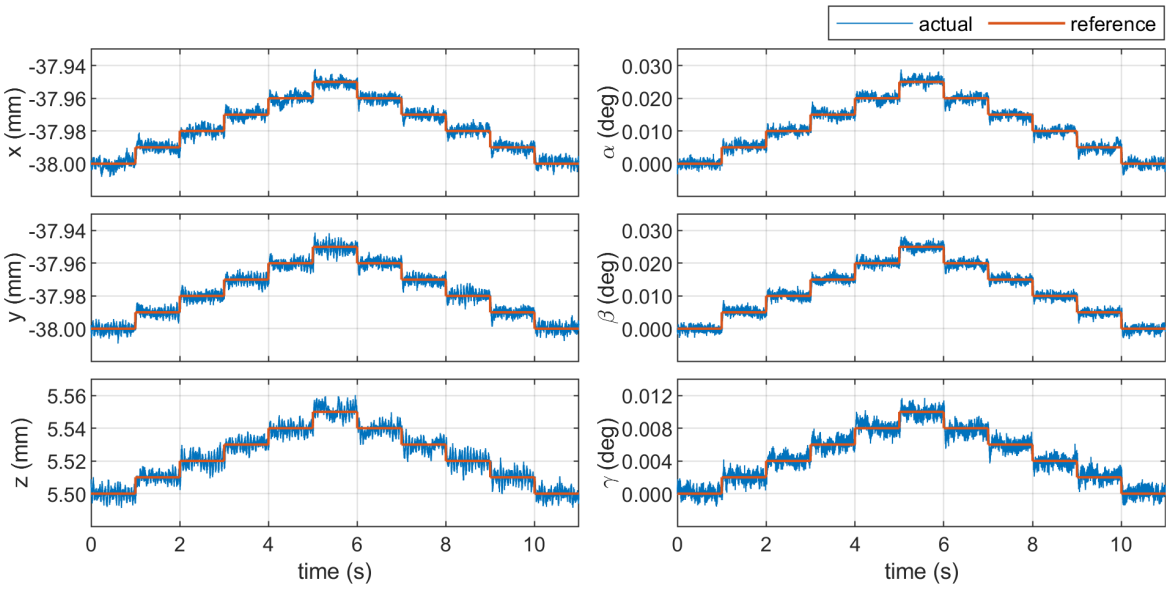

Figure 6.2: Precision in each axis using camera feedback on 64 coils. Steps of 0.01 mm are taken in the x, y, and z axes, 0.005° in the α and β axes, and 0.002° in the γ axis.

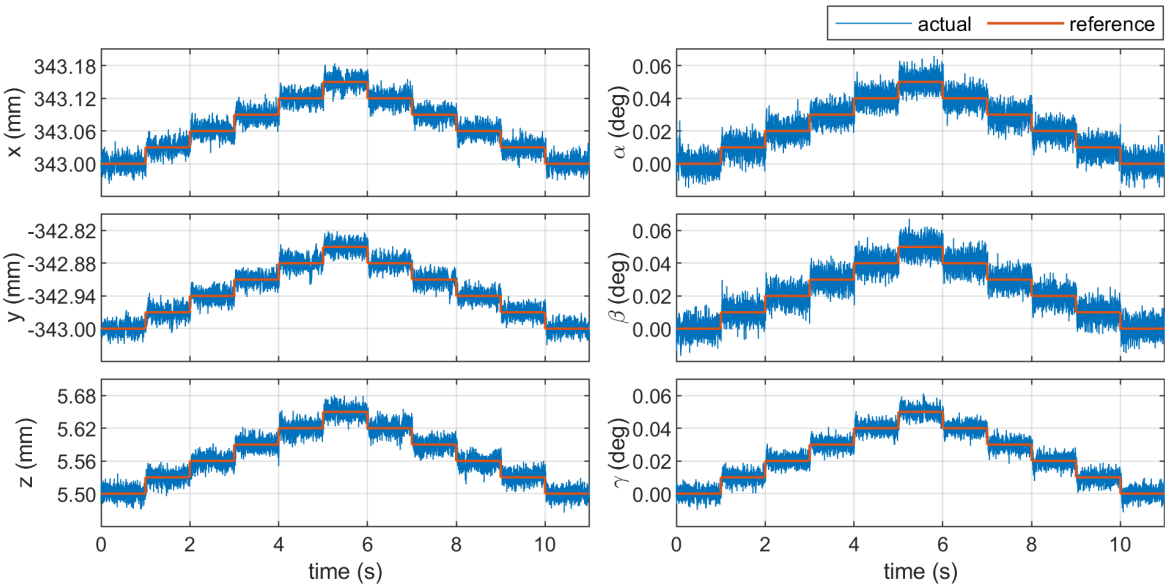

Figure 6.3: Precision in each axis using camera feedback on the MagFloor. Steps of 0.03 mm are taken in the x, y, and z axes and 0.01° in the α, β, and γ axes.

Table 6.1: Standard deviation, σ, of the levitation position error in six axes.

System	x (mm)	y (mm)	z (mm)	α (deg)	β (deg)	γ (deg)
			Standard Deviation, σ			
64 Coils Laser Sensors	0.00187	0.00180	0.00181	0.00063	0.00070	0.00069
64 Coils Cameras	0.00256	0.00256	0.00361	0.00116	0.00107	0.00064
MagFloor Cameras	0.0113	0.0106	0.0109	0.00476	0.00488	0.00325
			3 Standard Deviations, 3σ			
64 Coils Laser Sensors	0.00562	0.00540	0.00542	0.00190	0.00209	0.00208
64 Coils Cameras	0.00767	0.00769	0.01084	0.00349	0.00321	0.00192
MagFloor Cameras	0.0340	0.0317	0.0326	0.0143	0.0146	0.00976

6.2 System Latency

To test the system latency, steps of 1 mm, 4 mm and 8 mm were taken in the x direction on each system. These step sizes correspond to about a 1.1 A, 4.2 A and 8.0 A change in the current of some coils to force the mover. As such, it is expected that there should be very little actuation delay for the 1 mm step, but the 4 mm and 8 mm may add some delay as the current amplifiers reach the new target. For the 1 mm step, the delay is primarily due to the sensor system processing, communication to the PLC, computation of new targets in the PLC, and EtherCAT communication to the amplifiers.

To measure the delay, the time was measured for the mover to move a small amount once the step command was sent. For a small time frame, the integrator has little effect, and the derivative has no effect until the mover starts to move, since the derivative kick is removed with the strategy described in section 4.2. The control effort is therefore dominated by the proportional gain k_p, which was set to 10 000 N/m for both the camera and laser sensors on the 64 coils. The control effort once an 8 mm step is applied can be calculated using

$$u_p = (x - x_{\text{ref}})k_p = (0.008\,\text{m})(10\,000\,\text{N/m}) = 80\,\text{N}. \tag{6.1}$$

The time to move a short distance, such as 0.1 mm which is 1/80 of the step size, can then be calculated assuming a constant control effort

$$t = \sqrt{\frac{2d}{a}} = \sqrt{\frac{2d}{F/m}} = \sqrt{\frac{2(0.0001\,\text{m})}{(80\,\text{N})/(7.0\,\text{kg})}}\left(\frac{1000\,\text{ms}}{1\,\text{s}}\right) = 4.18\,\text{ms}. \tag{6.2}$$

The system latency can then be measured by find finding when the mover crosses this distance and subtracting the theoretical time calculated above. With this method, the system latency is approximately 6.1 ms, 6.5 ms and 6.8 ms in the 1 mm, 4 mm and 8 mm step responses, respectively, when using the laser sensors, as shown in figure 6.4. Using the camera-based motion tracker, the system latency is approximately 7.1 ms, 7.4 ms and 8.2 ms in the 1 mm, 4 mm and 8 mm step responses, respectively, as shown in figure 6.5. Since the delay is longer than the estimated time to move this small distance, the assumption of a constant control effort u_p for the short distance is reasonable. The system latency on the MagFloor is the same as on the 64 coils with the camera system since it uses the same hardware. As the current targets change smoothly during a ramp motion, with small changes between time steps, the 1 A test is the most applicable, and about a 7 ms delay can be expected when using the camera system for large motions on the MagFloor. Note that there can be some variation in the latency due to syncing of the hardware.

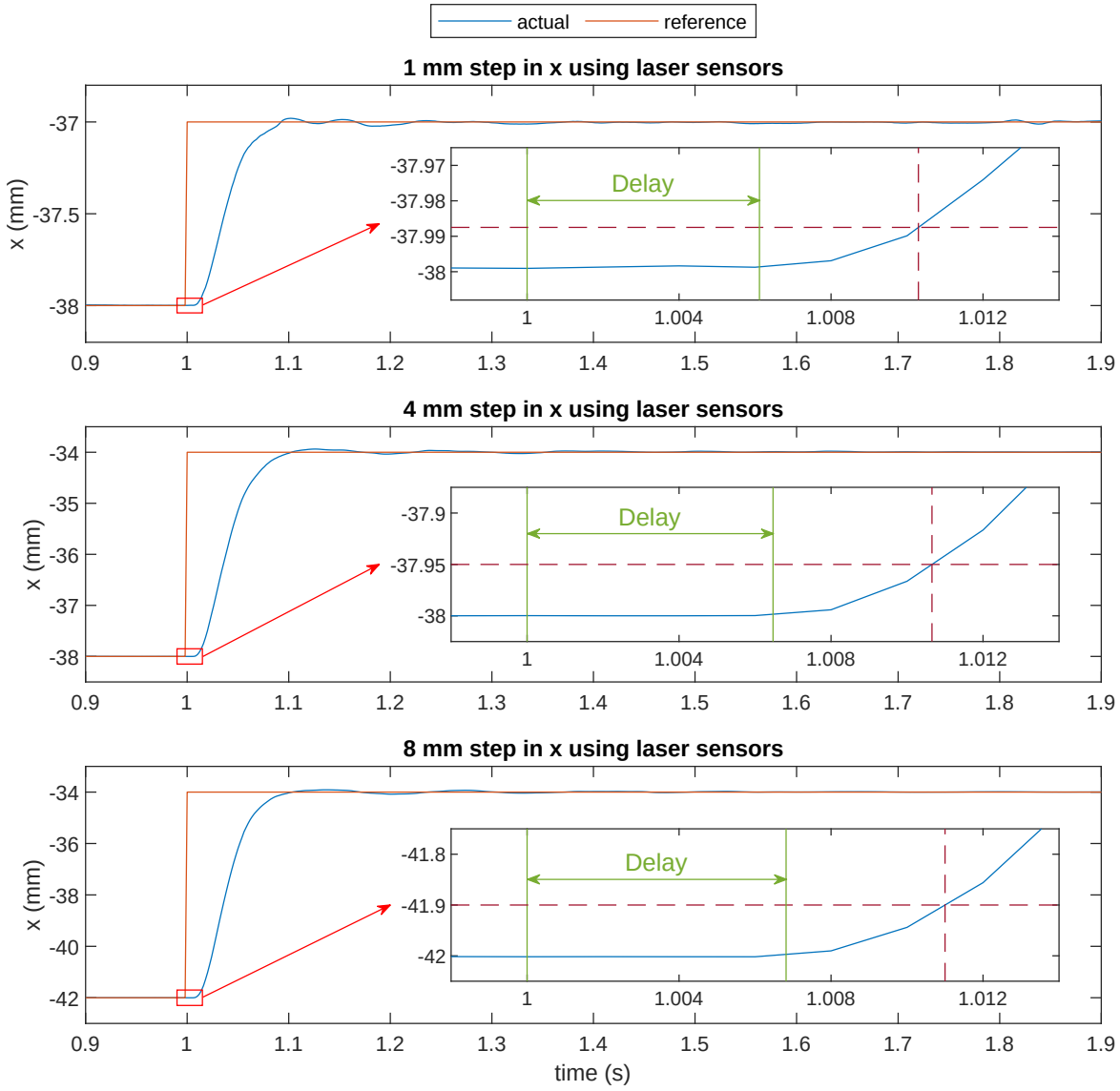

Figure 6.4: Steps of 1 mm, 4 mm and 8 mm taken in the x-axis to measure the system latency using the laser sensors.

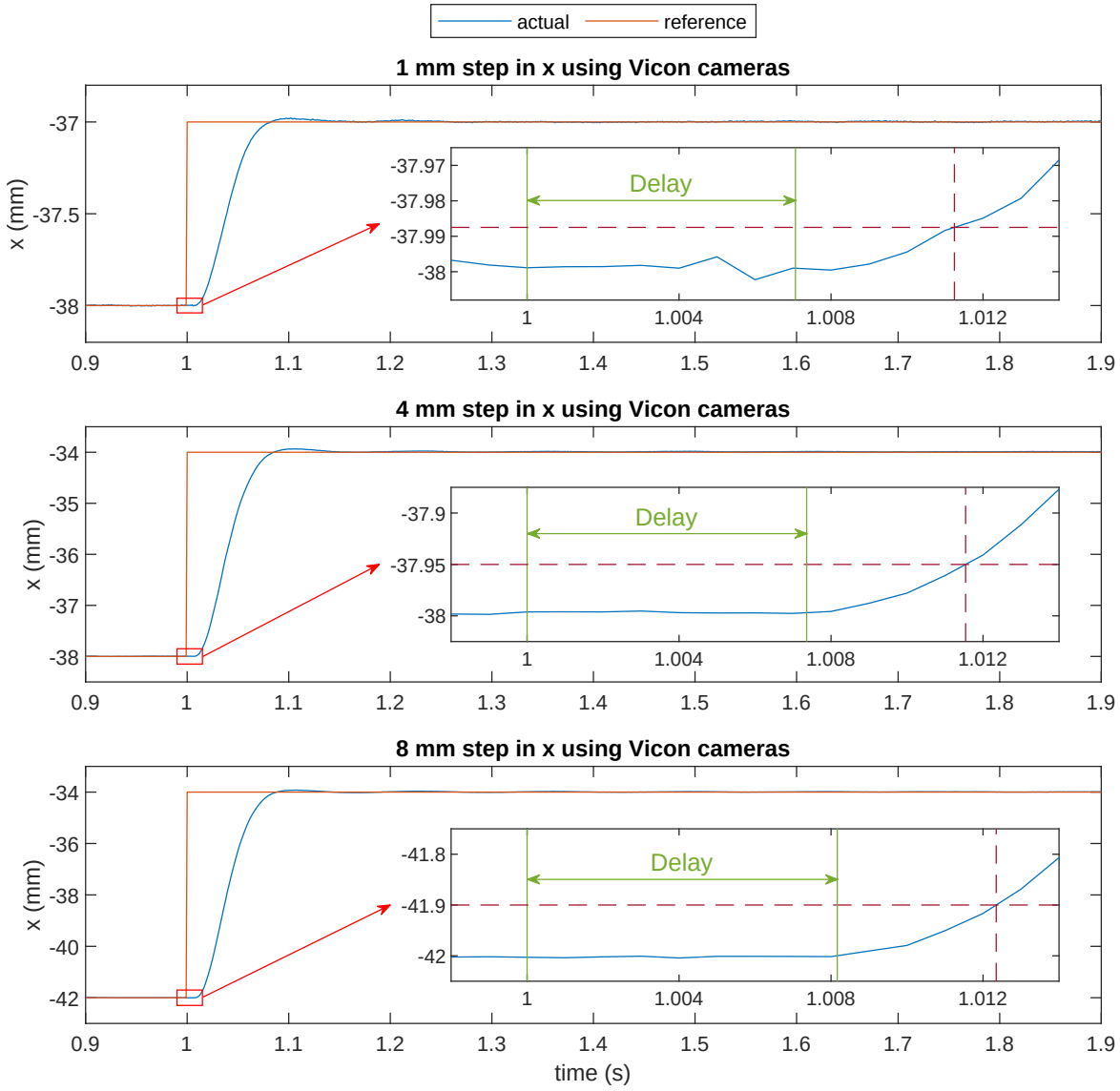

Figure 6.5: Steps of 1 mm, 4 mm and 8 mm taken in the x-axis to measure the system latency using the Vicon cameras.

6.3 Step Responses

The responses from an 8 mm step in the X_g direction on the 64-coil prototype are shown in figure 6.6. Averaging over the four steps taken in the test (two up and two down), the rise time is 0.049 s, the 2 % settling time is 0.092 s, and the overshoot is 1.41 % when using the laser sensors. When using the cameras, the rise time is 0.045 s, the 2% settling time is 0.088 s, and the overshoot is 0.275 %. Although the performance is similar between the two measuring systems, the performance with the camera system is better and shows smaller oscillations in x before settling. The disturbances in the γ axis are also much smaller when using the camera system, reduced from $\pm 0.05^\circ$ to $\pm 0.01^\circ$. One explanation for the better performance with the cameras is that flat plates were added for the laser sensors, increasing the mover's mass from 6.6 kg to 7.0 kg, which would slow it down. Note that the PID parameters were first tuned using the camera system and slightly adjusted in the $\alpha\beta$ rotation axes for the laser sensors. Further tuning of the gains in x with the laser sensors did not show significant improvement, so they were kept the same. A second reason is that the laser sensors only communicate to the PLC at 500 Hz, whereas the cameras communicate at 1000 Hz. Although the laser sensors have less delay and measurement noise than the cameras, operating the cameras at a higher frequency can still improve performance.

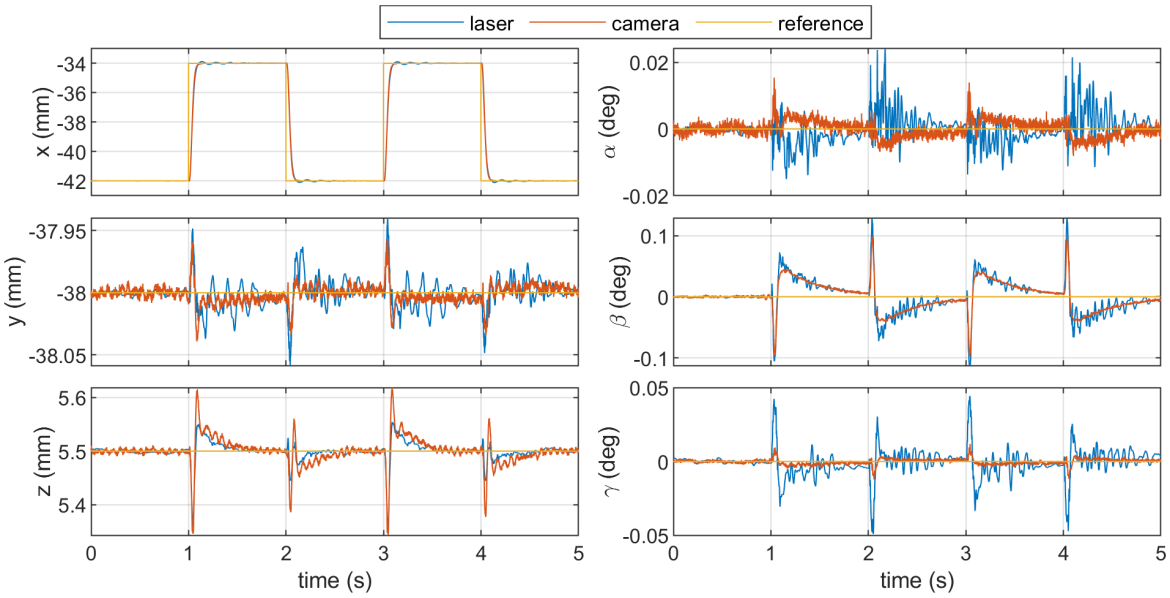

Figure 6.6: Responses from 8 mm step taken in X_g direction on the 64-coil prototype using laser versus camera feedback.

The response from an 8 mm step in X_g on the MagFloor is shown in figure 6.7. The average rise time is 0.045 s, the 2 % settling time is 0.578 s, and the overshoot is 14.0 %. The step response on the MagFloor is very different from the 64 coils because the PID parameters were tuned to have a much higher integrator gain, raising k_i from 4800 N/(m·s) to 35 000 N/(m·s) in the x axis between the two systems. This was done because there is a much greater steady-state error on the MagFloor from the cameras being placed further away. The higher integrator gains also allow the system can catch ramp trajectories much more quickly, which is important for the large motions on the MagFloor.

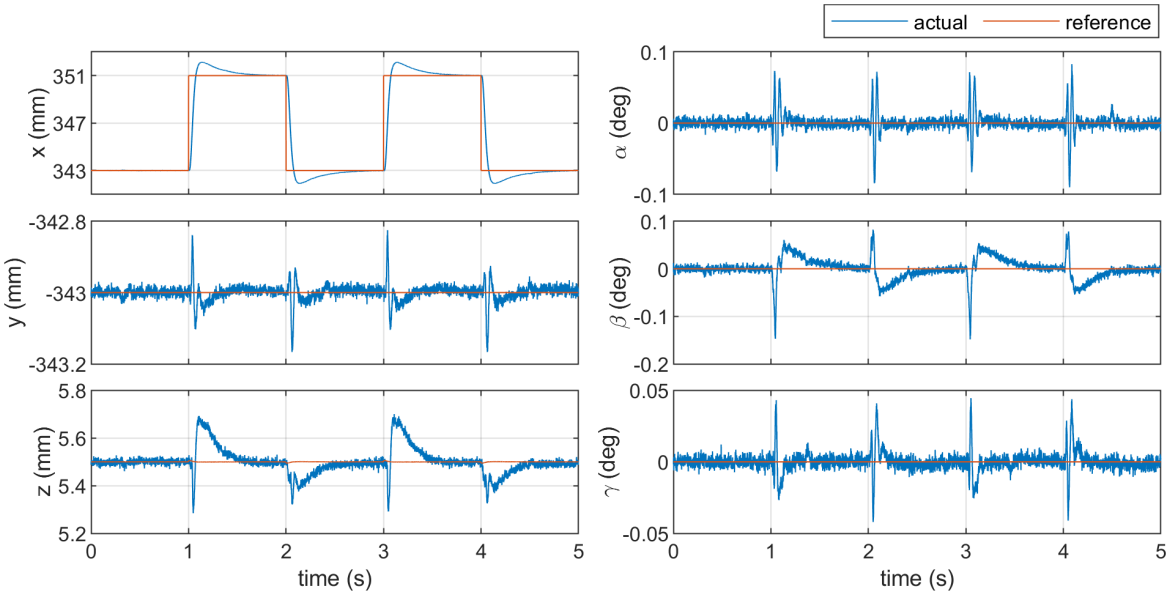

Figure 6.7: Response from 8 mm step taken in X_g direction on the MagFloor using camera feedback.

Figure 6.8 shows the responses from a 1 mm step in Z_g on the 64 coils. Using the laser sensors, the rise time is 0.048 s, the 2 % settling time is 0.572 s, and the overshoot is 14.5 %. The settling time is integrator dominated as there is a greater steady-state error and integrator gain in the Z_g direction. Using the camera system, the rise time is 0.048 s, the 2 % settling time is 0.769 s, and the overshoot is 13.2 %. The settling time is greater with the camera system as there is greater measurement noise and steady oscillations. The response from a 1 mm step in Z_g on the MagFloor is shown in figure 6.9. On the MagFloor, the average rise time is 0.051 s and the overshoot is 18.4 %. The measurement noise and steady oscillations are greater than 2 %, so this settling time cannot be calculated. However, the step response seems to reach steady-state after about 0.6 s.

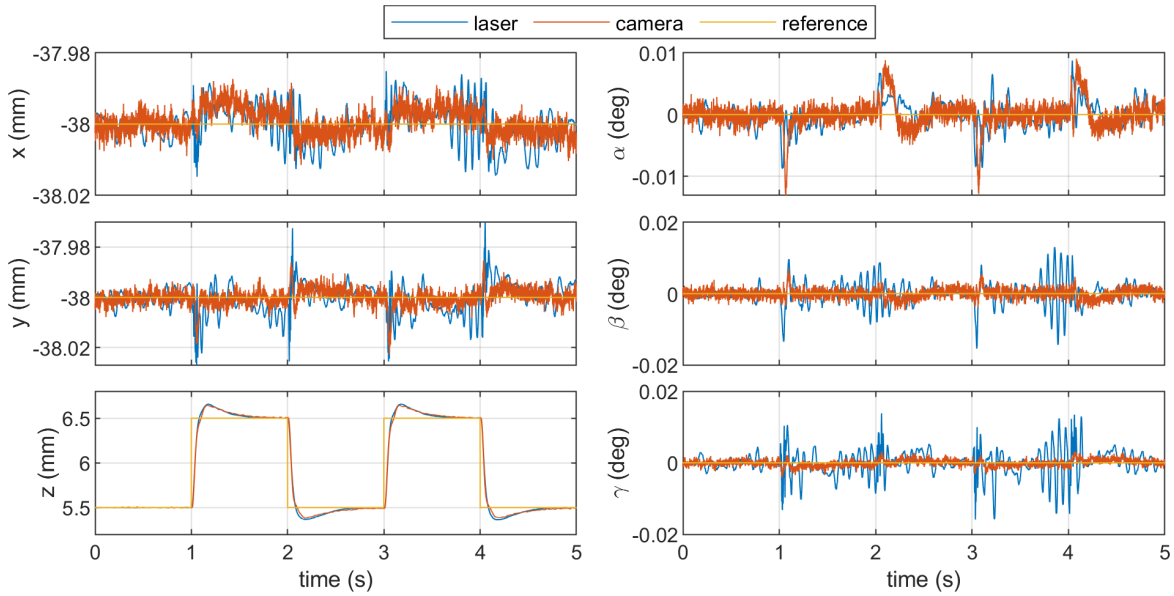

Figure 6.8: Responses from 1 mm step taken in Z_g direction on the 64-coil prototype using laser versus camera feedback.

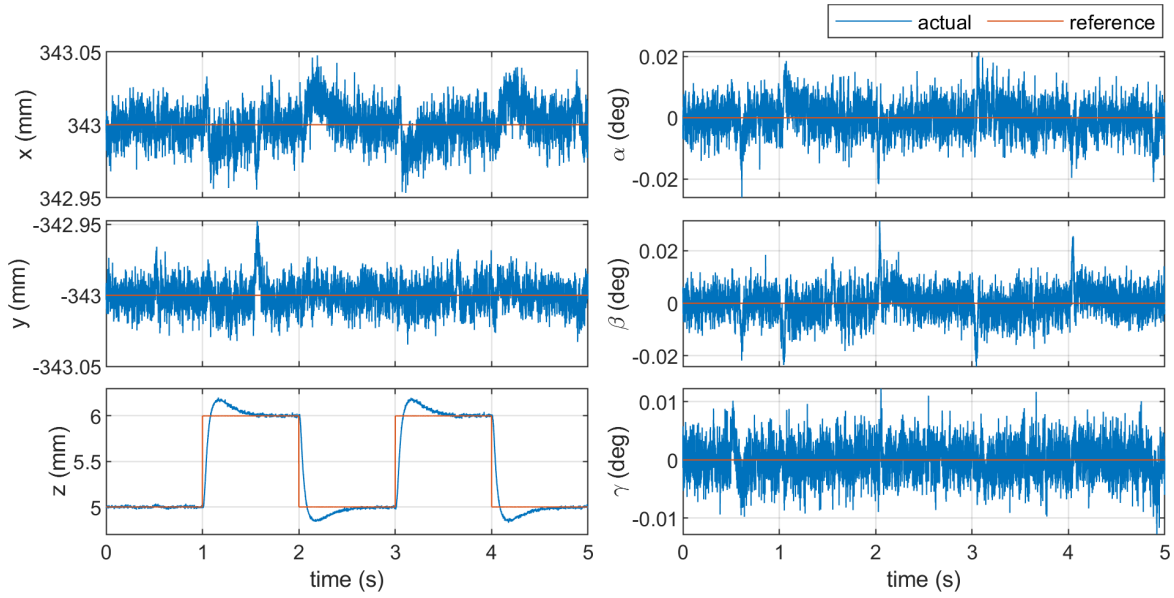

Figure 6.9: Response from 1 mm step taken in Z_g direction on the MagFloor using camera feedback.

The responses from a step of 1° in the yaw γ direction on the 64 coils are shown in figure 6.10. Using the laser sensors, the average rise time is 0.042 s, the 2 % settling time is 0.128 s, and the overshoot is 3.33 %. The disturbances are around ±0.03 mm in the xyz axes, ±0.015° in the α axis, and ±0.03° in the β axis. Note that the γ step with the camera system was taken at an x position of 38 mm, but the x data was shifted by −76 mm to plot alongside the laser sensor response. As this is simply shifting by one coil spacing, the response is comparable. Using the camera system, the rise time is 0.037 s, the 2 % settling time is 0.120 s, and the overshoot is 4.06 %. The performance between the laser sensors and the cameras is very similar in the γ step, and the disturbances in other axes are also similarly small. Steps larger than 1° in γ are possible, as this is far away from saturating the coil currents. In contrast, the 8 mm steps in the X_g direction shown in figures 6.6 and 6.7 are closer to saturation and have greater disturbances in the other axes.

Because of a greater steady-state error on the MagFloor, the PID gains in the γ direction were increased, the integrator gain in particular. This resulted in more overshoot and greater settling time for the 1° step in the yaw γ direction on the MagFloor, as shown in figure 6.11. On the MagFloor, the average rise time is 0.032 s, the 2 % settling time is 0.691 s, and the overshoot is 14.9 %. The disturbances in other axes are also much greater on the MagFloor for the γ step, and the levitation height dips about 0.1 mm.

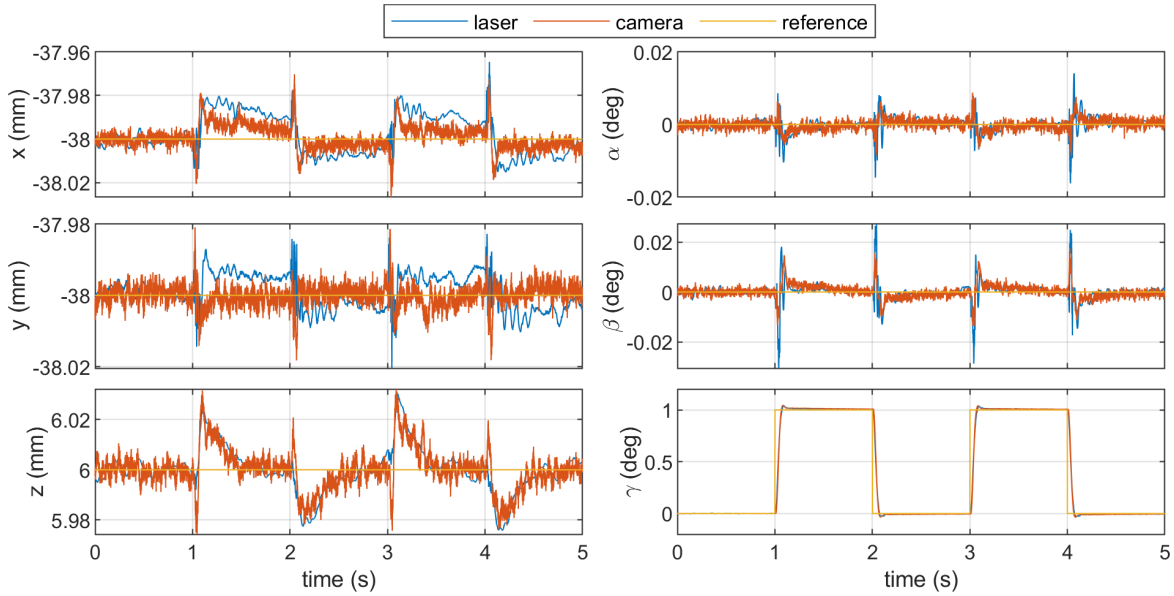

Figure 6.10: Responses from 1° step taken in γ direction on the 64-coil prototype using laser versus camera feedback.

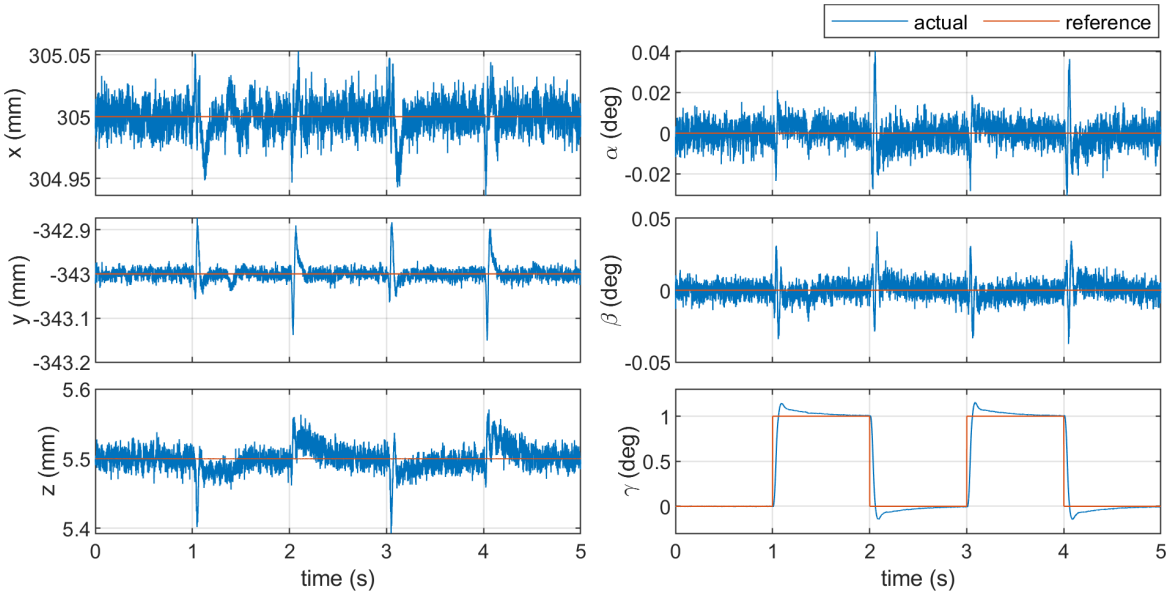

Figure 6.11: Response from 1° step taken in γ direction on the MagFloor using camera feedback.

Note that some of the steps were taken 0.5 mm lower on the MagFloor, since the aluminum cover sheet above the coils is 0.5 mm thinner on the MagFloor, reduced from 1.8 mm thick on the 64 coils to 1.3 mm thick on the MagFloor. Because the cover sheet is thinner, it provides less eddy-current damping force and is also further away from the mover for the same levitation height. Levitating 0.5 mm lower on the MagFloor makes the gap between the mover and the cover sheet the same as on the 64 coils, for more similar damping, but still less.

6.4 Trajectory Tracking and Motion Range

When using the laser displacement sensors, the xy movement range is limited to about $\pm 36\,\text{mm}$, with some buffer between the $\pm 40\,\text{mm}$ sensor range. Levitation heights of 4.5 mm to 7.5 mm are supported on both the 64 coils and the MagFloor. The minimum height is due to a 1.5 mm gap between the coil winding and the top of the square bobbin, a 1.8 mm thick aluminum cover sheet over the coils, and a 1 mm thick aluminum sheet mounted on the bottom of the mover. The motion range in the α and β rotations depends on the levitation height and the size of the mover. At a levitation height of 5.5 mm, the $\alpha\beta$ range is about $\pm 0.3°$, and at a levitation height of about 6.5 mm, the $\alpha\beta$ range is about $\pm 0.6°$. However, since the z levitation gap can oscillate when moving, the rotation range is further limited during horizontal motion. A 68 mm by 68 mm square trajectory at 300 mm/s with a reference acceleration of $2500\,\text{mm/s}^2$ is shown in figure 6.12. The overshoot is 1.6 mm at the ends of the ramp. The fluctuation in $\alpha\beta$ is within $\pm 0.17°$ and is larger in one direction than the other. This inconsistency could indicate some global offset error during the sensor calibration stage.

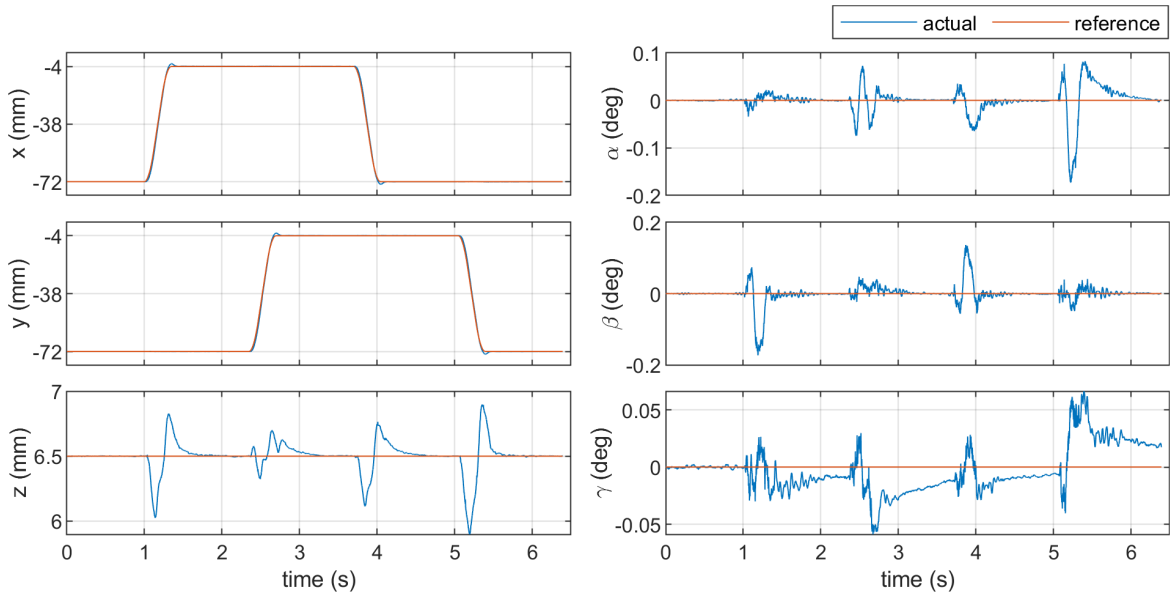

Figure 6.12: Square trajectory of 68 mm by 68 mm at 300 mm/s on the 64 coils using the laser displacement sensors.

The motion range in γ is about $\pm 20°$ with the laser sensors, and a ramp at $75\,°/\text{s}$ with acceleration of $200\,°/\text{s}^2$ is shown in figure 6.13. During this rotation, the fluctuation is

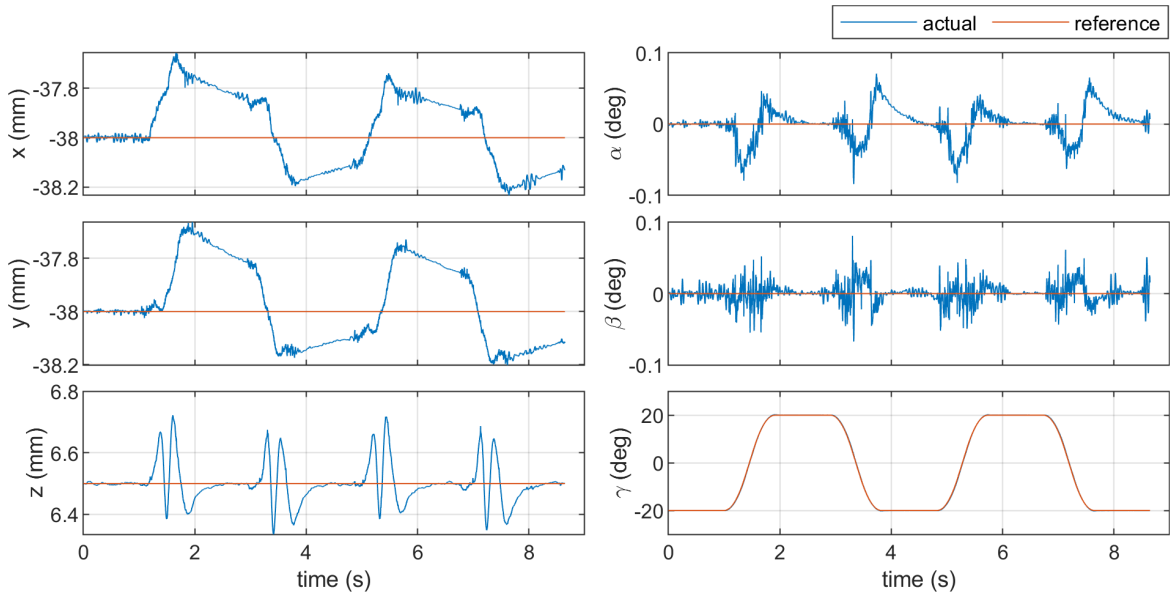

Figure 6.13: Yaw ramp at 75 °/s from -20 to 20 degrees using the laser sensors.

within ±0.35 mm in xy, ±0.22 mm in z, and ±0.09° in $\alpha\beta$. Even if the laser sensors could measure larger rotation ranges, infinite rotation is not possible at the $x = -38$ mm and $y = -38$ mm location due to force and torque limitations. At this location, the center of the mover is above a coil center and if the mover were rotated 45° in yaw, many of the coil centers would align with gaps in the Halbach array, resulting in an inability to produce sufficient levitation force. However, this location is power efficient for levitation at the $\gamma = 0°$ orientation. Full yaw rotation is possible in other locations.

The xy motion range on the 64-coil prototype using the camera system is expanded to ±120 mm, with a 15 mm buffer around the border of the stator. Figure 6.14 shows a square motion over the full 240 mm range in x and y at 300 mm/s, with a reference acceleration of 2500 mm/s^2 at the start and ends of the ramp. During this square, the fluctuations in other axes are similar to that with the laser system and are about ±0.5 mm in z, ±0.2° in $\alpha\beta$, and ±0.06° in γ.

As shown in figure 6.15, the yaw rotation γ range is unlimited when using the camera system and can support the full 360°. This unlimited rotation is only possible at certain locations on the stator. At the xy location shown in figure 6.15, the mover center is between two coils and sufficient levitation force can be provided throughout the entire 360° rotation. With a rotation speed of 75 °/s and acceleration of 75 °/s^2, the fluctuation is less than ±0.1° in $\alpha\beta$ and around 0.2 mm in z, which is similar to with the laser sensors.

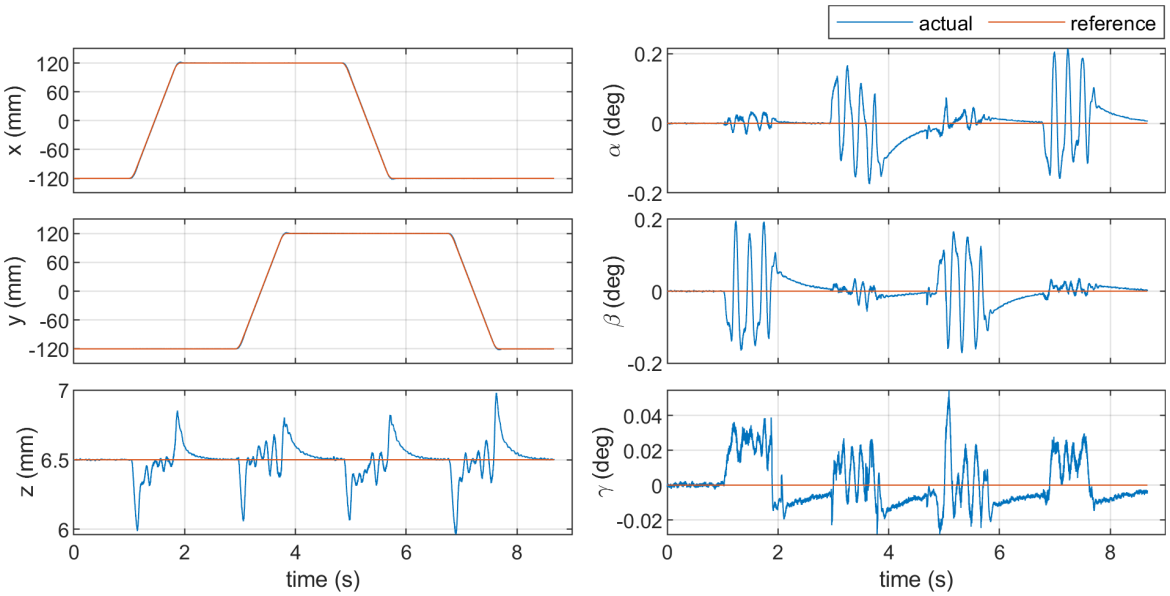

Figure 6.14: Square trajectory of 240 mm by 240 mm at 300 mm/s on the 64 coils using the camera system.

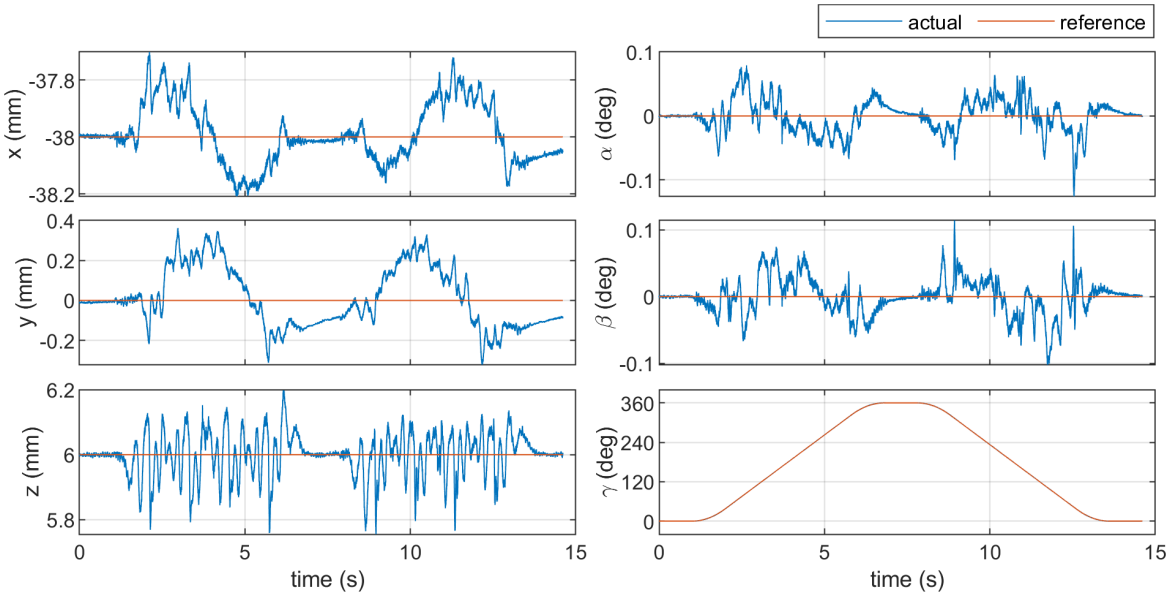

Figure 6.15: Yaw ramp at 75 °/s showing full 360-degree range on the 64 coils using the camera system.

The maximum linear speed on the maglev system is found to be 500 mm/s, and an x ramp at the maximum speed on the 64 coils is shown in figure 6.16. A reference acceleration of 2500 mm/s^2 is used for a smooth start and end of the ramp. Accelerating too quickly or moving faster than 500 mm/s can cause the mover to touch the surface of the stator or cause instability. Considering only the regions under constant speed and averaging over the four ramps taken, the mean absolute error in the x position is 2.803 mm, and there is about a 2 mm overshoot at the end of the ramp. The fluctuation is from 5.6 mm to 7.2 mm in z, between $\pm 0.2^\circ$ in β, and is small in the other axes.

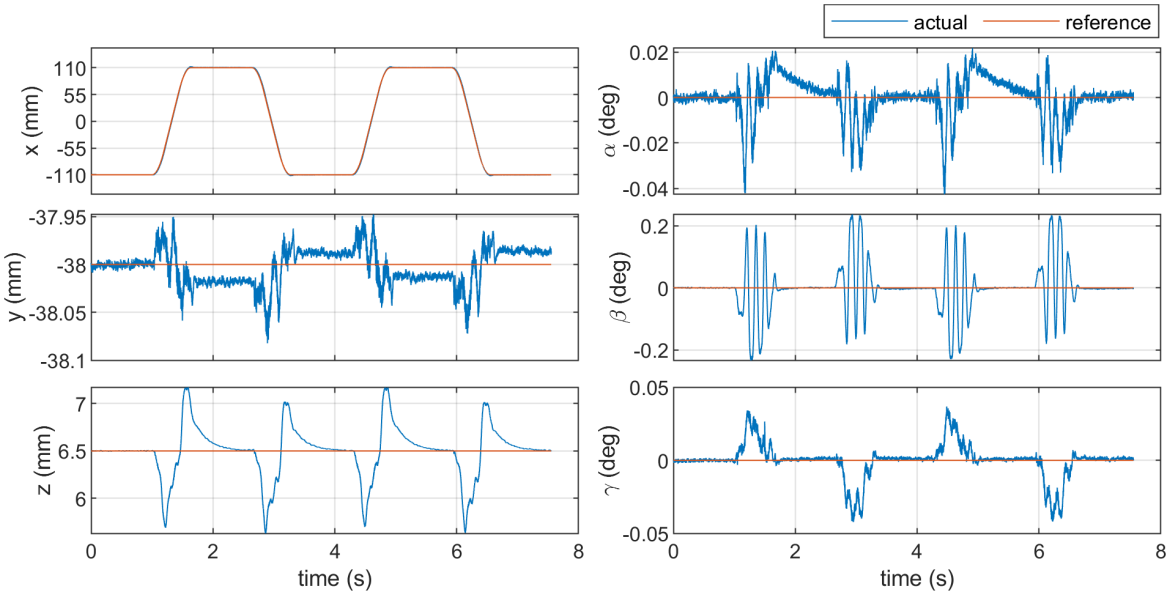

Figure 6.16: X-ramp at 500 mm/s on the 64 coils using the camera system.

On the MagFloor, the movement range is about ± 1030 mm in x and ± 727 mm in y, as shown in figure 6.17. This allows for about a 20 mm buffer between the edge of the mover and the edge of the stator. This motion is at a speed of 500 mm/s, with an acceleration of 2500 mm/s^2, which is about the maximum the MagFloor can support, similar to the 64 coils. During this motion, there are larger fluctuations of 1.5 mm in z, $\pm 0.45^\circ$ in $\alpha\beta$, and -0.22° to 0.15° in γ. The xy motion overshoots the end of the ramp by up to 3.5 mm. The larger disturbances on the MagFloor can be attributed to the higher steady-state error from less accurate camera measurements. Also, only some coil locations were measured and the rest were interpolated. Considering only regions of constant speed, the mean absolute error is 0.326 mm for the x ramps and 0.297 mm for the y ramps, which is much lower than on the 64 coils. This can be attributed to the greater integrator gains.

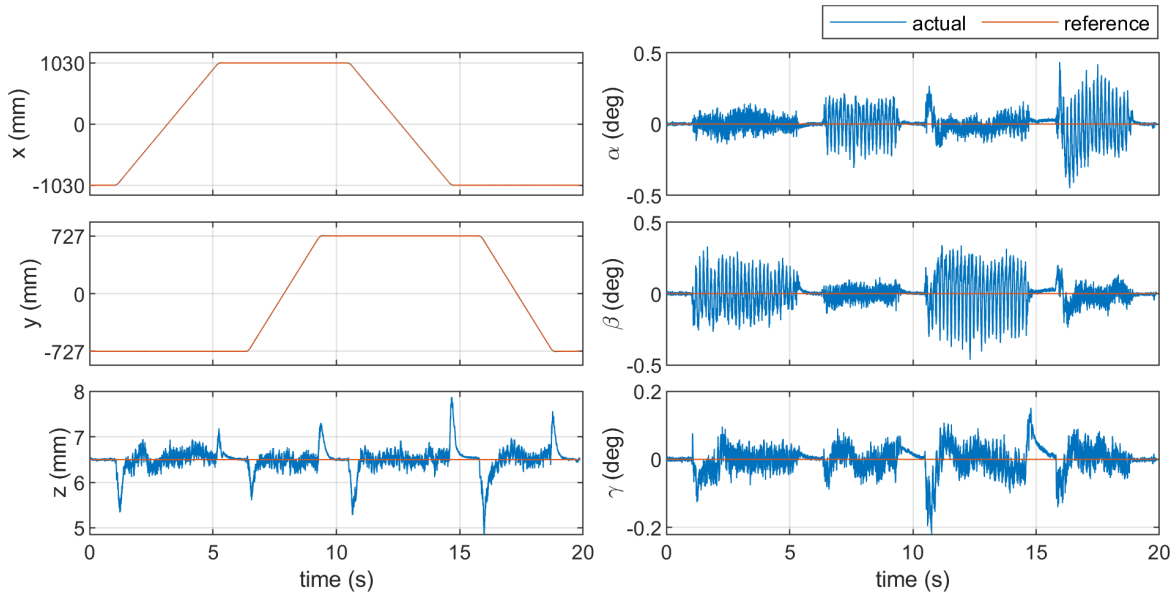

Figure 6.17: Rectangle trajectory of 2060 mm by 1454 mm at 500 mm/s on the MagFloor using the camera system.

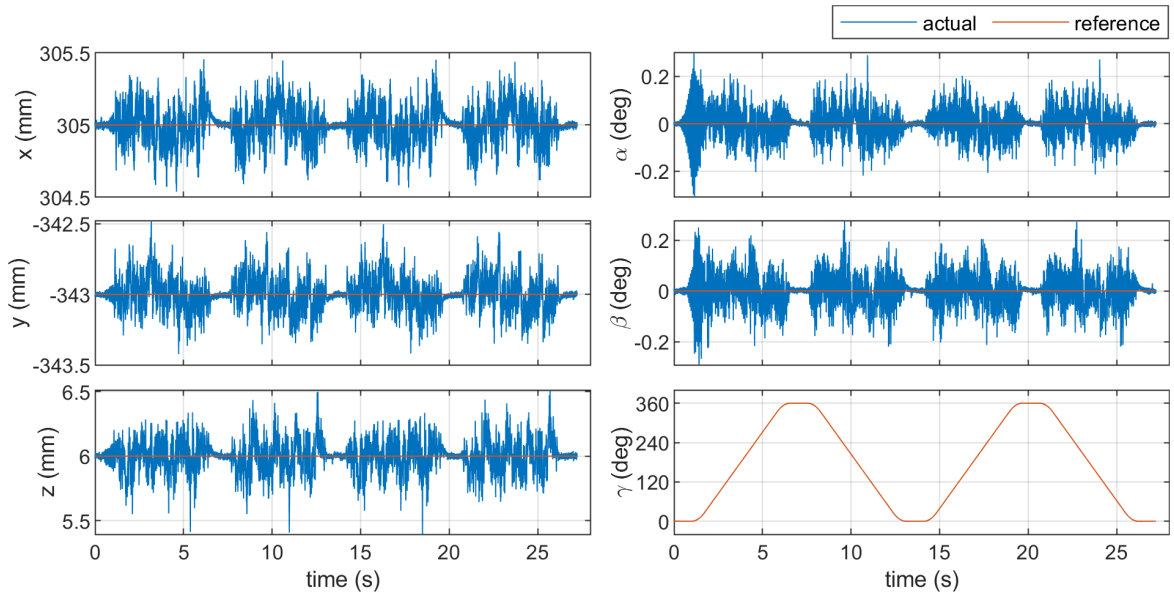

Figure 6.18: Yaw ramp at 75 °/s showing full 360-degree range on the MagFloor using the camera system.

Because the cameras are used on the MagFloor, the yaw γ rotation range is unlimited, as shown in figure 6.18. This rotation is at a speed of 75 °/s with acceleration of 100 °/s^2. The fluctuations were within about ±0.5 mm in the xyz axes and 0.3° in the $\alpha\beta$ rotations. These fluctuations were also much larger than seen in figure 6.15 on the 64 coils, despite the mover rotating at the same speed. This can be attributed to the greater error in the system, similar to the other tests.

Tracking of a circular trajectory on the 64 coils with the camera system is tested in figure 6.19. The circular path has a diameter of 240 mm and speeds of 100 mm/s, 200 mm/s, and 300 mm/s were tested. The mover completed multiple revolutions of the circle and a middle loop is plotted such that the mover is under constant motion. For this middle loop, the mean absolute error in the xy position is 0.359 mm, 0.878 mm, and 1.286 mm for the respective speeds. A similar test on the MagFloor is shown in figure 6.20, with a circle diameter of 994 mm and speeds of 100 mm/s, 300 mm/s, and 500 mm/s. The mean absolute error in the xy position is 0.166 mm, 0.311 mm, and 0.767 mm for the respective speeds. A figure-eight path is also tested on the MagFloor and is shown in figure 6.21. For this test, the mean absolute error in the xy position is 0.124 mm, 0.191 mm, and 0.387 mm for the respective speeds. However, these are only the maximum speeds and the tangential velocity varies throughout the figure-eight due to the way the trajectory is developed. Overall, the MagFloor has a smaller mean absolute error on the trajectories, which can be attributed to the greater integrator gains.

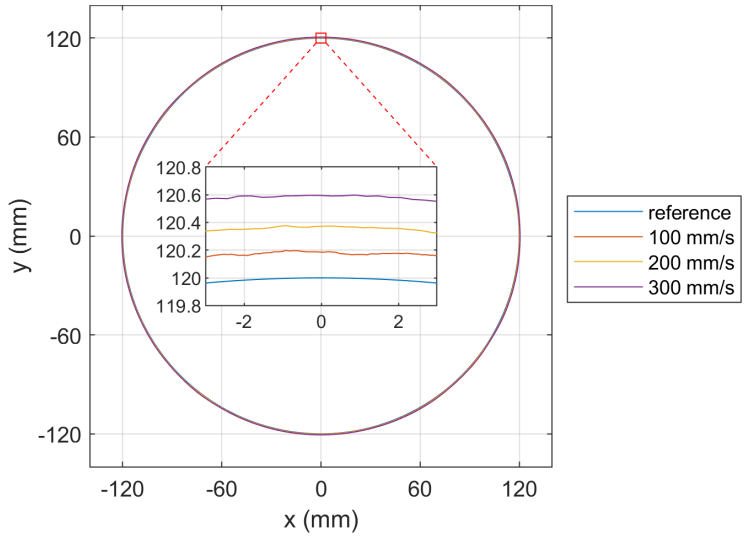

Figure 6.19: Tracking of a circular path at 100 mm/s, 200 mm/s, and 300 mm/s on the 64 coils using the camera system.

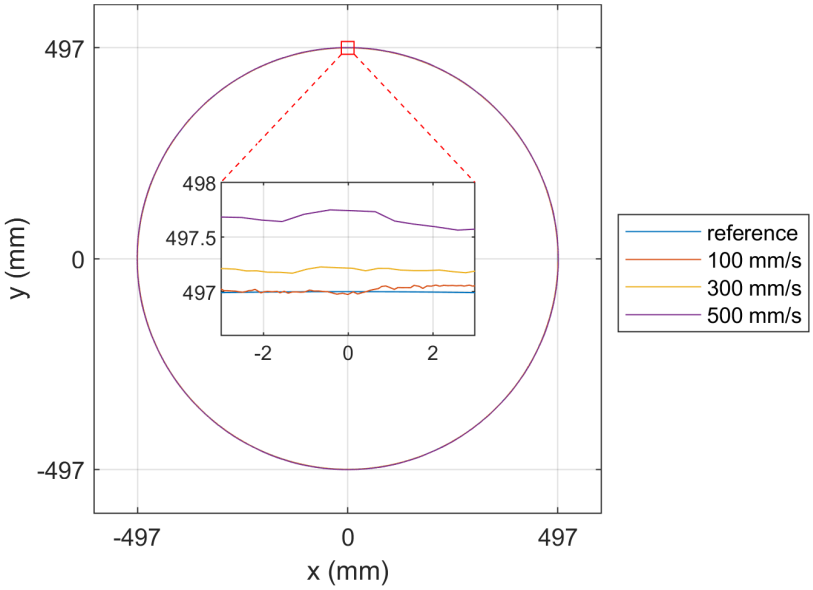

Figure 6.20: Tracking of a circular path at 100 mm/s, 300 mm/s, and 500 mm/s on the MagFloor using the camera system.

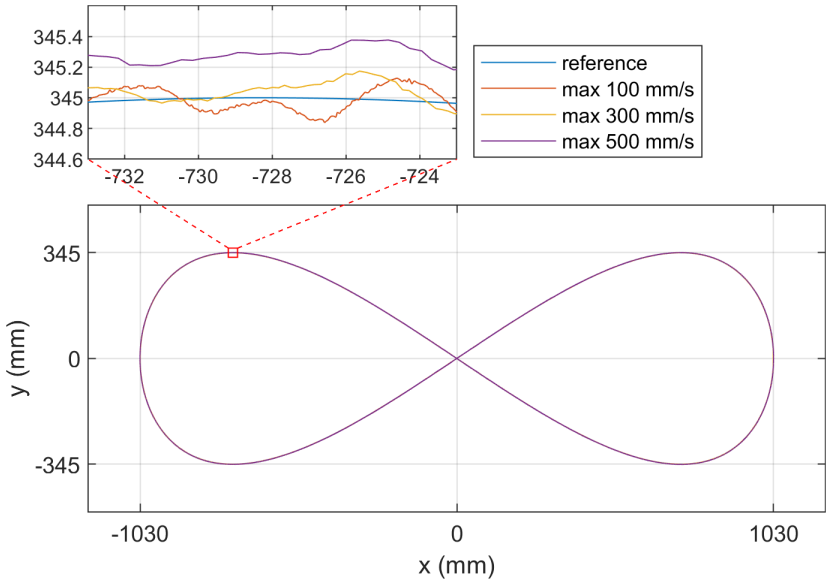

Figure 6.21: Tracking of a figure-eight path at 100 mm/s, 300 mm/s, and 500 mm/s on the MagFloor using the camera system.

Chapter 7

Controller Improvements

In this chapter, some preliminary investigation is completed into improvements to the controller, such as adding a state estimator and implementing an iterative learning controller (ILC). The goal of the state estimator is to compensate for the system latency by using an estimate of the mover's velocity to estimate the actual position of the mover at the time the coil currents will be applied. With ILC, the goal is to improve the control by adding a feedforward control effort based on learning from past iterations of the same trajectory. The tests in this chapter were done using only the Vicon camera-based motion tracker for sensor feedback since the goal is to improve the large motion trajectory tracking.

7.1 Delay Compensation with a State Estimator

As discussed in section 6.2, the system latency with the camera feedback was measured to be about 7 ms for small changes in coil currents. If the mover is travelling at a speed of 500 mm/s, then this latency means that the wrench transformation matrix and coil currents were calculated at a position 3.5 mm away from where the mover will be when those currents are applied. This error in calculating the currents means that there are large errors in the actual forces and torques applied to the mover for which the controller has to compensate.

An estimate of the force and torque error caused by this effect during the 500 mm/s x ramp in figure 6.16 is shown in figure 7.1. To estimate this error, the control efforts from the PIDs and the camera position measurements were logged during the test and used to calculate a current map for each time step. Then, the actual position of the mover was estimated using the velocity of the reference and assuming a 7 ms time delay. A new wrench transformation matrix was generated at this position and with the current map from before, an estimate of the actual forces and torques on the mover was generated. The force and torque error plotted in figure 7.1 is then the difference between the estimated forces and torques and those desired by the PIDs. This plot shows that at the start of the ramp motions, there is an error of about -15 N in F_z, which explains the dip in the

levitation height at the start of each ramp. The controller then compensates by increasing the control effort, which causes the jump in z at the end of the ramp when the motion stops. There is also a fluctuation in T_y, the torque about the y axis, between $\pm 0.83\,\mathrm{N\cdot m}$, which could contribute to the fluctuation seen in the β rotation. Interestingly, the force error in x is in the direction of the motion and helps to offset the eddy-current damping during motion, meaning the integrator in x doesn't need to grow as large.

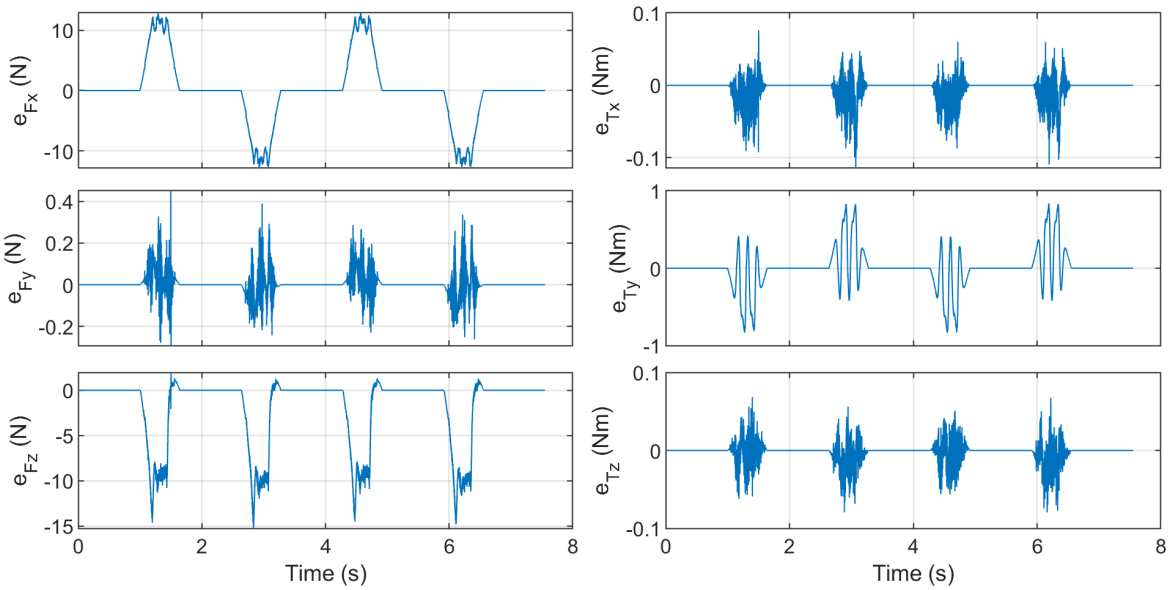

Figure 7.1: Estimated force and torque error caused by system latency during the 500 mm/s x-ramp on the 64 coils.

To compensate for the system latency, an estimate of velocity is used to estimate the position at the time the current map will be applied. Both the position measurements from the camera system and the velocity estimate using the derivative are propagated 7 ms forward in time by using the past control efforts from the PD terms of the PIDs. The integrator control effort is excluded from this calculation as it is assumed that this is compensating for system error and does not contribute to the acceleration of the mover. For example, in steady-state, the PD effort should go to 0, but the integrator may still have some value. First, an estimate of the velocity is computed by the discrete derivative of position measurements as before. The velocity estimate is then filtered using a modified low-pass filter which updates its state using both the past control effort and the new velocity estimate

$$v_{n-7,f} = 0.25 v_{n-7} + 0.75 \left(v_{n-8,f} + \frac{F_{n-8}}{m} T_s \right), \tag{7.1}$$

where v_{n-7} is the new velocity estimate from the measurement derivative, F_{n-8} is the PD control effort from 8 time steps ago (8 ms), m is the mass of the mover, and T_s is the time step. For the rotation axes, the moment of inertia is used instead of the mass. The same filter parameters are used on both the 64 coils and the MagFloor for the state estimator.

The position measurement and velocity estimate are then updated together using the PD control efforts from the past 7 time steps

$$v_{n,f} = v_{n-7,f} + \sum_{i=0}^{6} \frac{F_{n-7+i}}{m} T_s, \tag{7.2a}$$

$$x_n = x_{n-7} + \sum_{i=0}^{6} v_{n-7+i,f} T_s. \tag{7.2b}$$

This new position estimate is used to compute the error for the proportional and integrator term. The difference between the derivative of the reference and the new velocity estimate is used to compute the derivative term. Since the velocity estimate is already filtered and the reference is not noisy, no extra filter is added after the derivative term. With this approach, the PID will now be trying to minimize the error between the position estimate and the reference. During long motion where the integrator can catch the ramp, the camera measurement is approximately equal to the reference from 7 ms ago, while the position estimate is close to the present reference. Note that since the velocity estimate comes from the derivative of the measurements and is noisy, the position estimate is noisier than the raw camera measurements.

7.2 State Estimator Results

An x ramp at 500 mm/s on the 64 coils with and without the state estimator is shown in figure 7.2. Using the state estimator reduces the fluctuations in the z axis from between 5.6 mm to 7.2 mm without the estimator, to between 6.2 mm to 7.0 mm with the estimator. The fluctuations in the β axis are larger in one direction than the other using the state estimator, which could indicate there was some error in the camera calibration. As the force error without the estimator helps to push the mover in the direction of motion and offset the eddy-current damping force, adding the estimator increases the tracking error in the x axis. Considering only the regions of constant speed motion, the mean absolute error in x increases from 2.803 mm to 4.851 mm by adding the estimator. Note that in calculating the error with the state estimator, the measurement is compared to the reference from 7 ms ago, as this is approximately what the controller is trying to minimize.

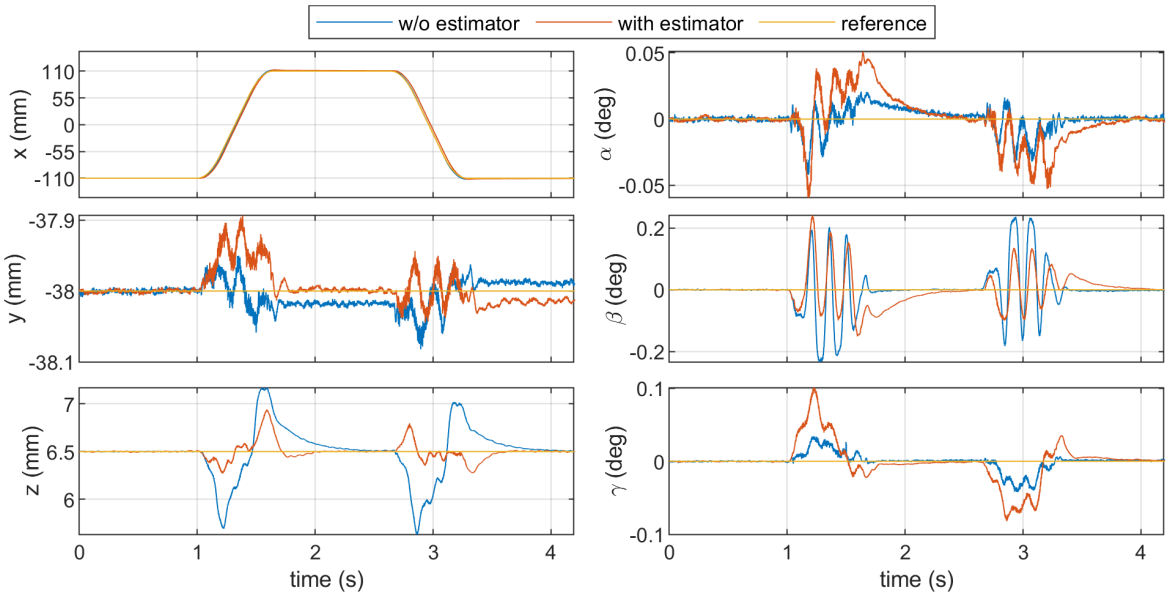

Figure 7.2: X-ramp at 500 mm/s on the 64 coils with and without the state estimator.

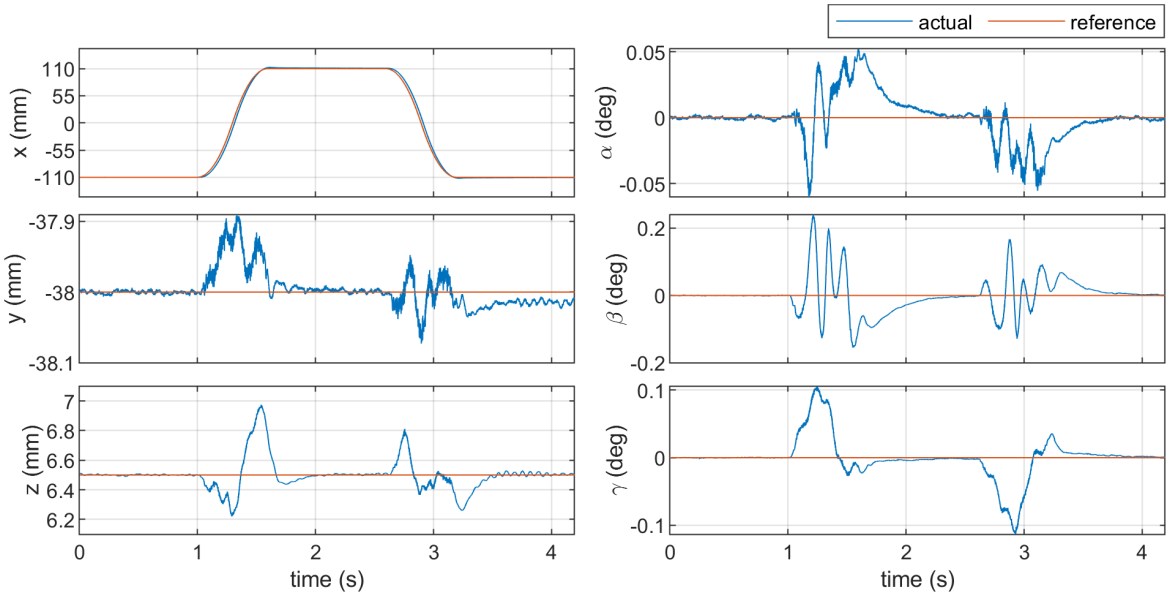

Figure 7.3: X-ramp at 700 mm/s peak on the 64 coils with the state estimator.

Since the levitation gap is better maintained with the state estimator, it is possible to achieve higher speeds of motion. Figure 7.3 shows an x ramp at a peak of 700 mm/s on the 64 coils using the state estimator. At this higher speed, the fluctuations in the z axis are still between 6.2 mm to 7.0 mm, and the fluctuations in other axes are of similar magnitude to the 500 mm/s test as well. However, the peak speed of 700 mm/s is only reached for about the middle 24 mm of the ramp before it starts to decelerate, since the reference acceleration is set at 2500 mm/s, the same as the other tests, and there is a limited range of motion. Increasing the acceleration reduces the stability, so higher speeds were tested on the larger MagFloor where there is more room to work with.

On the MagFloor, adding the state estimator shows a similar improvement in the fluctuations in the z axis, as shown in figure 7.4. The fluctuation in z is reduced from between 4.85 mm to 7.88 mm without the estimator to between 5.95 mm to 7.30 mm with the estimator, which is an increase in the lower bound by more than 1 mm. The fluctuations in β are reduced from between $-0.46°$ to $0.34°$ without the estimator to between $\pm 0.3°$ with the estimator. The fluctuations in the other rotation axes also show improvement with the estimator. With the state estimator, the mean absolute error during constant speed motion is 0.324 mm in the x ramps and 0.361 mm in the y ramps, which is similar to the 0.326 mm in x and 0.297 mm in y without the estimator. As larger integrator gains are used on the MagFloor, there is less effect on the tracking error by adding the estimator.

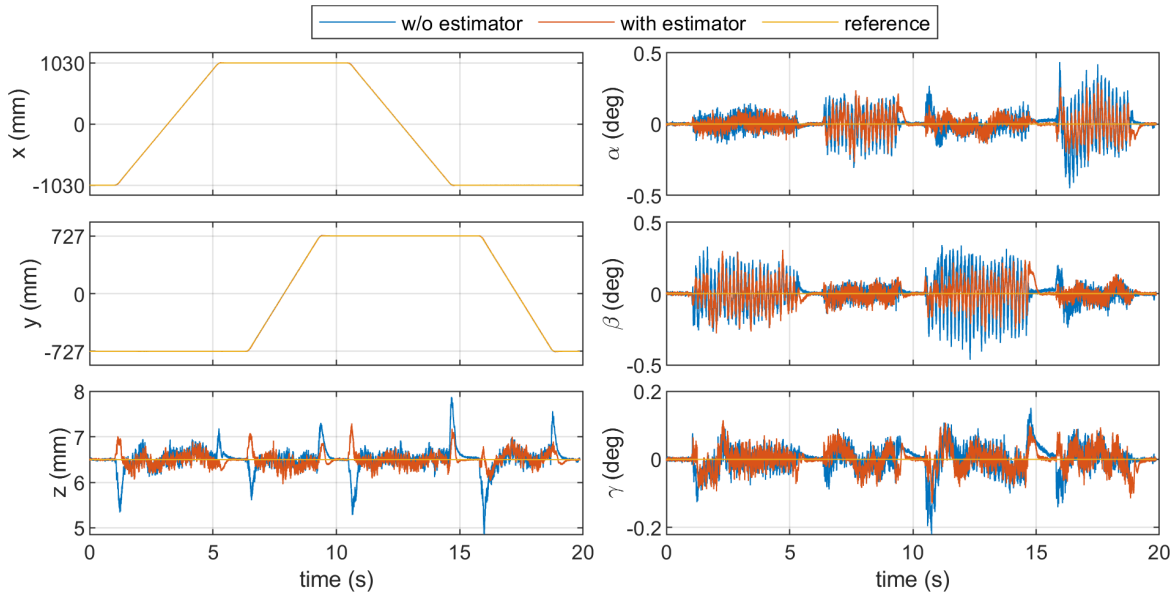

Figure 7.4: Rectangle at 500 mm/s on the MagFloor with and without the state estimator.

The maximum speed of motion doubled to 1000 mm/s on the MagFloor when using the state estimator, as shown in the rectangle motion in figure 7.5. At this higher speed, the fluctuations are within ±1.0 mm in z, ±0.35° in α, ±0.33° in β, and ±0.23° in γ. The minimum z height is higher at this 1000 mm/s with the estimator than at 500 mm/s without the estimator. Considering the regions of constant speed motion, the mean absolute tracking error is 0.985 mm in the x ramps and 1.214 mm in the y ramps. Attempting to move at speeds higher than 1000 mm/s can result in the power supply tripping from over 40 A of current being drawn in some instances. This is because there is significant eddy-current damping at this high speed, which requires large force and coil currents to overcome.

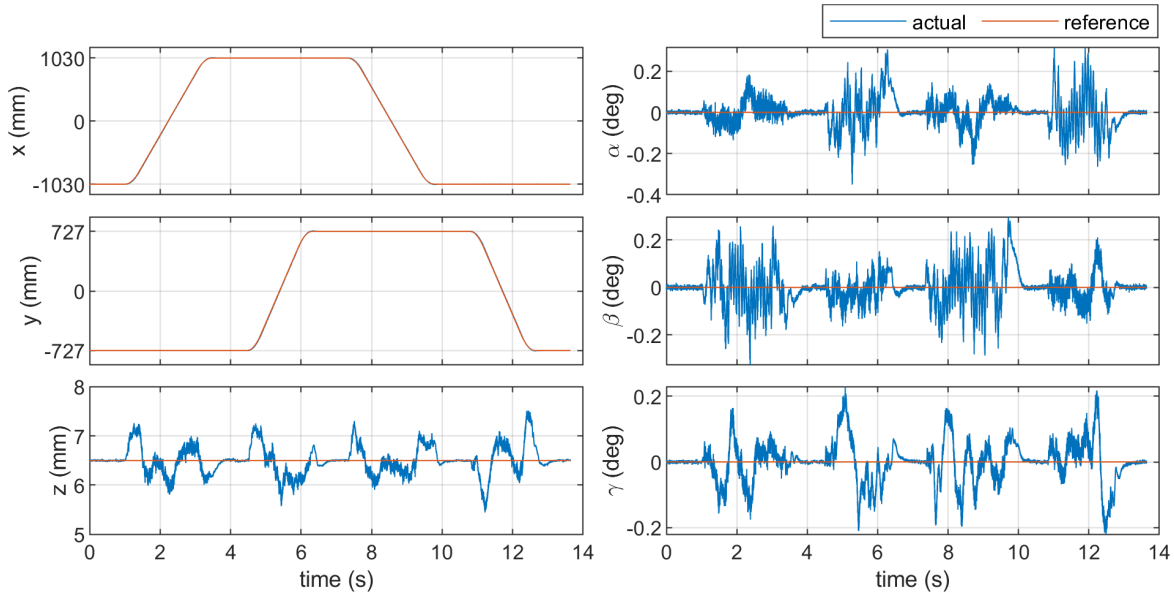

Figure 7.5: Rectangle at 1000 mm/s on the MagFloor with the state estimator.

Adding the state estimator significantly increased the maximum speed of rotation in the yaw (γ) axis from 75 °/s to 360 °/s, as shown in figure 7.6. An acceleration of 500 °/s^2 is used for a smooth start and end to the ramp and two revolutions (720°) are completed in each direction. During this motion, the fluctuations are between ±0.8 mm in x, −0.8 mm to 1.1 mm in y, 4.5 mm to 7.0 mm in z, −0.5° to 0.4° in α, and ±0.4° in β. The mean absolute tracking error during constant speed rotation in γ is 0.408°. Rotating at this maximum speed is close to drawing the maximum power the system can support, and attempting to rotate faster can trip the power supplies. During some instances where the levitation height dips, many coils are saturated and the system is not able to provide the desired forces. However, the momentum of the mover rotates past these points.

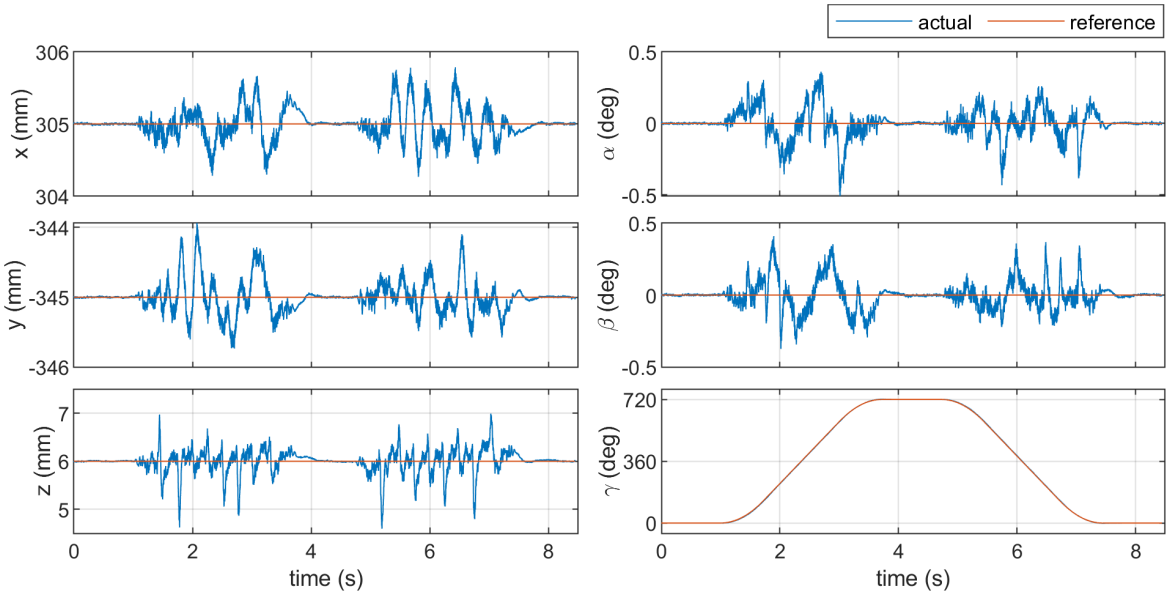

Figure 7.6: Yaw rotation at 360 °/s on the MagFloor with the state estimator.

Tracking of a circle at higher speeds on the MagFloor while using the state estimator is shown in figure 7.7. Similar to previous tests, the circle had a diameter of 994 mm and multiple loops of the trajectory were completed so that a middle loop where the mover is at an approximately constant tangential velocity is plotted. During this middle loop, the mean absolute error in xy is 1.228 mm, 2.419 mm and 5.290 mm for the 500 mm/s, 700 mm/s and 1000 mm/s speeds, respectively. The mean absolute error without the estimator at 500 mm/s was 0.767 mm, so the tracking error increased with the estimator, as expected.

Tracking of a figure-eight at the same maximum speeds is shown in figure 7.8. For this test, the mean absolute error in xy is 0.486 mm, 0.868 mm and 2.060 mm for the 500 mm/s, 700 mm/s and 1000 mm/s speeds, respectively. Tracking of a figure-eight is easier than a circle because the maximum speed only occurs at the middle of the path where the maximum speed in the x sine wave coincides with the maximum speed in the y sine wave. During most of the trajectory, the tangential velocity is lower. As expected, the mean absolute error in xy increased with the estimator at 500 mm/s, since without the estimator, the mean absolute error was 0.387 mm.

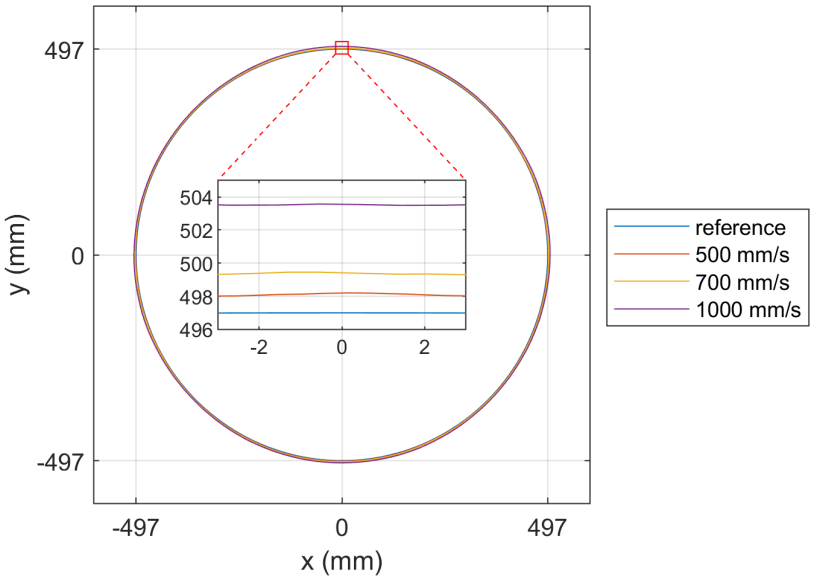

Figure 7.7: Circular trajectory at 500 mm/s, 700 mm/s and 1000 mm/s on the MagFloor with the state estimator.

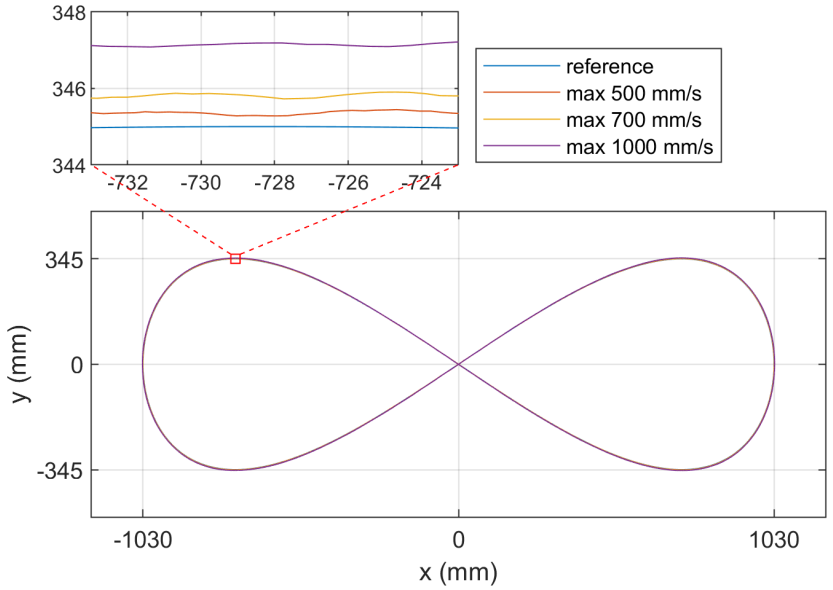

Figure 7.8: Figure-eight trajectory at 500 mm/s, 700 mm/s and 1000 mm/s on the MagFloor with the state estimator.

7.3 Iterative Learning Controller (ILC)

An iterative learning controller (ILC) is added on top of the state estimator controller to provide a feedforward control effort based on learning from past iterations of the same trajectory. With sufficient iterations, the tracking error should approximately go to 0, so long as the system is physically capable of tracking the path and actuator saturation is not an issue. ILC is sometimes implemented by modifying the reference position with each iteration, instead of adding a feedforward control effort. While this can work just as well, the learned modified reference will then be tied to certain PID gains and changing the gains would necessitate relearning the reference modification. For the ILC implementation in this research, the trajectory is stored in a file where each line corresponds to a time step and has six position targets and six feedforward control efforts to be loaded, one for each axis. The reference positions are only generated once for a given trajectory, and the feedforward control efforts are initialized to zero and then updated with each iteration.

The ILC effort is updated using a PD-type tunable learning function as

$$u_{i+1,t} = u_{i,t} + k_{lp}(r_{i,t} - x_{i,t+7}) + k_{ld}(\dot{r}_{i,t} - \dot{x}_{i,t+11}), \tag{7.3}$$

where i is the iteration index and t is the time step index. Since the state estimator implementation effectively tries to minimize the error between the position measurement and the reference from 7 time steps ago, the ILC implementation updates the ILC effort based on the error between the reference and the measurement from 7 time steps in the future, from the past iteration. Also, since the estimate of the derivative of the measurement passes through a discrete first-order low-pass filter with an effective time constant of 4 ms, another four time steps are added between the difference of the derivative of the reference and the measurement. In effect, this means that the control efforts from 7 ms and 11 ms ago are modified based on the position measurement and its derivative. Lastly, in the special case of the z axis on the MagFloor, the reference is compared to the corrected measurement using the coil height interpolation described in section 4.4.2.

For both the 64 coils and the MagFloor, the ILC learning gains were set to be approximately one-quarter of the PD gains used in the PID and are shown in table 7.1. Using pure P learning without any derivative component resulted in instability after several iterations. As such, adding learning from the derivative was necessary to ensure stability. This causes the measurement noise to be passed onto the learned feedforward control efforts, which can accumulate for many iterations. Therefore, because of the greater noise on the MagFloor, the learned ILC efforts were filtered using a frequency-based filter which removed all frequencies above a threshold of 10 Hz in the frequency domain before attempting the next iteration, as will be discussed later.

Table 7.1: PD learning gains used in ILC for the 64 coils and the MagFloor.

		x	y	z	α	β	γ
			N/m			N·m/rad	
k_{lp}	64 Coils Cameras	2500	2500	2750	45	45	50
	MagFloor Cameras	2250	2250	2750	45	45	55
			N·s/m			N·m·s/rad	
k_{ld}	64 Coils Cameras	87.5	87.5	81.25	1	1	1.5
	MagFloor Cameras	87.5	87.5	81.25	1.5	1.5	1.6

7.4 ILC Results

The response after using ILC on an x-ramp of 500 mm/s on the 64 coils is shown in figure 7.9. The first iteration is similar to simply using the state estimator as shown in figure 7.2 as the ILC feedforward control effort is initialized as all zeros. By the third iteration, the fluctuations in β reduced from between $-0.15°$ to $0.24°$ to between $-0.088°$ to $0.121°$. After 10 iterations, the fluctuations are between $-0.041°$ to $0.028°$ in β and between 6.42 mm to 6.60 mm in z, substantially reduced from the first iteration. The mean absolute error in x during constant speed motion of the x-ramp is 4.862 mm, 2.153 mm and 0.397 mm after the first, third, and tenth iteration. The third iteration has similar errors to the response without the state estimator shown in figure 6.16.

Figure 7.10 shows the progression of the mean absolute error in each axis during training considering the entire x-ramp trajectory. The error in the z axis increases for the first few iterations since the position of the mover changes between iterations as the mover tracks the ramp more closely, resulting in a new set of errors in z that may not correspond to what was learned previously. After about the sixth iteration, the mean absolute error in the x axis starts to plateau. The error in the rotation axes shows a decline up to the tenth iteration, which indicates more iterations are needed to fully converge.

The response after using ILC on a circular trajectory of 300 mm/s on the 64 coils is shown in figure 7.11. Similar to other tests, three loops of the circle were performed and a middle loop is plotted. The mean absolute error in the xy position during a middle loop is 2.991 mm, 1.226 mm and 0.400 mm after the first, third, and tenth iteration. The third iteration has a similar tracking error to the circular trajectory at 300 mm/s without the state estimator shown in figure 6.19, and there is a significant improvement by the tenth iteration. As can be seen in figure 7.11, the trajectory of the tenth iteration closely follows the reference to produce the correct diameter of the circle.

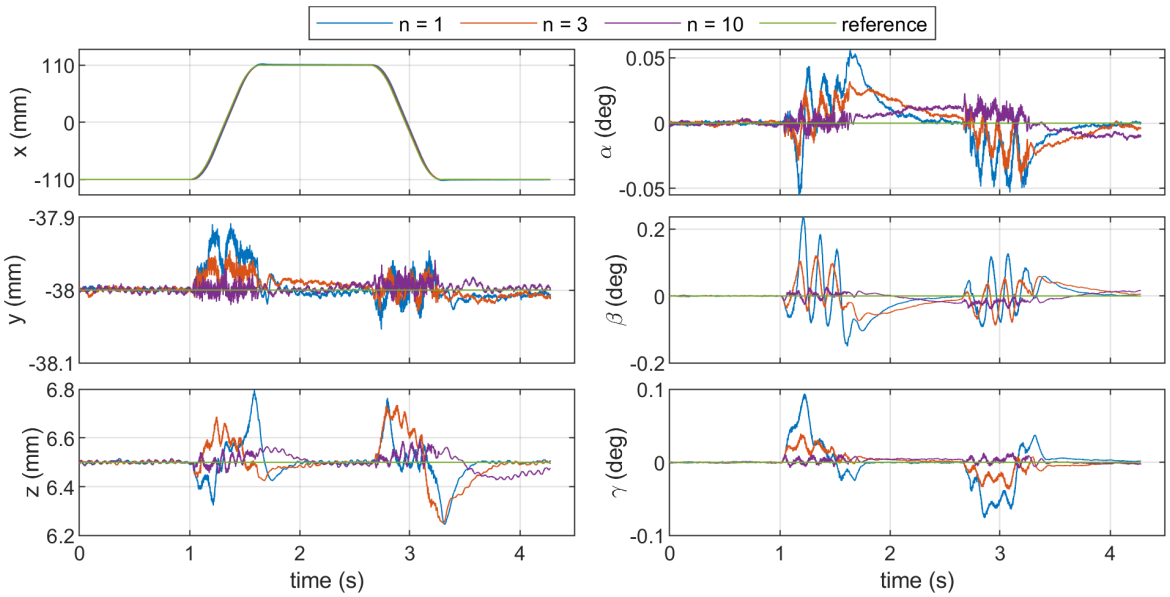

Figure 7.9: X-ramp at 500 mm/s on the 64 coils after 1, 3, and 10 iterations using ILC.

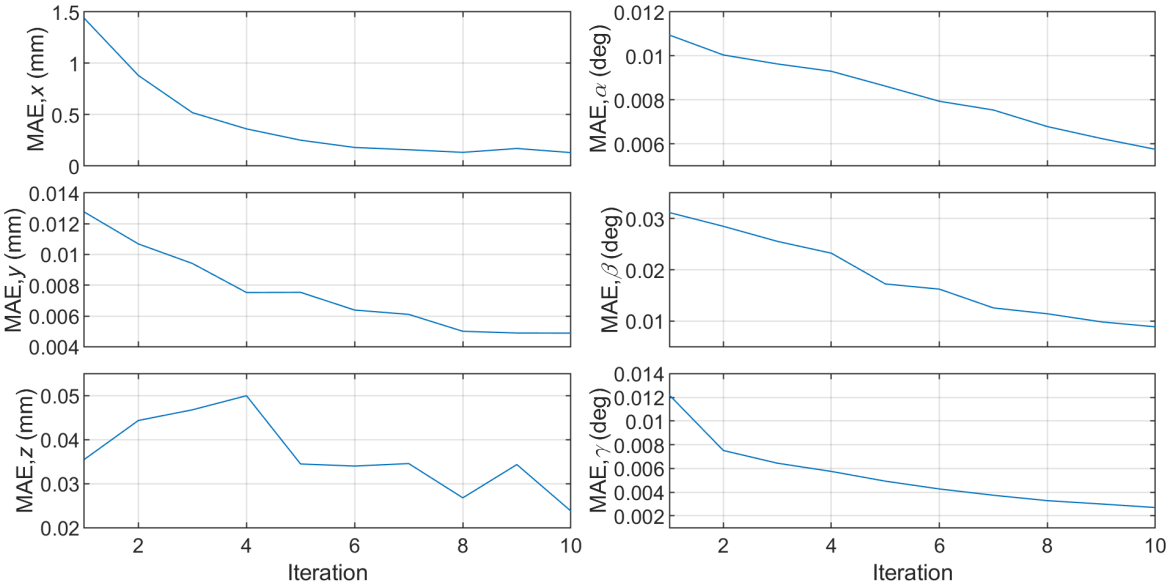

Figure 7.10: Mean absolute error per iteration during ILC on an x-ramp on the 64 coils.

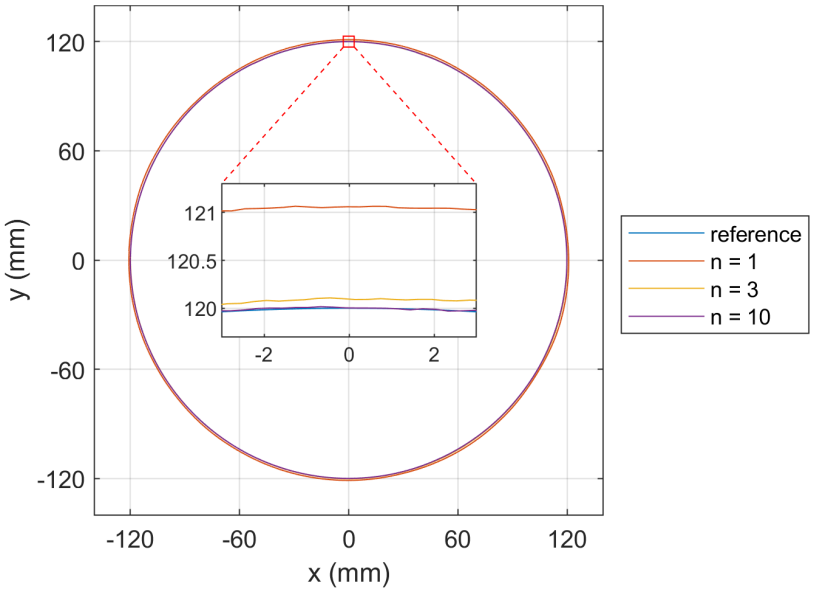

Figure 7.11: Circular trajectory at 300 mm/s with a diameter of 240 mm on the 64 coils after 1, 3, and 10 iterations using ILC.

As there is much greater measurement noise on the MagFloor, a frequency-based filter is added after learning the ILC efforts so that the noise is not accumulated with consecutive iterations. During each iteration, the ILC efforts for the next iteration are learned using equation (7.3). After the trajectory is complete, the entire time-based signal of feedforward ILC efforts is converted into the frequency domain using the fast Fourier transform (FFT) algorithm in MATLAB, which computes the discrete Fourier transform (DFT) of the signal. The frequency domain signal is then filtered by setting the amplitudes of all frequencies above a threshold of 10 Hz to zero, and this result is then reconstructed in the time domain using the inverse transform (IFFT). The result of this filtering on the ILC effort in x after the first iteration of an x-ramp is shown in figure 7.12. Note that the y-axis of the frequency domain plot is logarithmic, so the higher frequencies are much smaller in amplitude than the lower frequencies. The cutoff frequency of 10 Hz was chosen as it was sufficient to reproduce the large peaks in the signal while filtering out most of the noise.

The response after using ILC on an x-ramp of 500 mm/s on the MagFloor is shown in figure 7.13. This speed was chosen as it is well below the maximum 1000 mm/s which is close to saturating the coils and power supplies. At 500 mm/s, there is greater room to increase the control efforts when required to better track the trajectory. On the first iteration, the fluctuations are between 6.02 mm to 7.05 mm in z and $\pm 0.28°$ in β. By the

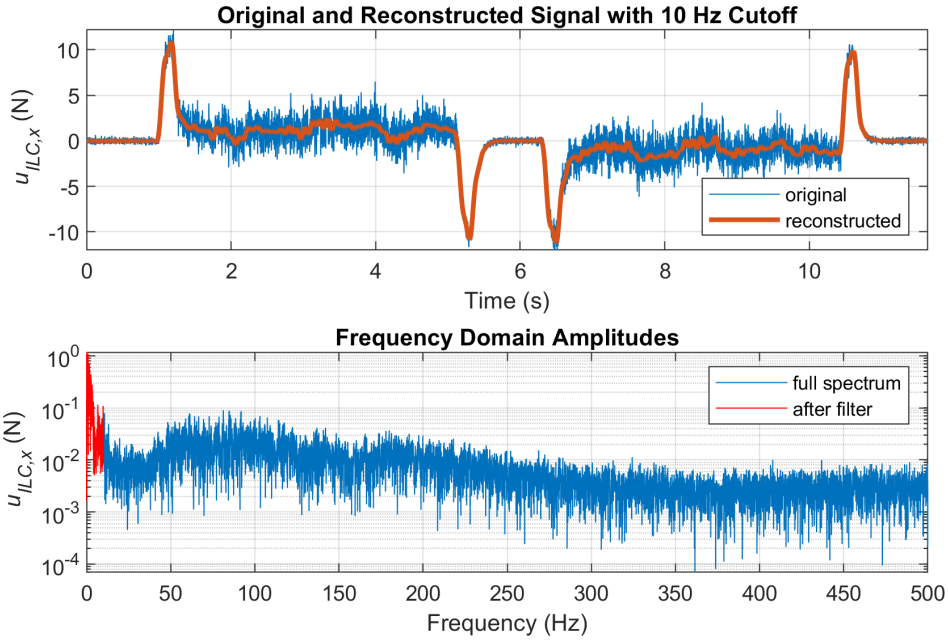

Figure 7.12: Frequency-based filtering of the ILC effort during an x-ramp at 500 mm/s after one iteration.

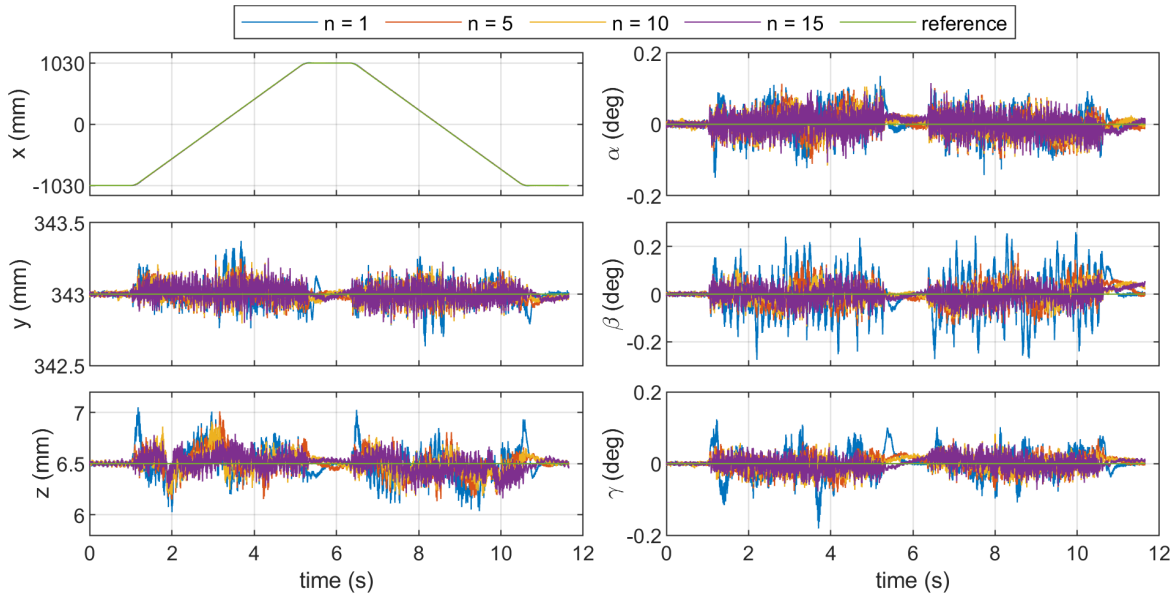

Figure 7.13: X-ramp from −1030 mm to 1030 mm at 500 mm/s on the MagFloor after 1, 5, 10, and 15 iterations using ILC.

fifteenth iteration, the fluctuations are reduced to between 6.16 mm to 6.79 mm in z and $\pm 0.13°$ in β. The fluctuations in the other axes are also reduced. The mean absolute error in x during constant speed motion is 0.317 mm, 0.320 mm, 0.274 mm and 0.251 mm for the first, fifth, tenth, and fifteenth iteration, respectively.

Figure 7.14 shows the progression of the mean absolute error in each axis during training on the x-ramp. Note that this error includes the entire trajectory, not just the regions of constant speed. As can be seen, the mean absolute error trends downward with each iteration, though it is not a monotonic decline. The error increases noticeably in the y axis in the seventh iteration but then declines in subsequent iterations. Overall, the error is higher on the MagFloor than on the 64 coils, even after fifteen iterations. The primary reason for this is likely the greater measurement noise and less accurate position readings causing more fluctuations in each axis. Another factor is that the trajectory is much longer on the MagFloor and errors may not be as repeatable.

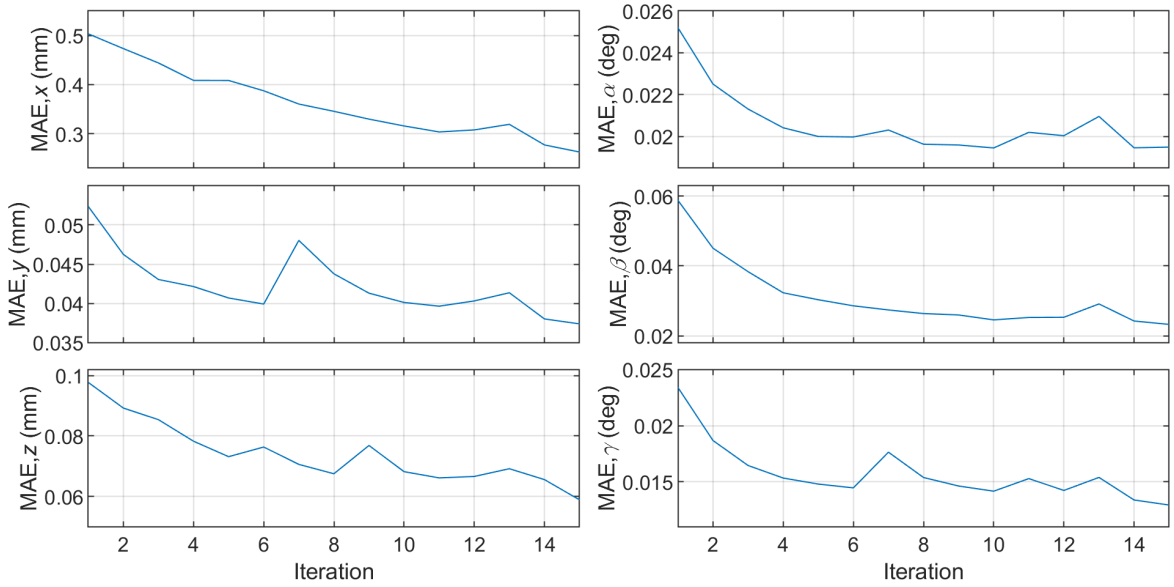

Figure 7.14: Mean absolute error per iteration during ILC on an x-ramp on the MagFloor.

The response from using ILC during a circular trajectory at 500 mm/s on the MagFloor is shown in figure 7.15. The mean absolute error in xy during a middle loop is 1.243 mm, 1.066 mm, 0.934 mm and 0.782 mm for the first, fifth, tenth, and fifteenth iteration, respectively. Note that the mean absolute error during the 500 mm/s circle without the state estimator was 0.767 mm as shown in figure 6.20, which is still less than the fifteenth iteration with the ILC. As can be seen in the figure, the fifteenth iteration still has not

quite reached the reference at the top of the loop, so more iterations could be required to fully converge. To reduce the required number of iterations, greater learning gains could be tried. However, increasing the learning gains also increases the risk of instability, so further tuning would be required.

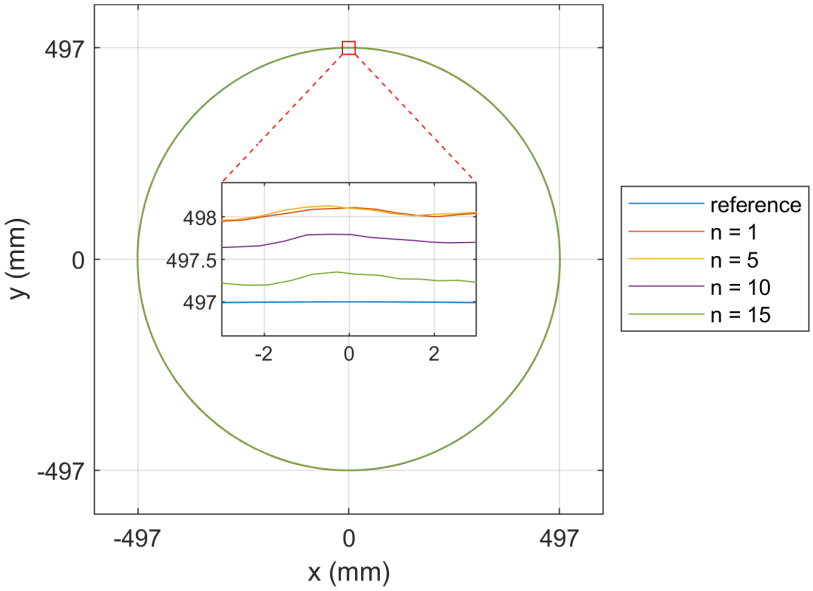

Figure 7.15: Circular trajectory at 500 mm/s with a diameter of 994 mm on the MagFloor after 1, 5, 10, and 15 iterations using ILC.

Chapter 8

Conclusions and Future Work

This research demonstrates the successful implementation of a modular maglev planar motor using a square coil stator and a 2-D Halbach array mover designed and built by a team of graduate students at the Maglev Microrobotics Laboratory. First, the internal PI controllers in the current amplifiers were tuned and tested to determine their response time and bandwidth. Then, a PID controller to control the six degrees of freedom of the mover was designed, with the system integration completed in TwinCAT. The six PIDs were first tuned on the 64 coils using the camera system. Levitation was achieved using both a camera-based motion tracking system and a set of eight laser displacement sensors on a 64-coil prototype and the performance between them was compared. Large-scale and high-speed motion was successfully demonstrated on the 768-coil MagFloor in RoboHub using camera-based feedback. Finally, the trajectory tracking performance was improved through the implementation of a state estimator to compensate for the system latency and an iterative learning controller (ILC).

8.1 Controller Design and System Integration

After tuning the internal PI controllers in the current amplifiers, the rise time is found to be about 0.2 ms for small current changes. The bandwidth decreases for sinusoidal inputs with amplitudes above 1 A as this passes above the voltage saturation at high frequencies. The most limiting factor to the current amplifier performance is the EtherCAT communication delay of 1.5 ms between sending current targets and receiving the updated current feedback when using the maximum EtherCAT communication cycle of 2000 Hz. For the small current changes during smooth motions, it can be expected that the current amplifiers reach their new target before the next target is received.

The PID control loop designed in MATLAB/Simulink and integrated into TwinCAT is able to effectively control the six DOF of the mover. The custom derivative calculation effectively removes derivative spikes from sensor sync issues and derivative kick and reduces the derivative noise through the low-pass filter. Similar PID parameters are used for each

of the three setups: the 64 coils with laser sensors, the 64 coils with laser sensors, and the MagFloor with cameras. Since the laser sensors have less measurement noise, the gains are increased slightly in the $\alpha\beta$ rotation axes to improve the performance. On the MagFloor, the integrator gains in xy are increased substantially to better track ramp motions for the large trajectories. Since six DOF levitation is achieved with the laser sensors, the method for converting the linear displacement readings into the 6-D position and orientation of the mover is demonstrated to be effective. The visualization interface developed in TwinCAT is also effective for controlling the system and testing the various trajectories used throughout this research.

8.2 Levitation Performance Comparison

As expected, the laser displacement sensors showed the best levitation precision of the three setups, with a precision of about 0.005 mm in the xyz translation directions and 0.002° in the $\alpha\beta\gamma$ rotations, using the $\pm 3\sigma$ interval. Interestingly, the precision in the z axis was not significantly better than the horizontal axes despite the much more precise laser sensors used on the vertical axes. This indicates that the precision of the vertical sensors is no longer limiting, and other factors such as the 500 Hz frequency of the measurement communication may be more important for further improvement. The system latency when using the laser sensors was also less than that with the cameras and was measured to be about 6 ms with the laser sensors and 7 ms with the cameras for small steps.

When using the cameras on the 64 coils, the precision is 0.008 mm in xy, 0.011 mm in z, 0.003° in $\alpha\beta$, and 0.002° in γ. On the MagFloor, the precision is reduced to 0.03 mm in xyz, 0.015° in $\alpha\beta$, and 0.01° in γ. Using the cameras on the 64-coil prototype was about half as precise in the z axis as the laser sensors, and the precision was about three times less precise than that on the MagFloor with the same four cameras further away. The precision was about five times less precise in the $\alpha\beta$ rotation axes with the cameras on the MagFloor than on the 64 coils, so adding more cameras closer to the ground around the MagFloor could offer significant improvement. Despite the much larger measurement noise on the MagFloor, levitation was still possible. By adding more cameras, similar precision could be achieved on the MagFloor as was on the 64 coils.

Despite the better precision with the laser sensors, the step responses were very similar to using the cameras on the 64 coils, and in the case of the x-step, the performance was better with the cameras. For a step in the x-axis with the cameras on the 64 coils, the rise time is 0.045 s, the 2 % settling time is 0.088 s, and the overshoot is 0.275 %. Two explanations for this are that the extra weight of the flat plates on the mover when using

the laser sensors slowed it down for the same gains and because the communication with the laser sensors is only at 500 Hz whereas the cameras send feedback at 1000 Hz. As expected, the step responses showed greater overshoot and longer settling times on the MagFloor since there is a much greater steady-state error and some of the integrator gains were increased to compensate. For an 8 mm step in x on the MagFloor, the 2 % settling time is 0.578 s and the overshoot is 14.0 %. Because of the higher integrator gains on the MagFloor, the system was better able to track a ramp motion and the mean absolute error in x was just 0.326 mm during the constant speed region of an x-ramp at the maximum speed of 500 mm/s. Full yaw (γ) rotation was also demonstrated on the MagFloor by completing a 360° rotation at a speed of 75 °/s.

8.3 Improvements with Advanced Methods

The levitation performance was improved with the addition of a state estimator to offset the 7 ms total system latency when using the camera system. In particular, the maximum speed was able to increase from 500 mm/s to 1000 mm/s on the MagFloor, and the fluctuations in the levitation gap and rotations were even less at the higher speed with the estimator. The maximum speed of yaw rotation was able to significantly increase from 75 °/s to 360 °/s using the state estimator as the stability of the levitation was better maintained. However, adding the state estimator reduced the tracking performance in the horizontal xy axes as the force error from the delay in these axes is always in the direction of motion, which helps to offset the eddy-current damping from the aluminum cover sheet. By adding the state estimator, there is less force in the direction of motion and the position error increases to overcome the damping force.

Implementing ILC on top of the state estimator improved the tracking performance with successive iterations of the same trajectory. On the 64-coil prototype, the mean absolute error in x during the constant speed region of an x-ramp at 500 mm/s decreased from 4.862 mm to 0.397 mm from the first to tenth iteration, resulting in a similar performance to using the much greater integrator gains on the MagFloor without the state estimator. The fluctuations in the β rotation were also reduced by over five times through the ten iterations. Using ILC on the MagFloor also resulted in improved xy tracking performance and reduced fluctuations in the levitation gap and rotation axes. However, the improvement of ILC was less significant in reducing the fluctuations in the other axes due to the greater measurement noise and larger steady-state error.

Overall, this demonstrates great potential for a planar maglev system which can achieve both high precision motion and be expanded like the MagFloor for large-range applications.

The use of a camera-based motion tracking system enables easy expansion and accommodation to stator configurations, and higher precision sensors such as laser sensors could be used in specific locations to provide even more precise control where needed. Force and torque errors caused by the system delay can be compensated by using a state estimator and the overall system performance can be improved through learning-based techniques such as an iterative learning controller.

8.4 Future Work

To fully realize a planar maglev system which can be used in conveying or flexible manufacturing applications, there are several areas of improvement or future work which could be investigated. Some of these are mentioned below:

- The laser sensor apparatus is a significant obstruction above the mover to any work process or payload. For more practical purposes, the vertical sensors could be positioned below the coils to look through slots in the aluminum cover sheet and the sensor frame above the mover could be removed. The laser sensors on the sides can be mounted from the sides to avoid any obstruction. Also, the vertical laser sensors could be placed farther apart to improve the measurement of the $\alpha\beta$ rotation axes. Alternatively, other sensors could be investigated, such as Hall effect sensors.

- To increase the robustness of the system, the quality of the position measurement on the MagFloor should be improved. The precision of the camera-based motion tracking system on the MagFloor could be substantially improved by adding more cameras, repositioning the cameras, and perhaps increasing the size of the reflective markers on the mover.

- Adding a payload to the mover was outside the scope of this work, however, it is an essential step toward practical applications. Measurements of the maximum payload should be performed, and the performance measured while carrying a payload. It is possible that redesigning the magnet array could increase the maximum payload and some form of adaptive control may be necessary.

- Once transporting a payload has been achieved, the next step could be a collaboration with robotic arms for loading and unloading the payload. This would involve integration with other robotic systems and perhaps some trajectory planning and optimization. If using camera-based sensor systems, either the payload or the robotic

arm could interfere with the position measurement. Secondary sensing systems could be implemented in specific locations with sensor fusion to allow for obstructions while maintaining levitation.

- For large payloads or more complex tasks, multiple movers could interact and collaborate. Mover-to-mover interactions would need to be studied as the magnetic fields can interact. There is likely a minimum distance required between the magnets such that the coils can still pull them apart. Also, a method will need to be developed for how to assign coil currents when the active coil sets of multiple movers overlap.

- To increase the payload and the maximum speed, the aluminum cover sheet can be removed or made thinner. The damping force would significantly decrease if the aluminum sheet were removed, allowing for a greater maximum speed, but the system would be less stable, so a good controller is needed. Removing the cover sheet would also allow the mover to levitate lower and closer to the coils where more force can be provided, thus raising the maximum payload and reducing energy consumption.

- As mentioned, the aluminum cover sheet provides significant eddy-current damping at high speeds and a more complex controller could model this damping force to improve the performance. With a correctly predicted damping force based on the mover's speed and levitation height, the integrator would need to do much less work and there would be much less overshoot at the end of the ramp motions.

- A very basic ILC strategy was investigated in this research, and it can be improved with more tuning or advanced techniques. The cutoff frequency of 10 Hz for the FFT filter on the MagFloor's ILC implementation should be further tuned, along with the ILC learning parameters. However, ILC is only one learning-based method and newer techniques show strong potential. For instance, a neural network was proposed to predict the reference modification instead of using time-consuming iterations of a trajectory [68]. This idea of using machine learning to improve control can be expanded upon.

References

[1] L. Yan, "Development and Application of the Maglev Transportation System," *IEEE Transactions on Applied Superconductivity*, vol. 18, no. 2, pp. 92–99, 6 2008.

[2] A. Smirnov, N. Uzhegov, T. Sillanpää, J. Pyrhönen, and O. Pyrhönen, "High-Speed Electrical Machine with Active Magnetic Bearing System Optimization," *IEEE Transactions on Industrial Electronics*, vol. 64, no. 12, pp. 9876–9885, 12 2017.

[3] C. Ha, C. Kim, and J. Lim, "Experimental Verification of a Magnetic Levitation Transport System for the OLED Display Evaporation Process Under Vacuum," *IEEE Robotics and Automation Letters*, vol. 3, no. 4, pp. 2786–2791, 2018.

[4] J. Kim, G. B. King, C. H. Kim, and C. W. Ha, "Modeling and designing levitation, roll and pitch controller for high accuracy maglev tray system," *Mechatronics*, vol. 53, pp. 181–191, 8 2018.

[5] K. H. Park, S. K. Lee, J. H. Yi, S. H. Kim, Y. K. Kwak, and I. A. Wang, "Contactless magnetically levitated silicon wafer transport system," *Mechatronics*, vol. 6, no. 5, pp. 591–610, 8 1996.

[6] H. Zhou, H. Deng, and J. Duan, "Hybrid Fuzzy Decoupling Control for a Precision Maglev Motion System," *IEEE/ASME Transactions on Mechatronics*, vol. 23, no. 1, pp. 389–401, 2018.

[7] W. J. Kim and D. L. Trumper, "High-precision magnetic levitation stage for photolithography," *Precision Engineering*, vol. 22, no. 2, pp. 66–77, 4 1998.

[8] J. J. Abbott, E. Diller, and A. J. Petruska, "Magnetic Methods in Robotics," *Annual Review of Control, Robotics, and Autonomous Systems*, vol. 3, no. 1, pp. 57–90, 5 2020.

[9] M. P. Kummer, J. J. Abbott, B. E. Kratochvil, R. Borer, A. Sengul, and B. J. Nelson, "OctoMag: An Electromagnetic System for 5-DOF Wireless Micromanipulation," *IEEE Transactions on Robotics*, vol. 26, no. 6, pp. 1006–1017, 12 2010.

[10] P. K. Heris and M. B. Khamesee, "Design and Fabrication of a Magnetic Actuator for Torque and Force Control Estimated by the ANN/SA Algorithm," *Micromachines*, vol. 13, no. 2, 2022.

[11] M. Dyck, X. Lu, and Y. Altintas, "Magnetically Levitated Rotary Table With Six Degrees of Freedom," *IEEE/ASME Transactions on Mechatronics*, vol. 22, no. 1, pp. 530–540, 2 2017.

[12] X. Lu, T. Zheng, F. Xu, and X. Xu, "Semi-Analytical Solution of Magnetic Force and Torque for a Novel Magnetically Levitated Actuator in Rotary Table," *IEEE Transactions on Magnetics*, vol. 55, no. 12, pp. 1–8, 12 2019.

[13] P. Kumar, S. Malik, E. Toyserkani, and M. B. Khamesee, "Development of an Electromagnetic Micromanipulator Levitation System for Metal Additive Manufacturing Applications," *Micromachines*, vol. 13, no. 4, 2022.

[14] N. Arora, M. U. Khan, L. Petit, F. Lamarque, and C. Prelle, "Design and Development of a Planar Electromagnetic Conveyor for the Microfactory," *IEEE/ASME Transactions on Mechatronics*, vol. 24, no. 4, pp. 1723–1731, 2019.

[15] A. Jain, P. K. Jain, F. T. S. Chan, and S. Singh, "A review on manufacturing flexibility," *International Journal of Production Research*, vol. 51, no. 19, pp. 5946–5970, 2013.

[16] A. K. Sethi and S. P. Sethi, "Flexibility in manufacturing: A survey," *International journal of flexible manufacturing systems*, vol. 2, no. 4, pp. 289–328, 1990.

[17] L. L. Koste, M. K. Malhotra, and S. Sharma, "Measuring dimensions of manufacturing flexibility," *Journal of Operations Management*, vol. 22, no. 2, pp. 171–196, 2004.

[18] J. Browne, D. Dubois, K. Rathmill, S. P. Sethi, and K. E. Stecke, "Classification of Flexible Manufacturing Systems," *The FMS Magazine*, vol. 2, pp. 114 – 117, 10 1984.

[19] M. Lütjen, M. Teucke, M. Isenberg, H. Thamer, C. Uriarte, and S. Kunaschk, "Design of SmartGate Technologies for Enhanced Material Handling," *International Journal of Advanced Logistics*, vol. 2, no. 1, pp. 26–37, 2013.

[20] C. Uriarte, A. Asphandiar, H. Thamer, A. Benggolo, and M. Freitag, "Control strategies for small-scaled conveyor modules enabling highly flexible material flow systems," *Procedia CIRP*, vol. 79, pp. 433–438, 2019.

[21] Cellumation, "Cellumation | Innovative conveyor technology," 2022. [Online]. Available: https://cellumation.com/

[22] Omnia Wheel, "Conveyor Transfer Systems and Omniwheel Conveyors," 2022. [Online]. Available: https://www.omniawheel.com/conveyor-systems

[23] Fetch Robotics Inc., "Autonomous Warehouse Robots that Improve Productivity from Fetch Robotics," 2022. [Online]. Available: https://fetchrobotics.com/

[24] Planar Motor Inc., "Products: XBot," 2022. [Online]. Available: https://www.planarmotor.com/products.html

[25] Beckhoff Automation Ltd., "XPlanar | Planar motor system," 2022. [Online]. Available: https://www.beckhoff.com/en-ca/products/motion/xplanar-planar-motor-system/

[26] Z. Xu, X. Zhang, and M. B. Khamesee, "Real-Time Data-Driven Force and Torque Modeling on a 2-D Halbach Array by a Symmetric Coil Considering End Effect," *IEEE Transactions on Magnetics*, vol. 58, no. 11, pp. 1–10, 11 2022.

[27] Y. Ueda and H. Ohsaki, "A Planar Actuator with a Small Mover Traveling Over Large Yaw and Translational Displacements," *IEEE Transactions on Magnetics*, vol. 44, no. 5, pp. 609–616, 5 2008.

[28] L. Zhang, B. Kou, H. Zhang, and S. Guo, "Characteristic Analysis of a Long-Stroke Synchronous Permanent Magnet Planar Motor," *IEEE Transactions on Magnetics*, vol. 48, no. 11, pp. 4658–4661, 11 2012.

[29] S. Zhang, Y. Zhu, H. Mu, K. Yang, and W. Yin, "Decoupling and levitation control of a six-degree-of-freedom magnetically levitated stage with moving coils based on commutation of coil array," *Proceedings of the Institution of Mechanical Engineers, Part I: Journal of Systems and Control Engineering*, vol. 226, no. 7, pp. 875–886, 6 2012.

[30] C. P. Britcher and M. Ghofrani, "A magnetic suspension system with a large angular range," *Review of Scientific Instruments*, vol. 64, no. 7, pp. 1910–1917, 1993.

[31] H. Zhu, C. K. Pang, and T. J. Teo, "Analysis and control of a 6 DOF maglev positioning system with characteristics of end-effects and eddy current damping," *Mechatronics*, vol. 47, pp. 183–194, 11 2017.

[32] H. Zhu, T. J. Teo, and C. K. Pang, "Magnetically Levitated Parallel Actuated Dual-Stage (Maglev-PAD) System for Six-Axis Precision Positioning," *IEEE/ASME Transactions on Mechatronics*, vol. 24, no. 4, pp. 1829–1838, 8 2019.

[33] J. W. Jansen, "Magnetically levitated planar actuator with moving magnets : electromechanical analysis and design," Ph.D. dissertation, Electrical Engineering, 2007.

[34] J. W. Jansen, C. M. M. van Lierop, E. A. Lomonova, and A. J. A. Vandenput, "Magnetically Levitated Planar Actuator With Moving Magnets," *IEEE Transactions on Industry Applications*, vol. 44, no. 4, pp. 1108–1115, 7 2008.

[35] J. M. M. Rovers, J. W. Jansen, and E. A. Lomonova, "Design and measurements of the Double Layer Planar Motor," in *2013 International Electric Machines Drives Conference*, 5 2013, pp. 204–211.

[36] ——, "Performance measurements of the Double Layer Planar Motor," in *Proceedings of the 10th International Symposium on Linear Drives for Industry Applications (LDIA 2015), 27-29 July 2015, Aachen, Germany.* s.n., 2015.

[37] I. Proimadis, C. H. H. M. Custers, R. Tóth, J. W. Jansen, H. Butler, E. Lomonova, and P. M. J. V. d. Hof, "Active Deformation Control for a Magnetically Levitated Planar Motor Mover," *IEEE Transactions on Industry Applications*, vol. 58, no. 1, pp. 242–249, 1 2022.

[38] X. Lu and I.-u.-r. Usman, "6D direct-drive technology for planar motion stages," *CIRP Annals*, vol. 61, no. 1, pp. 359–362, 2012.

[39] I.-U.-R. Usman and X. Lu, "Force Ripple Attenuation of 6-DOF Direct Drive Permanent Magnet Planar Levitating Synchronous Motors," *IEEE Transactions on Magnetics*, vol. 51, no. 12, pp. 1–8, 12 2015.

[40] J. d. Boeij, E. Lomonova, and J. Duarte, "Contactless Planar Actuator With Manipulator: A Motion System Without Cables and Physical Contact Between the Mover and the Fixed World," *IEEE Transactions on Industry Applications*, vol. 45, no. 6, pp. 1930–1938, 2009.

[41] F. Liu, M. Zhang, Y. Zhu, and C. Hu, "A Real-Time Model of Ironless Planar Motors With Stationary Circular Coils," *IEEE Transactions on Magnetics*, vol. 51, no. 7, pp. 1–10, 2015.

[42] X. Zhang, C. Trakarnchaiyo, H. Zhang, and M. B. Khamesee, "MagTable: A tabletop system for 6-DOF large range and completely contactless operation using magnetic levitation," *Mechatronics*, vol. 77, p. 102600, 8 2021.

[43] P. Berkelman and M. Dzadovsky, "Magnetic Levitation Over Large Translation and Rotation Ranges in All Directions," *IEEE/ASME Transactions on Mechatronics*, vol. 18, no. 1, pp. 44–52, 2 2013.

[44] H. Zhu, T. J. Teo, and C. K. Pang, "Design and Modeling of a Six-Degree-of-Freedom Magnetically Levitated Positioner Using Square Coils and 1-D Halbach Arrays," *IEEE Transactions on Industrial Electronics*, vol. 64, no. 1, pp. 440–450, 2017.

[45] Stanford Magnets, "Everything You Need to Know About Halbach Arrays," 2022. [Online]. Available: https://www.stanfordmagnets.com/everything-you-need-to-know-about-halbach-arrays.html

[46] M. Miyasaka and P. Berkelman, "Magnetic levitation with unlimited omnidirectional rotation range," *Mechatronics*, vol. 24, no. 3, pp. 252–264, 4 2014.

[47] H. Zhu, T. J. Teo, and C. K. Pang, "Flexure-Based Magnetically Levitated Dual-Stage System for High-Bandwidth Positioning," *IEEE Transactions on Industrial Informatics*, vol. 15, no. 8, pp. 4665–4675, 8 2019.

[48] W. Min, M. Zhang, Y. Zhu, B. Chen, G. Duan, J. Hu, and W. Yin, "Analysis and Optimization of a New 2-D Magnet Array for Planar Motor," *IEEE Transactions on Magnetics*, vol. 46, no. 5, pp. 1167–1171, 5 2010.

[49] Y. Wang, F. Chen, Z. Zheng, and L. Zeng, "Magnet array of planar motor using permanent magnets with different magnetisation intensity and height," *IET Electric Power Applications*, vol. 14, no. 14, pp. 2772–2779, 2020.

[50] J. d. Boeij, E. Lomonova, and A. Vandenput, "Modeling Ironless Permanent-Magnet Planar Actuator Structures," *IEEE Transactions on Magnetics*, vol. 42, no. 8, pp. 2009–2016, 8 2006.

[51] F. Bancel, "Magnetic nodes," *Journal of Physics D: Applied Physics*, vol. 32, no. 17, pp. 2155–2161, 1999.

[52] J. d. Boeij, E. Lomonova, and A. J. A. Vandenput, "Look-Up Table Based Real-Time Commutation of 6-DOF Planar Actuators," in *2007 IEEE International Conference on Control Applications*, 10 2007, pp. 1118–1123.

[53] J. W. Jansen, C. M. M. van Lierop, E. A. Lomonova, and A. J. A. Vandenput, "Modeling of Magnetically Levitated Planar Actuators With Moving Magnets," *IEEE Transactions on Magnetics*, vol. 43, no. 1, pp. 15–25, 1 2007.

[54] S. Zhang, X. Dang, K. Wang, J. Huang, J. Yang, and G. Zhang, "An Analytical Approach to Determine Coil Thickness for Magnetically Levitated Planar Motors," *IEEE/ASME Transactions on Mechatronics*, vol. 22, no. 1, pp. 572–580, 2017.

[55] S. Zhang, L. Niu, L. Zhou, J. Huang, W. Hu, and G. Zhang, "Optimal Matching Design of Length and Width of Rectangular Ironless Coils for Magnetically Levitated Planar Motors," *IEEE Access*, vol. 7, pp. 185 301–185 309, 2019.

[56] J. Peng, Y. Zhou, and G. Liu, "Calculation of a New Real-Time Control Model for the Magnetically Levitated Ironless Planar Motor," *IEEE Transactions on Magnetics*, vol. 49, no. 4, pp. 1416–1422, 4 2013.

[57] F. Xu, Y. Lv, X. Xu, and V. Dinavahi, "FPGA-Based Real-Time Wrench Model of Direct Current Driven Magnetic Levitation Actuator," *IEEE Transactions on Industrial Electronics*, vol. 65, no. 12, pp. 9635–9645, 12 2018.

[58] T. Zheng, F. Xu, X. Lu, and X. Xu, "A New Multi-Objective Optimization Method of Magnetic Levitation Planar Motor," *IEEE Transactions on Magnetics*, vol. 55, no. 8, pp. 1–8, 8 2019.

[59] B. Kou, F. Xing, L. Zhang, C. Zhang, and Y. Zhou, "A Real-Time Computation Model of the Electromagnetic Force and Torque for a Maglev Planar Motor with the Concentric Winding," *Applied Sciences*, vol. 7, no. 1, 2017.

[60] D. Yuan, M. Zhang, Y. Zhu, L. Wang, X. Li, and C. Hu, "Extended unified wrench model suitable for the end effect of the ironless permanent magnet planar motor," *IET Electric Power Applications*, vol. 13, no. 3, pp. 402–409, 3 2019.

[61] H. J. Ahn and K. R. Kim, "2D Hall Sensor Array for Measuring the Position of a Magnet Matrix," *International Journal of Precision Engineering and Manufacturing-Green Technology*, vol. 1, no. 2, pp. 125–129, 2014.

[62] S. Du, J. Hu, Y. Zhu, and M. Zhang, "A Hall Sensor-Based Position Measurement With On-Line Model Parameters Computation for Permanent Magnet Synchronous Linear Motor," *IEEE Sensors Journal*, vol. 18, no. 13, pp. 5245–5255, 7 2018.

[63] C. Hu, Z. Wang, Y. Zhu, M. Zhang, and H. Liu, "Performance-Oriented Precision LARC Tracking Motion Control of a Magnetically Levitated Planar Motor With Comparative Experiments," *IEEE Transactions on Industrial Electronics*, vol. 63, no. 9, pp. 5763–5773, 9 2016.

[64] Z. Wang, C. Hu, Y. Zhu, S. He, M. Zhang, and H. Mu, "Newton-ILC Contouring Error Estimation and Coordinated Motion Control for Precision Multiaxis Systems With Comparative Experiments," *IEEE Transactions on Industrial Electronics*, vol. 65, no. 2, pp. 1470–1480, 2 2018.

[65] F. Song, Y. Liu, J.-X. Xu, X. Yang, P. He, and Z. Yang, "Iterative Learning Identification and Compensation of Space-Periodic Disturbance in PMLSM Systems With Time Delay," *IEEE Transactions on Industrial Electronics*, vol. 65, no. 9, pp. 7579–7589, 9 2018.

[66] M. Li, Y. Zhu, K. Yang, L. Yang, and C. Hu, "Data-Based Switching Feedforward Control for Repeating and Varying Tasks: With Application to an Ultraprecision Wafer Stage," *IEEE Transactions on Industrial Electronics*, vol. 66, no. 11, pp. 8670–8680, 11 2019.

[67] F. Boeren, A. Bareja, T. Kok, and T. Oomen, "Frequency-Domain ILC Approach for Repeating and Varying Tasks: With Application to Semiconductor Bonding Equipment," *IEEE/ASME Transactions on Mechatronics*, vol. 21, no. 6, pp. 2716–2727, 12 2016.

[68] T. Ou, C. Hu, Y. Zhu, M. Zhang, and L. Zhu, "Intelligent Feedforward Compensation Motion Control of Maglev Planar Motor With Precise Reference Modification Prediction," *IEEE Transactions on Industrial Electronics*, vol. 68, no. 9, pp. 7768–7777, 9 2021.

[69] Z. Wang, R. Zhou, C. Hu, and Y. Zhu, "Online Iterative Learning Compensation Method Based on Model Prediction for Trajectory Tracking Control Systems," *IEEE Transactions on Industrial Informatics*, vol. 18, no. 1, pp. 415–425, 1 2022.

[70] R. Hollis and S. E. Salcudean, "Lorentz Levitation Technology: a New Approach to Fine Motion Robotics, Teleoperation, Haptic Interfaces, and Vibration Isolation," in *Research report, International Business Machines Corporation, T. J. Watson Research Center*, 10 1993, pp. 1 – 20.

[71] Keyence, "Ultra High-Speed/High-Accuracy Laser Displacement Sensor - LK-G5000 series," 2022. [Online]. Available: https://www.keyence.ca/products/measure/laser-1d/lk-g5000/

[72] H. Anton and C. Rorres, *Elementary Linear Algebra: Applications Version*, 11th ed. Hoboken, NJ: John Wiley & Sons Inc., 2014.

Appendices

Appendix A

Trajectory Generation

The position references are generated in TwinCAT based on user input in the visualization panel. The user can enter "end goal" targets for each of the 6 axes and if the difference between the current reference and the new goal is less than a threshold, the new goal is directly sent as a step input. However, if the difference is greater than a threshold, then intermediate points in a smooth ramp are generated and sent to the controller. The horizontal x, y translation axes are a special case where the ramps are generated in conjunction so that the overall direction of velocity goes directly to the target in both axes, rather than reaching the target in one axis before the other. The intermediate points are generated using a stored speed of the reference in each axis v_x and v_y and incrementing the reference positions x_{ref} and y_{ref} each time step. This process is outlined in this section.

First, based on the remaining distance to the target and the current velocity of the reference, it is checked if the reference should accelerate, decelerate, or remain at a constant velocity given by $v_{\max}$ which the user can modify in the visualization panel.

The remaining distance to the end goal is calculated using

$$d_{\text{rem}} = \sqrt{(x_{\text{end}} - x_{\text{ref},n-1})^2 + (y_{\text{end}} - y_{\text{ref},n-1})^2}. \tag{A.1}$$

The current speed of the reference in xy is

$$v_{xy} = \sqrt{(v_{x,n-1})^2 + (v_{y,n-1})^2}, \tag{A.2}$$

where $v_{x,n-1}$ and $v_{y,n-1}$ are the speed of the reference in the x and y directions from the last PLC cycle.

The required distance to stop can then be found using

$$d_{\text{stop}} = \frac{v_{xy}^2}{2a_{xy}}, \tag{A.3}$$

where a_{xy} is the magnitude of acceleration which can be modified in the visualization panel.

If the distance to the end goal is greater than the stopping distance, $d_{\text{rem}} > d_{\text{stop}}$, and the current speed is less than the maximum speed, $v_{xy} < v_{\max}$, then the mover can increase its speed. Based on the direction toward the end goal, the maximum speed is split into x and y components,

$$v_{x,\max} = \cos(\theta_v) v_{\max}, \tag{A.4a}$$
$$v_{y,\max} = \sin(\theta_v) v_{\max}, \tag{A.4b}$$

where $v_{\max}$ is a configurable speed and the direction to the end goal can be found from

$$\theta_v = \text{arctan2}(y_{\text{end}} - y_{\text{ref},n-1}, x_{\text{end}} - x_{\text{ref},n-1}). \tag{A.5}$$

Note that this should be calculated using a four-quadrant inverse tangent.

Using these maximum speed components, a direction of acceleration is found

$$\theta_{\text{accel}} = \text{arctan2}(v_{y,\max} - v_{y,n-1}, v_{x,\max} - v_{x,n-1}). \tag{A.6}$$

The velocity of the reference in xy is then incremented using

$$v_{x,n} = v_{x,n-1} + \cos(\theta_{\text{accel}}) a_{xy} t_s, \tag{A.7a}$$
$$v_{y,n} = v_{y,n-1} + \sin(\theta_{\text{accel}}) a_{xy} t_s, \tag{A.7b}$$

where t_s is the time step. Due to the discrete nature of this update, the overall velocity can only increase in increments of $a_{xy} t_s$. If the reference velocity is within this tolerance of $v_{\max}$, then the velocity components are set directly to $v_{x,n} = v_{x,\max}$ and $v_{y,n} = v_{y,\max}$.

The position references for this cycle are then updated using

$$x_{\text{ref},n} = x_{\text{ref},n-1} + v_{x,n} t_s, \tag{A.8a}$$
$$y_{\text{ref},n} = y_{\text{ref},n-1} + v_{y,n} t_s. \tag{A.8b}$$

If the remaining distance is less than the stopping distance, $d_{\text{rem}} < d_{\text{stop}}$, then the reference should start to decelerate. However, because this is calculated discretely, waiting until this condition is satisfied may result in a slight overshoot of the end goal. As such, deceleration is started one frame earlier by checking if $|d_{\text{rem}} - v_{xy} t_s| < d_{\text{stop}}$. To add some tolerance, it will only accelerate if $|d_{\text{rem}} - 2 v_{xy} t_s| > d_{\text{stop}}$ and $v_{xy} < v_{\max}$. When decelerating, the velocity of the reference is updated using the same approach as in equation (A.7),

$$v_{x,n} = v_{x,n-1} + \cos(\theta_{\text{decel}}) a_{xy} t_s, \tag{A.9a}$$
$$v_{y,n} = v_{y,n-1} + \sin(\theta_{\text{decel}}) a_{xy} t_s, \tag{A.9b}$$

where the deceleration direction is calculated based on the current velocity

$$\theta_{\text{decel}} = \text{arctan2}(-v_{y,n-1}, -v_{x,n-1}). \tag{A.10}$$

Due to the discrete nature of incrementing the reference, the smallest x, y step the reference can take is $a_{xy}t_s^2$. If the distance to the end goal d_{rem} is within this tolerance, then the reference is set directly to $x_{\text{ref},n} = x_{\text{end}}$ and $y_{\text{ref},n} = y_{\text{end}}$.

An example reference trajectory is shown in figure A.1. In this example, the end goal $(x_{\text{end}}, y_{\text{end}})$ was first set to $(1030, -345)$ and the mover started to move in the x direction. After the mover was approximately halfway there, the goal was changed to $(1030, 345)$, which was in a different direction. Because this method of trajectory generation stores the velocity of the reference (v_x, v_y) and increments it each loop, when the end goal changes, this velocity is smoothly modified to the new direction of the goal. The lower two plots in figure A.1 show the velocity of the reference in x and y and as can be seen from the plots, the velocity changes linearly with time and there is no discontinuity. By designing the reference this way, with acceleration and deceleration periods, it is easier for the PID controllers to track the reference. It is also easier to reach higher speeds by accelerating slowly as the mover is more stable and can use smaller control efforts. In the example shown in the figure, the maximum velocity during the motion was set to 500 mm/s and the acceleration was set to 500 mm/s^2 so it is easy to see in the plot. However, during most experiments in this research, the acceleration was set to 2500 mm/s^2.

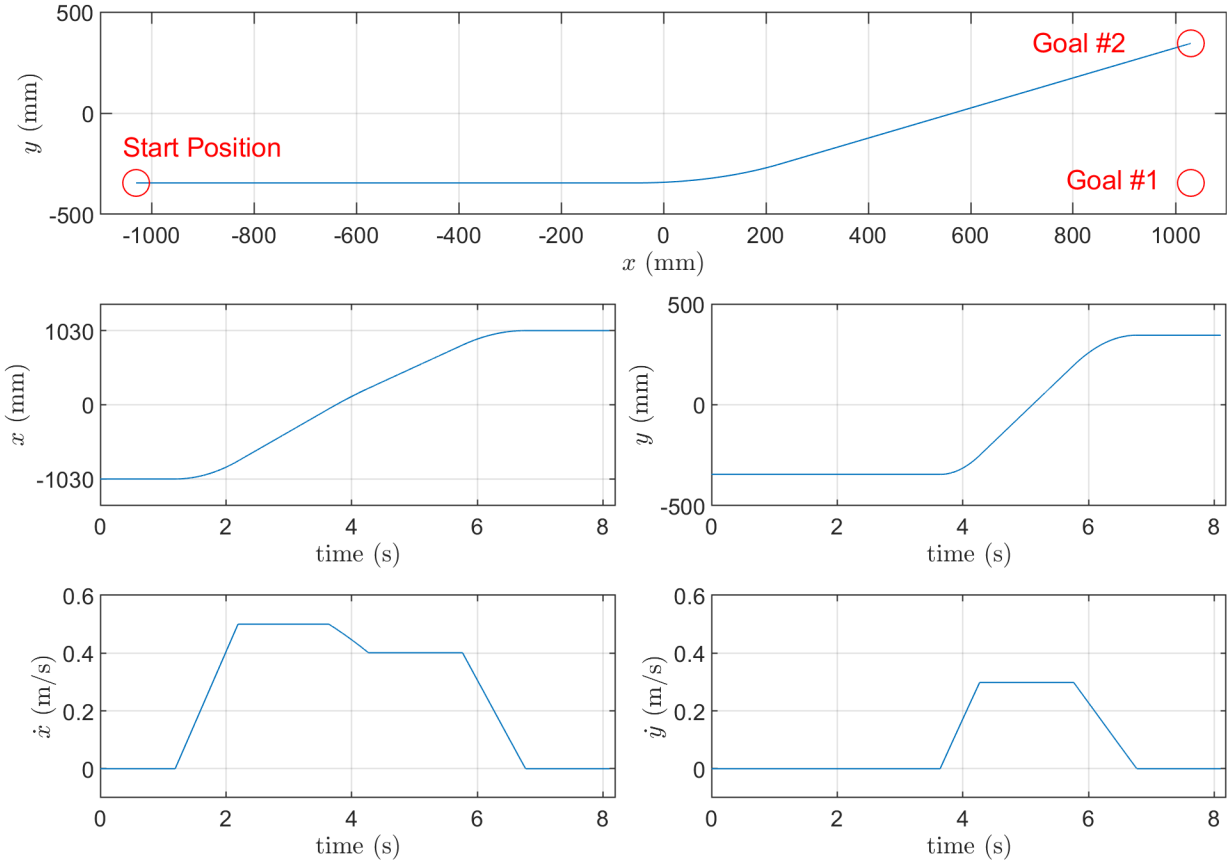

Figure A.1: Example reference trajectory as it adjusts to an end goal change from the user during motion, showing an xy top view, x and y over time, and their derivatives.

A.1 Circle Generation

To generate a circle or an ellipse, an intermediate variable of the angular position ϕ is smoothly accelerated, held to a constant angular velocity, then decelerated at the end of the trajectory. This angular position could be discretely incremented using a time step, such as in the previous section, or it could be calculated based on an elapsed time from the start of the trajectory. The equations in this section describe calculating the trajectory using an elapsed time as this results in less discretization error. First, the maximum tangential velocity and acceleration are converted into their angular counterparts, using $\omega_{\max} = v_{\max}/r$ and $\alpha = a/r$, where $v_{\max}$ and a are the tangential velocity and acceleration and r is the radius of the circle. The acceleration time is then simply $t_{\text{accel}} = \omega_{\max}/\alpha$. During this period, the angular position is given by

$$\phi = \frac{\alpha t_1^2}{2}, \tag{A.11}$$

where t_1 is the time since the start of the trajectory. At the end of the acceleration period t_{accel}, the angular position will be

$$\phi_{\text{accel}} = \frac{\omega_{\max}^2}{2\alpha}. \tag{A.12}$$

Thus, during the constant angular velocity period, the angular position is given by

$$\phi = \phi_{\text{accel}} + \omega_{\max} t_2, \tag{A.13}$$

where t_2 is the time since the acceleration period ended. The time the angular velocity is constant is given by

$$t_{\text{constant}} = (2\pi n - 2\phi_{\text{accel}})/\omega_{\max}, \tag{A.14}$$

where n is the desired number of loops of the circle to perform. Once this time has elapsed, the angular velocity will decelerate and the angular position is given by

$$\phi = 2\pi n - \phi_{\text{accel}} + \omega_{\max} t_3 - \frac{\alpha t_3^2}{2}, \tag{A.15}$$

where t_3 is the time since the deceleration period started. Once $t_3 = t_{\text{accel}}$, then the deceleration period will end and the angular position will be $\phi = 2\pi n$.

Using the angular position, the reference positions $(x_{\text{ref}}, y_{\text{ref}})$ can be calculated

$$x_{\text{ref}} = x_0 + r_x(1 + \cos(\phi + \pi)), \tag{A.16a}$$
$$y_{\text{ref}} = y_0 + r_y \sin(\phi + \pi), \tag{A.16b}$$

where (x_0, y_0) is the initial position at the start of the circle trajectory and r_x and r_y are the radii in the x and y directions. For a circle, these will be equal $r_x = r_y = r$, however, for an elliptical motion, they can be different. Using this method to generate an elliptical motion will result in the tangential velocity varying as the mover travels along the ellipse. The motion described by these equations will be in the clockwise direction starting from the left side of the circle.

A.2 Figure-Eight Generation

To generate a figure-eight motion, the same concept of the angular position can be used, except a sine wave can be given at twice the frequency in one axis compared to the other. For example, the equations

$$x_{\text{ref}} = x_0 + r_x(1 + \cos(\phi + \pi)), \tag{A.17a}$$

$$y_{\text{ref}} = y_0 + r_y \sin(2\phi + \pi), \tag{A.17b}$$

will generate a figure-eight motion oriented in the horizontal direction. In this case, the maximum tangential velocity will occur twice at the intersection of the path when both the velocity in x and y are maximum. The maximum angular velocity can be calculated from

$$\omega_{\max} = v_{\max} \cos(\arctan(2r_y/r_x))/r_x, \tag{A.18}$$

assuming that the motion is at twice the frequency in the y axis. For the tests in this research, typically $r_x > 2r_y$ for the figure-eight motion.